Cosmology with Velocity Dispersion based Counts of Groups and The Effect of AGN Feedback on Host Galaxy Morphology

Caroline Elizabeth Caldwell

A thesis submitted in partial fulfilment of the requirements of

Liverpool John Moores University

for the degree of

Doctor of Philosophy.

October 2016

0.1 Preface

A Tale of Two Theses

It was the best of times, it was the worst of times, it was the age of wisdom, it was the age of foolishness, it was the epoch of belief, it was the epoch of incredulity, it was the season of Light, it was the season of Darkness, it was the spring of hope it was the winter of despair...

A Tale of Two Cities, Charles Dickens

This thesis is written in two completely independent parts. This is based on the progress of my PhD. I was working on AGN, then my supervisor left, and now I am researching cosmology. The first part of this thesis is my current research on combining simulations and observations to constrain cosmological parameters using velocity dispersions of groups. The second part was research conducted in the first year and a half of my PhD, and focuses on the effect of AGN feedback on galaxy star formation and morphology.

Although some may say it is customary to write the thesis on one subject, I have chosen to separate the thesis into two independent parts to maintain the potency of the arguments and theories that are relevant to each particular part. Each part has its own introduction, literature review, conclusions, and future work. I am not in any way saying that there is not a bridge between the two parts, but for the sake of clarity, I leave this to a verbal discussion.

Declaration

The work presented in this thesis was carried out at the Astrophysics Research Institute, Liverpool John Moores University. Unless otherwise stated, it is the original work of the author.

While registered as a candidate for the degree of Doctor of Philosophy, for which submission is now made, the author has not been registered as a candidate for any other award. This thesis has not been submitted in whole, or in part, for any other degree.

Caroline E. Caldwell
Astrophysics Research Institute
Liverpool John Moores University
IC2, Liverpool Science Park
146 Brownlow Hill
Liverpool
L3 5RF
UK

DECEMBER 19, 2016

Abstract

The evolution of galaxy cluster counts is a powerful probe of several fundamental cosmological parameters. A number of recent studies using this probe have claimed tension with the cosmology preferred by the analysis of the Planck primary CMB data, in the sense that there are fewer clusters observed than predicted based on the primary CMB cosmology. One possible resolution to this problem is systematic errors in the absolute halo mass calibration in cluster studies, which is required to convert the standard theoretical prediction (the halo mass function) into counts as a function of the observable (e.g., X-ray luminosity, Sunyaev-Zel'dovich flux, optical richness).

Here I propose an alternative strategy, which is to directly compare predicted and observed cluster counts as a function of the one-dimensional velocity dispersion of the cluster galaxies. I show that the velocity dispersion of groups/clusters can be theoretically predicted as robustly as mass but, unlike mass, it can also be directly observed, thus circumventing the main systematic bias in traditional cluster counts studies. With the aid of the BAHAMAS suite of cosmological hydrodynamical simulations, I demonstrate the potential of the velocity dispersion counts for discriminating even similar ΛCDM models. Then, I compare the abundance of groups in the GAMA survey to the predictions from BAHAMAS to constrain the values of several cosmological parameters.

Additionally, I investigate the role of active galactic nuclei (AGN) in galaxy evolution. The color bimodality of galaxy populations roughly divides galaxies into two groups: blue, star-forming galaxies, and red, quiescent galaxies. One theory that explains how high-mass, red, non-star-forming galaxies maintain this condition is the duty cycle hy-

pothesis. This hypothesis invokes AGN feedback from low luminosity radio-loud AGN (LERGs) to deposit mechanical heating into the intergalactic medium, thus preventing star formation.

I test this hypothesis by comparing the half-light radii of quiescent elliptical galaxies with LERG host galaxies using a large multi-wavelength sample from two surveys, UKIDSS/UDS, and ULTRAVISTA/COSMOS. The radius distribution of the two groups are similar, thus providing evidence for the duty cycle hypothesis. I also check the star formation activity of the LERGs. For the duty cycle to hold, LERGs should reside within non-star-forming galaxies. However, I find that a subset of LERGs appear to be dusty star forming galaxies.

Publications

The following papers contain work from this thesis, and have been submitted for publication in a refereed journal:

1. Caldwell, C. et al., ”Cosmology with velocity dispersion counts: An alternative to measuring cluster halo masses”, 2016, MNRAS, 462, 4117

2. Wilson, S., et al., ”The XMM Cluster Survey: evolution of the velocity dispersion -temperature relation over half a Hubble time”, 2016, MNRAS

3. Povic, M., et al., ”The impact from survey depth and resolution on the morphological classification of galaxies,” 2015, MNRAS,453,1644

Acknowledgements

First I would like to thank my parents, who have been very distant since I moved to the UK. Nevertheless, I would not have made it this far without their many sacrifices and support, and I appreciate it. I would like to thank my great-grandmother, Janet Hargrove, and my grandmother, Mary Palmer, for dealing with and overcoming all the shit that smart and strong women had to deal with in the 20th century. I wish you both were still here. I always think that if you could get through it, then I can too.

My PhD has not been anything like I dreamed it would be, but I would like to thank my supervisors, Ivan Baldry, Chris Collins, and Ian McCarthy for making the most of a bad situation. I believe that I am a better scientist because of your guidance. I would also like to thank Mike Endl and Bev Wills at the University of Texas at Austin, for giving me a strong foundation to build my research experience on. When things were bad, my experiences at UT reminded me that things can be better.

I always expected this thesis to be the thing I would be most proud of at the end of my PhD, but it isn't. I think I have done enough to earn the degree, but I didn't earn it in the way I wanted to, and that will always be disappointing. The friendships I have made here, however, make me very proud. Helen, Rich, Andy, Katie, Rob, Maia, David, Scott, and Ben. I feel very lucky to have met y'all, and I am really upset about leaving you all here, while I get to move back to America. Thank you for listening and keeping me happy and sane. I hope that I can repay you for your kindness one day.

Finally, I would like to thank music. My lifelong hobby that reminds me that astronomy is not the only thing going on in the world. If it had not been for my musical interludes, I wouldn't have been able to keep the PhD going. Thanks mom for teach-

ing me to sing and forcing me to take piano lessons so I would be good at music theory. Thanks Kim, for teaching me to move with all sorts of music – not just classical, and providing numerous opportunities to practice grace under pressure. The dance and music in my childhood has helped me face so many situations in my adult life that I could have never planned for as a kid in Mount Pleasant.

Thank you Port Sunlight Orchestra for being the first non-astronomy British people I got to meet. You guys are great folks, and great musicians. Thank you for letting me play cello in your orchestra even though my sight-reading is not very good. Thank you Liverpool String Orchestra for accepting me into your group when I was too busy to make it across the Mersey to PSO. Thank you D'ukes of Hazzard, for being the second, and much less serious, group of non-astronomy Brits I have encountered. You guys are a lot of fun. It is highly improbable that I will ever meet such a silly (and I mean silly in the most honorific way possible), friendly, and accepting group of people, like you again. Singing and playing ukulele covers with you on Thursdays has been the one thing I could look forward to, as I was working on finishing my thesis. Finally, I would like the thank the musical *Hamilton* for providing my ambition with an anthem."Just like my country, I'm young, scrappy and hungry, and I am not throwing away my shot."

"A book, too, can be a star, a living fire to lighten the darkness, leading out into the expanding universe."

- Madeline L'Engle

Contents

List of Tables

List of Figures

Part I

Cosmological Constraints from Velocity Dispersions of Galaxy Groups

Chapter 1

Introduction

1.1 General Introduction

In 1915, Einstein published the field equations for his general theory of relativity. Astrophysics has played an important role in providing empirical evidence for the theory. In 1919, Eddington's observations of stars during a solar eclipse showed that general relativity accurately predicts the gravitational deflection of light paths (Dyson et al., 1920). In the 1920's and 30's, the search for exact solutions to Einstein's field equations resulted in what is now called the Friedmann-Robertson-Walker-Lemaitre (FLRW) metric. This metric is based on two assumptions: the universe on large scales is homogenous and isotropic. When the metric is applied to the field equations, the following solution (Friedmann, 1922) is obtained:

$$\left(\frac{\dot{a}}{a}\right)^2 = \frac{8\pi G\rho}{3} + \frac{\Lambda c^2}{3} - \frac{kc^2}{a^2}, \tag{1.1}$$

$$\frac{\ddot{a}}{a} = \frac{4\pi G}{3}\left(\rho + \frac{3p}{c^2}\right) + \frac{\Lambda c^2}{3}. \tag{1.2}$$

These equations are known as the Friedmann Equations. The scale factor, a, is a function of time, and describes the expansion of the universe. The Hubble parameter, H, appears in equation 1.1 as $\frac{\dot{a}}{a}$. When the H^2 is divided by on both sides, the right hand

side terms of equation 1.1 describe three fundamental cosmological parameters. From left to right they are: the matter density of the universe (Ω), the dark energy density of the universe (Ω_Λ), and the curvature of space.

The time dependent scale factor, a, means that the size of the universe is not static. Once again, astronomy played a role in providing supporting evidence for this theory. Hubble's observations, in 1929, of the recession velocity of galaxies showed a correlation between recession velocity and distance (Hubble, 1929). This was seen as evidence for the expansion of the universe. Lemaitre took this idea to the $t = 0$ limit, and proposed, in 1931, that the universe started from a single point, "l'atom primitif" (Lemaitre, 1931). This theory became known as the Big Bang.

1.2 Modern Cosmology

Now, the big bang theory is accepted as the standard cosmological model. From this theory it can be shown that the Universe began in a hot, dense state where matter and radiation were in equilibrium. As the Universe expanded, it cooled. At z $\approx$1100 it had cooled sufficiently for recombination to take place, allowing the radiation to decouple from the matter and travel across the Universe essentially uninhibited (Peebles, 1968). This radiation is known as the cosmic microwave background, CMB.

The CMB is a probe of large-scale structure, because it is the earliest look at over densities of matter in the universe. Although FLRW requires a homogeneous universe, at decoupling these over densities are very small and therefore the FLRW metric continues to be a good approximation. These over densities are directly related to the initial conditions of the universe. Understanding and quantifying these initial conditions is a primary goal of observational cosmology. Three major cosmological surveys of the modern era are: Cosmic Background Explorer (COBE) (Smoot et al., 1992), the Wilkinson Microwave Anisotropy Probe (WMAP) (Hinshaw et al., 2003), and Planck (Planck Collaboration et al., 2011). These surveys have observed the whole sky in microwave radiation and use the cosmic microwave background temperature and po-

larization anisotropy to understand how structure formed in the universe.

WMAP and Planck follow the pioneering work of the first all sky mission to map CMB anisotropy, COBE (Smoot et al., 1992). COBE, first data release 1992, was the first space based mission to show small temperature anisotropy in the CMB. The following two missions, WMAP and Planck, have viewed these density fluctuations in higher spatial resolution. WMAP began observing in 2001, and its final data release was published in 2011 after 9 years of observing the CMB. It uses 5 bands ranging from 23 to 94 GHz to observe the CMB (Hinshaw et al., 2013). The increased number of bands, from the COBE experiment, provide information on foreground flux from the galaxy that must be subtracted before measuring the CMB. Planck is a further improvement on resolution. Planck began operating in 2009 and the most recent full data release was in 2015. It has 33 detectors and observes in the range of 30 GHz to 875 GHz with nine different bands (Planck Collaboration et al., 2011).

1.2.1 Power spectrum

Once an all sky map has been created, a power spectrum, i.e. a statistical approximation of the clustering of matter as a function of distance, is produced. The angular power spectrum, modeled in figure 1.1 is estimated from the temperature fluctuations of the CMB map.

Parametric fits to the Planck and WMAP power spectra are compared in figure 1.1 (Larson et al., 2015). The peaks in the power spectrum indicate where baryonic matter is initially more clustered. Figure 1.1 shows that there is a small, $\sim 2\%$, difference between the amplitude of the peaks of the WMAP and Planck surveys. Due to the systematic difference between the two surveys, Larson et al. (2015) show a grey, 1σ band of uncertainty around the ratio of the two surveys, indicating that the differences between WMAP and Planck are almost always less than one standard deviation. However, I will demonstrate throughout this thesis that these small differences have a large impact on structure formation in the universe.

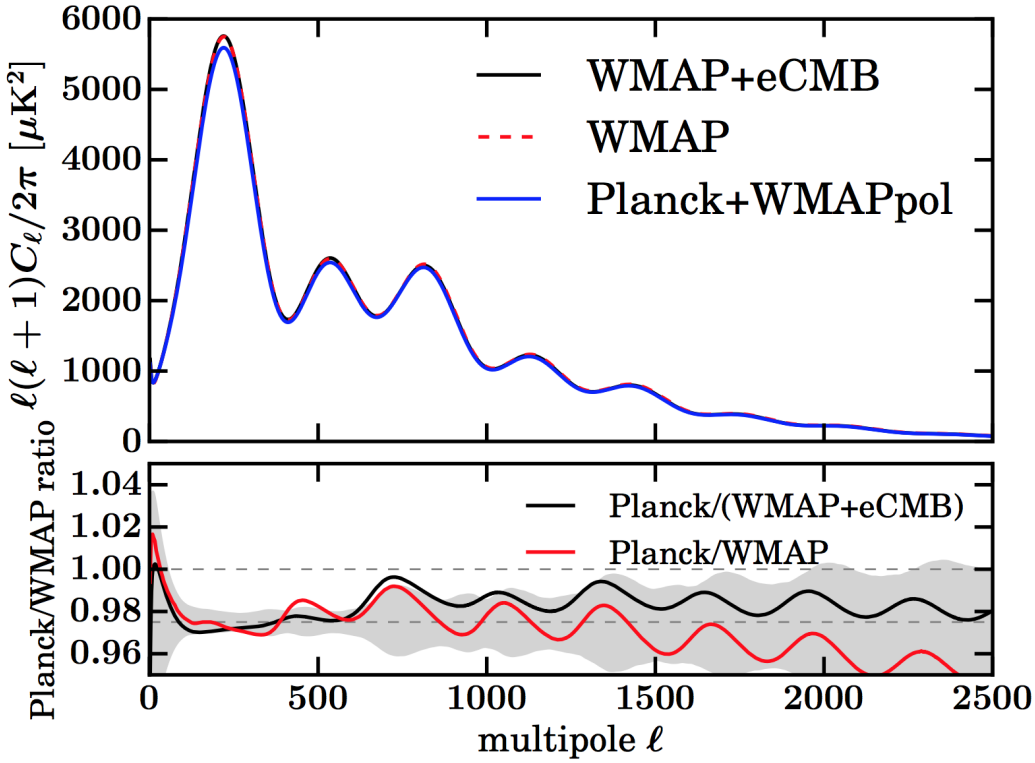

Figure 1.1: copied from this figure's caption in Larson et al. (2015) "A comparison of the best-fit 6-parameter λCDM model spectra derived from recent CMB data sets. *Solid black* - fit to WMAP+eCMB data (SPT and ACT); *dashed red*- fit to WMAP (only) data; *solid blue* - fit to Planck plus WMAP low-l polarization data. The bottom panel shows the ratio of the Planck-based fits to the two WMAP-based fits. The dominant feature is a $\sim 2\%$ amplitude difference between the fits, though some structure is present in the ratio. A dashed horizontal line is shown at 0.975 to guide the eye. The WMAP-only forecast, in red, exhibits an additional $\sim 2\%$ difference at high l, well beyond the l range directly measured by WMAP ($l < 1200$). The gray band shows the 1σ uncertainty in the ratio accounting for the fact that WMAP and Planck observe the same sky, but apply different sky masks, cover different multipole ranges and have independent noise. Given this uncertainty, we cannot distinguish a simple amplitude rescaling from a more complicated shift in parameters."

1.2.2 Cosmological Parameters

The WMAP survey was the first all sky survey to measure the CMB power spectrum over a large range of angular scales. These observations are best fit by a model with six cosmological parameters. The standard 6-parameter model is composed of $\Omega_c h^2$, $\Omega_b h^2$, Ω_Λ, $10^9 \Delta_R^2$, n_s, and τ. There are many other derived parameters, a few of interest are σ_8, Ω_m, and H_0. $\Omega_c h^2$ is the physical cold dark matter density, $\Omega_b h^2$ is the physical baryon density, Ω_Λ is the dark energy density, $10^9 \Delta_R^2$ is the amplitude of the primordial scalar curvature perturbations at $k = 0.002\mathrm{Mpc}^{-1}$, n_s is the spectral index of the primordial density perturbations, and τ is the optical depth at reionization (Hinshaw et al., 2013). Additionally, σ_8 is the parameter that describes the standard deviation of matter density on scales of 8 Mpc$/h$, Ω_m is the sum of the matter densities: Ω_c, Ω_b, and in some cases, $\Omega_{neutrino}$, and finally, H is the Hubble parameter, defined as the recession velocity divided by the distance. When the parameter appears in this form, H_0, it is to be evaluated at redshift 0.[1]

In general, the parameters are derived with the following method. First, theoretical model power spectra are generated using CAMB[2] (Lewis et al. 2000; April 2014 version), assuming a flat ΛCDM cosmology. Then, assuming a uniform probability of a given set of cosmological parameters and that the temperature fluctuations are gaussian, a maximum likelihood estimation is run on the power spectra to determine the best fit parameters (Hinshaw et al., 2003).

1.2.3 Neutrinos

The best-fit cosmological parameters indicate that dark matter constitutes a large fraction, approximately a quarter, of the composition of the universe. Several candidates have been suggested as the physical component of dark matter, including, MACHOs, WIMPs, and neutrinos. Neutrinos are highly energetic particles that very rarely inter-

[1] Another fundamental parameter that is not fitted is the temperature of the CMB, T_0, or equivalently $\Omega_{\mathrm{photons}}$. This is known accurately with $T_0 = 2.725$K.

[2] http://camb.info/

act with the matter around them. As more is learned about the elusive neutrino, it may be the case that neutrinos act like hot dark matter. However, large scale structure points to cold dark matter being the dominant component. Nevertheless, I will show in this thesis that neutrinos have an effect on large scale structure.

An excellent review of the historical development of the neutrino can be found in the introduction of the review article by Xing & Zhao (2016). It was once thought that, due to their rare interactions with matter that neutrinos do not have mass (Weinberg, 1967). However this was disproven using oscillation experiments, and the 2015 Nobel prize in physics was awarded to those scientists who discovered that neutrinos have mass (Kajita, 1999; McDonald et al., 2002). However, the exact value of the neutrino mass is an open question.

Particle physics based experiments have shown that there are 3 mass eigenstates of neutrinos, each individuated by its own unique mixture of neutrino flavors: electron neutrinos, muon neutrinos, and tau neutrinos, but has yet to determine the masses of all three eigenstates (Patterson, 2015). The mixing is shown in figure 1.2. While solar neutrino experiments have established that the mass of species 1 is less than species 2, the mass of species 3 is not known. The normal hierarchy is defined as $m3 > m2 > m1$ and the inverted hierarchy is defined as $m2 > m1 > m3$ (Patterson, 2015). A tight constraint on the summed neutrino mass could discriminate between the two hierarchies. The normal and inverted hierarchy are illustrated in figure 1.2.

Despite not being easy to detect, several particle physics experiments are underway or proposed to understand the underlying hierarchy of neutrinos. These experiments can be grouped into four main categories: Long-baseline, accelerator based (T2K/Super-Kamiokande (Abe et al., 2011)), atmospheric (PINGU/IceCube (Aartsen et al., 2014)), reactor (JUNO/KamLAND (Vogel et al., 2015)), and cosmological (DESI (Levi et al., 2013), EUCLID (Refregier et al., 2010)).The late 2020's to early 2030's are the estimated time frame for significant $(> 5\sigma)$ results from all these experiments. This figure is from Patterson (2015).

Cosmological neutrino experiments are sensitive to the summed mass of the neutrinos

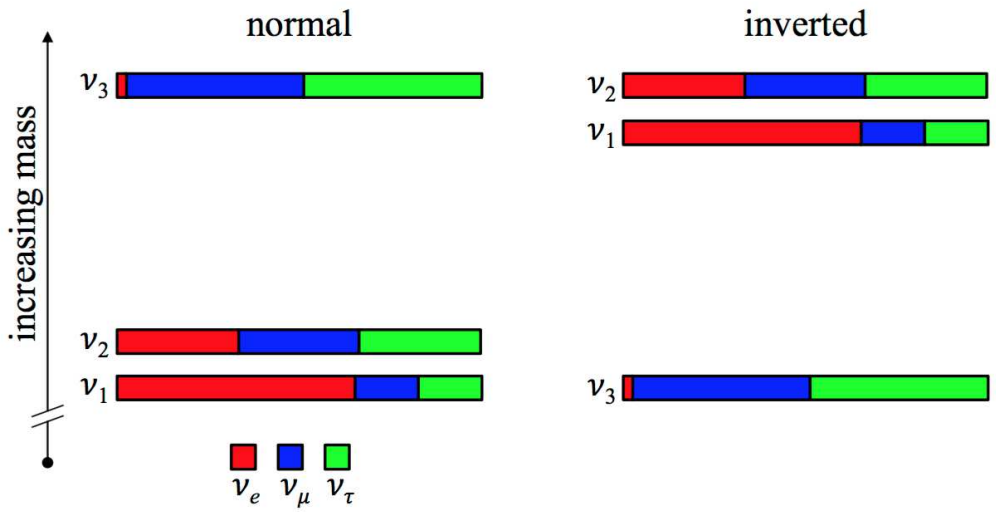

Figure 1.2: This figure shows two possible neutrino mass hierarchies: normal, and inverted. Each neutrino type is a mixture of three neutrino flavors that is represented by the three colors: red, blue, and green. While the mass order of two neutrinos is known, the mass of the third remains undefined. This causes the ambiguity in the hierarchy. (Patterson, 2015)

rather than the hierarchy, specifically. The summed mass can be used to determine the hierarchy by comparing to the known limits determined by oscillation experiments. If the summed mass is less than 0.1 eV, then the hierarchy is normal (Patterson, 2015).

To detect cosmological neutrinos, their effect on the abundances of groups and clusters is observed. They act like hot dark matter that erases structure on small scales (Bird et al., 2012). Neutrinos will free-stream out from primordial over densities before those over densities collapse to form galaxies and groups of galaxies (Bird et al., 2012). The evacuation of neutrinos, which have mass, leaves the over density less massive and less dense, and sometimes the decreased density slows or prevents the gravitational collapse. An estimate of the summed neutrino mass can be made by comparing the observed number of groups to models with varying summed neutrino mass.

1.3 Galaxy Groups and Clusters as Cosmological Probes

The abundance of galaxy groups and clusters at a given redshift is directly tied to cosmological parameters that control the growth rate of structure, such as the total matter density (Ω_m), the amplitude of density fluctuations in the early Universe (σ_8), the spectral index of fluctuations (n_s), and the evolution of dark energy (for recent reviews see Voit 2005; Allen et al. 2011). Consequently, measurements of the evolution of the abundance of groups and clusters can be used to constrain the values of these fundamental cosmological parameters. Recent examples include: Vikhlinin et al. (2009) and Bohringer et al. (2014) using X-ray emission observed with ROSAT, Benson et al. (2013) and Planck Collaboration XX et al. (2014) using the Sunyaev-Zel'dovich (SZ) effect observed with the South Pole Telescope (SPT) and Planck, respectively, and Rozo et al. (2010) using the optical maxBCG sample from the Sloan Digital Sky Survey (SDSS). Upcoming X-ray (eROSITA), SZ (e.g., SPT-3G, ACTpol), and optical (e.g., the Dark Energy Survey, the Large Synoptic Survey Telescope, and Euclid) missions promise to provide even richer datasets that will further enhance this field of study.

In order to compare the observed abundances of groups and clusters with theoretical predictions for a given cosmology, the relation between the observable (e.g., X-ray luminosity, optical richness, weak lensing signal, SZ flux, etc.) and the total mass, including its evolution and scatter, is required to convert the standard theoretical prediction (i.e., the halo mass function) into a prediction for the number counts as a function of the observable. (A separate important issue is that the predictions normally correspond to the total mass in a dark-matter-only model, but the masses of real groups and clusters can be modified significantly by baryonic physics; e.g., Cui et al. 2014; Velliscig et al. 2014.) One can attempt to determine this observable–mass relation either empirically or by using self-consistent cosmological hydrodynamical simulations.

However, both methods have their shortcomings. The empirical route is limited by non-negligible systematic errors in all current methods of total mass estimation (e.g., Rozo et al. 2014) and can, in any case, generally only be applied to relatively small

(generally low-z) samples where the data quality is sufficiently high to attempt mass measurement. The basic problem for the simulation route is that many observable quantities (such as the X-ray luminosity, SZ flux, total stellar mass, etc.) cannot be robustly predicted due to the sensitivity to uncertain 'subgrid' physics (Le Brun et al., 2014).

The issue of absolute mass calibration has been brought to the forefront by the Planck number counts discrepancy (Planck Collaboration et al., 2014). Specifically, the best-fit ΛCDM model based on analyses of the primary CMB data over-predicts the observed number counts by a factor of several (Planck Collaboration XX et al. 2014; Planck Collaboration XXIV et al. 2015, see also Bohringer et al. 2014). One possible explanation for this discrepancy is the presence of a large 'hydrostatic mass bias', such that the adopted X-ray-based masses under-predict the true mass by up to $\sim 50\%$ (e.g., von der Linden et al. 2014). Alternatively, there may be remaining relevant systematics in the Planck CMB data analysis (see, e.g., Spergel et al. 2015; Addison et al. 2015), or the discrepancy could be signaling interesting new physics which suppresses the growth of large-scale structure compared to that predicted by a ΛCDM with parameters fixed (mainly) by the primary CMB at redshift $z \sim 1100$, such as free streaming by massive neutrinos (e.g., Wyman et al. 2014; Battye & Moss 2014; Beutler et al. 2014). Clearly, before we can arrive at the conclusion that there is interesting new physics at play, we must rule out the 'mass bias' scenario.

1.4 Dynamics of Galaxy Groups

One way to independently check the robustness of the discrepancy between observed and predicted galaxy cluster abundances is to measure the abundance of groups/clusters as a function of some other property that can be theoretically predicted as robustly as mass. Fortunately, such a variable exists: the velocity dispersion of orbiting satellite galaxies. The velocity dispersion of the satellites is set by the depth of the potential

well and, when in equilibrium, can be expressed via the Jeans equation as:

$$\frac{d[\sigma_{\rm 3D}(r)^2\rho_{\rm gal}(r)]}{dr} = -\frac{GM_{\rm tot}(r)\rho_{\rm gal}(r)}{r^2}, \tag{1.3}$$

where $\sigma_{\rm 3D}(r)$ is the 3D velocity dispersion profile, $\rho_{\rm gal}(r)$ is the density distribution of the tracer (satellite) population, and $M_{\rm tot}(r)$ is the total mass profile. Provided the simulations have the correct spatial distribution of tracers (which we discuss further below), they ought to predict the velocity dispersion of satellites as robustly as the mass distribution.

In practice it is not necessary to solve the Jeans equations, because the simulations evolve the equations of gravity and hydrodynamics self-consistently, which is necessary given the non-linear complexity of real clusters (e.g., mergers, substructure, asphericity, derivations from equilibrium), and I can directly compare the predicted and observed velocity dispersions. In particular, in the present study I use the BAHAMAS suite of simulations, presented in McCarthy et al. (2016) (hereafter M16). These authors calibrated the stellar and AGN feedback models to reproduce the observed local galaxy stellar mass function and the hot gas mass fractions of X-ray groups and clusters. They then demonstrated that the simulations reproduce a very wide range of other independent observations, including (particularly relevant for the present study) the overall clustering of galaxies (the stellar mass autocorrelation function) and the spatial and kinematic properties of satellites around groups and clusters.

1.5 Outline of Part One

The first part of the thesis addresses the issue of constraining cosmological parameters through comparisons of group abundances in simulations and observations. First, the datasets are introduced. Then, a method is developed using velocity dispersions of simulated groups to constrain cosmological parameters. Finally, I report the progress to-date of the attempt to constrain cosmological parameters using observational data.

Chapter 2

Simulations and Observations

2.1 Introduction

In this section, I describe the simulations and observations used in the research to probe cosmology and large scale structure using velocity dispersions of groups. I discuss the details of the BAryons and HAloes of MAssive Systems (BAHAMAS) simulation, that make it an excellent choice for modeling galaxy group dynamics and probing large scale structure. I also introduce the Galaxies and Mass Assembly (GAMA) survey (Driver et al., 2011), and justify the use of this survey for this project.

2.2 The BAHAMAS simulation

I use the BAHAMAS suite of cosmological smoothed particle hydrodynamics (SPH) simulations, which are described in detail in M16, McCarthy et al. (2016). The BAHAMAS suite consists of large-volume, $400\ h^{-1}\ \mathrm{Mpc}$ on a side, periodic box hydrodynamical simulations. Updated initial conditions based on the maximum-likelihood cosmological parameters derived from the WMAP9 data (Hinshaw et al., 2013) $\{\Omega_m, \Omega_b, \Omega_\Lambda, \sigma_8, n_s, h\} = \{0.2793, 0.0463, 0.7207, 0.821, 0.972, 0.700\}$ and the *Planck* 2013 data (Planck Collaboration XVI et al., 2014) = $\{0.3175, 0.0490, 0.6825, 0.834, 0.9624,$

0.6711$\}$ are used.

The BAHAMAS suite includes simulations with massive neutrinos, which I use for this analysis. Specifically, McCarthy et al. have run massive neutrino versions of the WMAP9 and Planck cosmologies for several different choices of the total summed neutrino mass, M_ν, ranging from the minimum mass implied by neutrino oscillation experiments of ≈ 0.06 eV (Lesgourgues & Pastor, 2006) up to 0.48 eV. When implementing massive neutrinos, all other cosmological parameters are held fixed apart from the matter density due to cold dark matter, which was decreased slightly to maintain a flat model (i.e., so that $\Omega_\mathrm{b} + \Omega_\mathrm{cdm} + \Omega_\nu + \Omega_\Lambda = 1$), and σ_8. The parameter σ_8 characterizes the amplitude of linearized $z = 0$ matter density fluctuations on $8h^{-1}$ Mpc scales. Instead of holding this number fixed, the amplitude of the density fluctuations at the epoch of recombination (as inferred by WMAP9 or Planck data assuming massless neutrinos) is held fixed, in order to retain agreement with observed CMB angular power spectrum. Note that other possible strategies for implementing neutrinos are possible (e.g., decreasing Ω_Λ instead of Ω_cdm) but McCarthy et al. have found with small test simulations that the precise choice of what is held fixed (apart from the power spectrum amplitude) does not have a large effect on the local cluster population. What is most important, is the value of Ω_ν, which is related to M_ν via the simple relation $\Omega_\nu = M_\nu/(93.14 \text{ eV } h^2)$ (Lesgourgues & Pastor, 2006) and ranges from 0.0013 to 0.0105 for our choices of summed neutrino mass.

The Boltzmann code CAMB[1] (Lewis et al. 2000; April 2014 version) was used to compute the transfer functions and a modified version of V. Springel's software package N-GenIC[2] to make the initial conditions, at a starting redshift of $z = 127$. N-GenIC has been modified by S. Bird to include second-order Lagrangian Perturbation Theory (2LPT) corrections and support for massive neutrinos[3].

The runs used here have 2×1024^3 particles, yielding dark matter and (initial) baryon particle masses for a WMAP9 (Planck 2013) massless neutrino cosmology of $\approx 3.85\times$

[1] http://camb.info/
[2] http://www.mpa-garching.mpg.de/gadget/
[3] https://github.com/sbird/S-GenIC

$10^9\ h^{-1}\ \mathrm{M}_\odot$ ($\approx 4.45\times10^9\ h^{-1}\ \mathrm{M}_\odot$) and $\approx 7.66\times10^8\ h^{-1}\ \mathrm{M}_\odot$ ($\approx 8.12\times10^8\ h^{-1}\ \mathrm{M}_\odot$), respectively. (The particle masses differ only slightly from this when massive neutrinos are included.)

The comoving gravitational softening lengths for the baryon and dark matter particles are set to $1/25$ of the initial mean inter-particle spacing but are limited to a maximum physical scale of $4\ h^{-1}$ kpc (Plummer equivalent). The switch from a fixed comoving to a fixed proper softening happens at $z = 2.91$. $N_{\mathrm{ngb}} = 48$ neighbors are used for the SPH interpolation and the minimum SPH smoothing length is limited to 0.01 times the gravitational softening.

The simulations were run using a version of the Lagrangian TreePM-SPH code GADGET3 (last described in Springel, 2005), which was significantly modified to include new subgrid physics as part of the OverWhelmingly Large Simulations project (OWLS)(Schaye et al., 2010). The simulations include prescriptions for star formation (Schaye & Dalla Vecchia, 2008), metal-dependent radiative cooling (Wiersma et al., 2009a), stellar evolution, mass loss, and chemical enrichment (Wiersma et al., 2009b), a kinetic supernova feedback prescription (Dalla Vecchia & Schaye, 2008), and a model for black hole mergers and accretion and associated AGN feedback (Booth & Schaye, 2009). For runs with massive neutrinos, the semi-linear algorithm developed by Ali-Haïmoud & Bird (2013), implemented in GADGET3, was used.

BAHAMAS is a direct descendant of the OWLS and cosmo-OWLS (Le Brun et al., 2014; McCarthy et al., 2014) projects, both of which explored the impact of varying the important parameters of the subgrid models on the stellar and hot gas properties of haloes. These projects demonstrated that many of the predicted observable properties are highly sensitive to the details of the subgrid modeling, particularly the modeling of feedback processes. The idea behind BAHAMAS was therefore to calibrate the supernova and AGN feedback models, using the intuition gained from OWLS and cosmo-OWLS, on some key observables. M16 elected to calibrate the feedback using the local galaxy stellar mass function and the gas mass fractions of groups and clusters, thereby effectively calibrating on the baryonic content of massive haloes (with $\mathrm{M}_{tot} > 10^{12}\mathrm{M}_\odot$).

For the purposes of the present study, the accuracy of the calibration is not critically important provided an appropriate selection criterion is imposed on the simulation satellite population. That is, as long as simulated satellites with *total* masses similar to those of the observed satellites are selected (i.e., we want to select the same tracer populations). In the case of simulations that reproduce the observed galaxy stellar mass function, one can just select simulated galaxies based on their stellar mass (or absolute magnitude). For simulations that significantly violate the galaxy stellar mass function, and will therefore have an unrealistic mapping between stellar mass and halo mass, one could instead use semi-empirical constraints (e.g., subhalo abundance matching) to re-assign the stellar masses of the simulated galaxies, thereby imposing a realistic mapping between stellar mass and halo mass. I explicitly demonstrate the lack of sensitivity of the velocity dispersions to the details of the subgrid modeling in Section 3.1.3.

2.3 The GAMA Survey

The GAMA survey is a highly complete, down to r = 19.8 magnitude, optical spectroscopic redshift survey that covers $\approx$ 180 square degrees (Liske et al., 2015). It overlaps with many well known survey fields, for example GALEX in the ultraviolet, to VIKING in the infrared, and SDSS in the optical. This enables GAMA to have a very extensive multi-wavelength catalog (21 different wavelength band passes) that can be used to address many different questions in astrophysics today, from star formation, galaxy morphology, and cosmology (Driver et al., 2016).

The uniform spatial completeness and deep magnitude depth of the GAMA survey enables unprecedented examination of groups of galaxies (Robotham et al., 2011). These plentiful, but faint associations of galaxies have heretofore not been detected in sufficient number to statistically understand their properties.

The GAMA survey was conducted in three, 60 square degree, regions that are named by the approximate center in right ascension of that slice: G09, G12, and G15 for

centers of 9 hours, 12 hours and 14h30m, respectively. The velocity errors on the redshifts are typically $\sim$ 50 km/s (Baldry et al., 2014). I use two physical quantities, stellar mass and redshift, that have been calculated by members of the GAMA team. The masses are released in Taylor et al. (2011), and the redshifts are described in Baldry et al. (2014); Liske et al. (2015).

2.3.1 Volume-limited sample

As noted in the previous section, the GAMA survey has very high spectroscopic completeness, ninety-nine per cent down to r-band magnitudes of 19.8 (Driver et al., 2011). High completeness ensures that all of the galaxies down to that particular magnitude limit have been observed. However, high completeness is not enough for a comparison of number density. For a number density calculation, a volume limited sample must be created so that the galaxy counts from one sample can be compared to another. In this section, I describe how that volume-limited sample was created.

A nearly volume-limited sample bounded by $0.0 < z < 0.20$ and lower mass limit of $\mathrm{M}_* > 10^{10}\mathrm{M}_\odot$ has been selected from the full GAMA survey, see figure 2.1. The mass limit is set by the resolution limit of the BAHAMAS simulation. Unfortunately, such a high mass limit forces us to discard most of the GAMA data, which excels at observing lower mass galaxies.

The volume redshift limit is determined by considering the redshifts that galaxies, above the mass limit, reach if they were to have an r-band magnitude of 19.8, the magnitude limit of the GAMA survey. This maximum redshift that a galaxy can be observer is called z_{max}. The z_{max} values for the galaxies have been calculated by Taylor et al. (2011). Briefly, the method employed by those authors is the best-fit spectral template for each galaxy is redshifted until its apparent r-band Petrosian magnitude reaches 19.8 mag.

I follow the method described in Lange et al. (2015) to calculate the redshift limit of the volume limited sample, except those authors begin with a redshift limit, and calculate

the mass limit, and I begin with a mass limit and calculate the redshift limit. A plot of stellar mass versus maximum redshift (fig.2.1) shows that, the z_{max} of is 0.20 is an reasonable choice for a mass limit of 10^{10}M$_*$. Choosing a z_{max} at this range means that 64% of the galaxies at the mass limit are seen over the full volume, and it is clear that if the mass limit was increased by another 0.5 dex, nearly all the galaxies in the mass range would be visible at z=0.2 or greater.

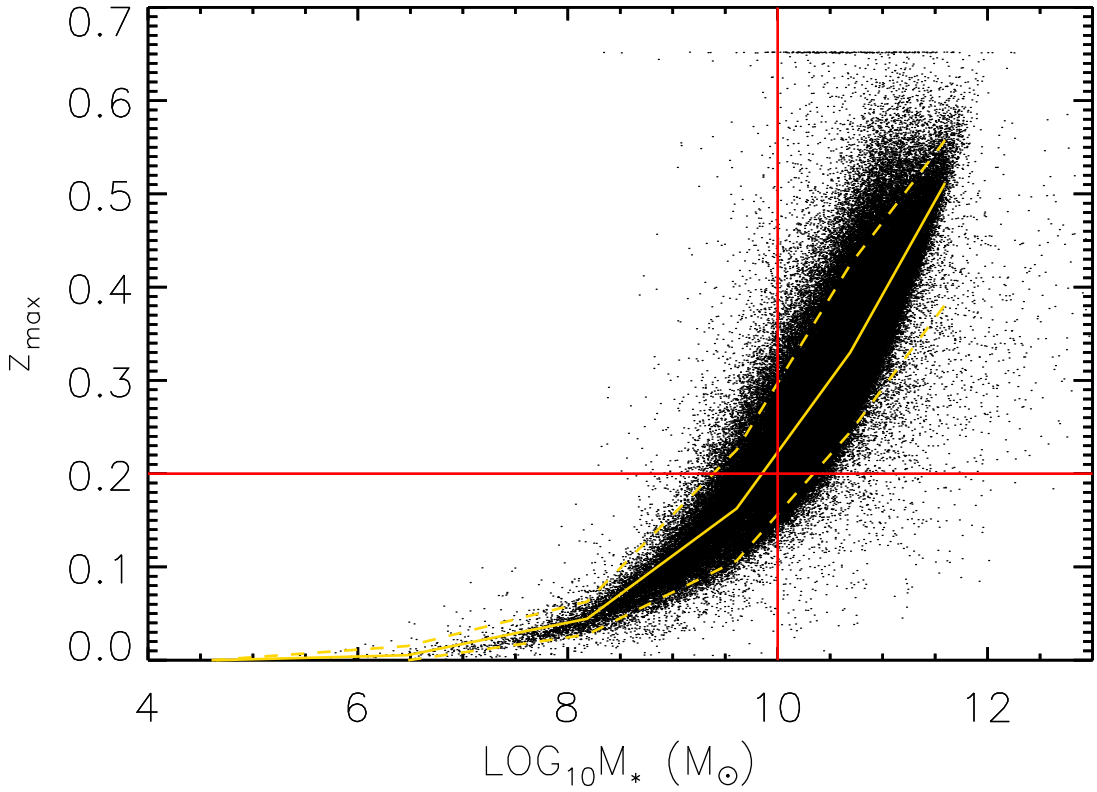

Figure 2.1: The stellar mass-maximum redshift (z_{max}) for the limiting petrosian magnitude of r = 19.8 mag. This plot uses values from the GAMA survey calculated by Taylor et al. (2011). The mass limit imposed by the resolution of the BAHAMAS simulation is log(M⊙) $>$ 10. Therefore I select z=0.2 as the maximum redshift for galaxies in my volume limited sample. The yellow contours show the median and 1 sigma distribution of the data. Although $z_{max} = 0.2$ is not at the flux limit of log(M⊙) = 10, it is below the median value for that range.

2.3.2 Group Finding

Clustering of galaxies can be determined by eye, (Abell, 1958; Zwicky et al., 1961). However, new large redshift surveys have too many groups to make visual detection efficient. The improvements in computational power, and the requirement for repeatable

scientific methods lead modern astronomers to use group finding algorithms. Within the volume-limited sample described above, the grouping of galaxies was determined by the GAMA group finding algorithm, written by Aaron Robotham (Robotham et al., 2011). Below, I discuss the chosen set up for finding groups in this research.

The GAMA group finder uses a Friends of Friends algorithm to detect clustering. The algorithm calculates the separation between galaxies and considers them grouped if the separation (linking distance) meets certain criteria in both the radial and x-y plane projections. Specifically, for the x-y projection, the tangent of the angular galaxy separation must be less than the mean comoving galaxy separation at that epoch, scaled by the mean required linking overdensity (b). The former quantity is calculated from the integral of the galaxy luminosity function to the effective absolute magnitude limit of the survey at that galaxy's position. The latter quantity is determined from analysis of a mock catalog.

For redshift surveys, the apparent lengthening in the radial direction caused by peculiar velocities, which is sometimes referred to as a redshift space distortion or, more figuratively, the finger of god effect, is a major concern and source of error. The recession velocity due to the expansion of the universe, referred to here as the cosmological redshift, is increased or decreased by a factor due to additional motion from the galaxy (peculiar velocity). This additional velocity may be due to a local flow that the galaxy is a member of, or by interacting with a nearby galaxy's gravitational field. This means the total redshift observed is a combination of cosmological and peculiar redshift, and can be expressed as

$$1 + z = (1 + z_{cosmo})(1 + z_{pec}). \tag{2.1}$$

Tempting as it may be to add velocity vectors that point in the same direction, it is important to note that redshifts combine geometrically, as shown above. To account for the effect of peculiar velocities in the group finding algorithm, a radial expansion factor, R, is included in the criteria to increase the linking length. Due to the peculiar velocity increasing in high density environments like clusters, Robotham et al. allow

two of the parameters above, b and R, to vary based on the local density contrast. Taking all the criteria into consideration, there are 8 parameters in this algorithm, but through testing, Robotham et al. find that only two, b and R, are the most dominant and the others only introduce slight perturbations to the grouping.

The group finding algorithm is trained on mock catalogs from the Millennium Dark Matter simulation (Springel, 2005). This is an N-body dark matter simulation, that semi-analyically matches galaxies to DM haloes using GALFORM (Bower et al., 2006). These galaxies then have their r-band magnitudes adjusted to perfectly match the GAMA luminosity function and selection function. The mock catalogs are used to find the parameter space that optimally finds a high group detection rate and low interloper fraction.

Using the optimized parameter set, a comparison is performed between the mock survey and the GAMA survey. Robotham et al. find the purity, which is essentially the fraction of found group member that are classified correctly, of GAMA groups to be 80 per cent, and the purity of mock groups is 73 per cent. The authors also note that at high multiplicities, GAMA has fewer systems than the mock catalog. Overall, the authors conclude that there is remarkable consistency between the mocks and real groups and the velocity dispersion and radius of the groups are median unbiased. These quantities should form an accurate resource for statistical analysis.

Chapter 3

Properties of Galaxy Clusters and Groups from BAHAMAS

Simulations provide a system with known parameters that can aid in the interpretation of observational results. Scaling relations are one way simulations are used in observational research. Most commonly, since mass cannot be directly observed, relationships between observables and mass are created. The mean relations are verified by theory, but often, the scatter is not well accounted for. If large scatter in observations is not accounted for, it could bias the result. This is where simulations become an asset. They can model populations of galaxies, including the scatter, which has astrophysical, statistical, and instrumental sources. In this section, I calculate some velocity dispersion scaling relations, and quantify the scatter using the hydrodynamic simulation BAHAMAS. These relations will form the foundation for cosmological models that I create in Chapter 4.

One observable used for scaling relations is the velocity dispersion of objects. The velocity is calculated from the shift of spectral lines from light emitted by the object. If there are a number of objects gravitationally bound in one system, the distribution and width of the velocities can be calculated. The width of the velocity distribution is called the velocity dispersion.

The classical principle that enables velocity dispersions to be a good tracer of mass is the Virial theorem. This states that the kinetic energy of a system in a state of energetic equilibrium, called 'Virial Equilibrium', is twice the potential energy. In the case of galaxies or galaxy groups, the kinetic energy is the time average of $1/2mv^2$, and the potential is the gravitational potential, hence the relation between velocity and mass.

Another observable commonly used in large galaxy clusters to estimate mass is the hot gas temperature, emitted in the X-ray, which can be determined from fitting the X-ray spectrum. The X-ray emission in high mass groups and clusters is dominated by thermal bremsstrahlung continuum, and is dominated by line emission in less massive groups (Mulchaey, 2000). There is some discussion in the literature about whether the mean relation for temperature and mass is best modeled by a continuous function or a broken power law (Le Brun et al., 2016; Mulchaey, 2000). The basis for this is that some of the energetic processes, such as AGN feedback, affect groups more strongly than clusters. In smaller associations of galaxies, the potential well is weaker, and it is easier for highly energetic gases to escape.

The trouble with all scaling relations is that there is rarely a direct mapping between the observed quantity and a mass. Scatter around the mean relation determines the reliability of the conversion. This is why velocity dispersions are not widely acknowledged as the best mass proxy, because the scatter at low masses can span almost an order of magnitude. Observations can overcome this scatter with increased sensitivity, thus adding more tracers. With the aid of the BAHAMAS simulations, I will model the scatter around the mean velocity dispersion - mass relation as well as several other quantities. With the benefit of hydrodynamic simulations, I can observe the intrinsic and statistical errors. This will provide a quantification of the scatter, and will help interpret results from current observational surveys.

In this chapter, I will describe how groups are selected, and their velocity dispersions are calculated. Using the information about the potential encoded in the velocity dispersions, I will show that velocity dispersions can be used instead of masses to understand the population statistics of a galaxy group. I will also demonstrate that velocity dispersions can be used to distinguish between different cosmological models. Us-

ing the BAHAMAS simulation, I explore several relations between fundamental physical quantities and observables. In many cases, understanding the mean relationship between observables and physical quantities is not sufficient because there is a non-negligible amount of scatter which causes a wide distribution of points about the mean. Additionally, the relations can evolve significantly over cosmic time. Therefore, when necessary, I also investigate the scatter and evolution of the scaling relation.

3.1 Velocity Dispersion Calculation

3.1.1 Galaxy and group selection criteria

Before velocity dispersions for the simulated groups and clusters can be calculated, an appropriate tracer population must be selected. Previous studies (usually based on N-body simulations) often selected bound dark matter particles (e.g., Evrard et al. 2008). However, the satellite galaxy population could in principle have a different spatial/kinematic distribution compared to the underlying smooth dark matter distribution, e.g., through the effects of dynamical friction, or just simply differences in the time of accretion of satellites compared to that of the (smooth) dark matter component. Indeed, many previous studies have found that the satellites are more spatially-extended (i.e., have a lower concentration) than what is measured for the total mass distribution (e.g., Carlberg et al. 1997a; Lin et al. 2004; Budzynski et al. 2012; van der Burg et al. 2015). M16 have shown that in the case of BAHAMAS, the satellites have a negative velocity bias (i.e., a lower velocity dispersion) with respect to the underlying dark matter particles.

With cosmological hydrodynamical simulations, I am able to move beyond selecting dark matter particles, and identify satellite galaxies. Galaxies in the simulations are defined as self-gravitating substructures (identified with SUBFIND algorithm, Springel et al. 2001; Dolag et al. 2009) with non-zero stellar mass. For the analysis below, I present results based on selecting groups of 5 or more galaxies with stellar masses exceeding $10^{10}\mathrm{M}_{\odot}$ (i.e., that are 'resolved' in the simulations) and that are within a 3D

radius r_{200m}, which is the radius that encloses a mean density that is 200 times the mean universal density at that redshift [i.e., $200\Omega_m(z)\rho_{\rm crit}(z)$]. Note that the derived velocity dispersions are not strongly sensitive to these choices, however, owing to the fact that the total mass distribution is fairly close to isothermal, and that the radial distribution of satellites is not a strong function of stellar mass (M16). For completeness, in table 3.1, I provide fits to the velocity dispersion–halo mass relation for various choices of mass definition and aperture (including both spherical and cylindrical radii) for selecting satellites.

3.1.2 Velocity dispersion calculation

With a tracer population in hand, I proceed to calculate the velocity dispersions of the simulated groups and clusters. There are several possible methods for calculating the velocity dispersion of a system (simulated or real), including calculating a simple root-mean-square (RMS) or fitting a normal distribution to the galaxy redshifts. I have decided to use the so-called 'gapper' algorithm (Wainer & Thissen, 1976), due to its practical application to observations (e.g., Eke et al. 2004; Robotham et al. 2011; Ruel et al. 2014; Proctor et al. 2015) and robustness at low richness (Beers et al., 1990). With the gapper method, the velocities are sorted from least to greatest and the velocity dispersion is then estimated as:

$$\sigma_{\rm gap} = \frac{\sqrt{\pi}}{N(N-1)} \sum_{i=1}^{N-1} w_i g_i, \tag{3.1}$$

with $w_i = i(N-i)$ and $g_i = v_{i+1} - v_i$, where N is the number of galaxies in the group or cluster, and v_i is the *i*th velocity from a list of the group's galaxies' velocities, that has been sorted in ascending order.

Although, statistically, the gapper method does not require the central object to be removed before calculation of the velocity dispersion, I have found that the mean gapper velocity dispersion is lower than the mean RMS velocity dispersion with the central removed. This is likely due to the central galaxy moving at a velocity that is not typical

of the satellite population. Therefore, I follow Eke et al. (2004) and scale $\sigma_{\rm gap}$ up by $[N/(N-1)]^{1/2}$ to account for these effects. Clearly, this correction is only relevant for low-mass groups with richnesses approaching unity, for which I have found that including this correction results in velocity dispersion estimates that are more stable to changes in the stellar mass cut used to select satellites. I use the symbol σ_v to denote the gapper velocity dispersion after it has been multiplied by the Eke et al. correction.

Although the simulation provides velocities in three dimensions, I limit this analysis to using only one dimension (I do not average the three one-dimensional velocity components) to replicate the information available in real observations. Therefore, σ_v is a 1-dimensional velocity dispersion. [1]

3.1.3 Effects of Baryon Physics

Predictions for the internal properties of groups and clusters (particularly of the gaseous and stellar components) are often sensitive to the details of the subgrid modeling of important feedback processes. One can attempt to mitigate this sensitivity by calibrating the feedback model against particular observables, as done in BAHAMAS. I anticipate that the velocity dispersions of satellites will be less sensitive to the effects of feedback than, for example, the gas-phase properties or the integrated stellar mass, since the dynamics of the satellite system is driven by the depth of the potential well which is dominated by dark matter. However, the total mass (dark matter included) of groups and clusters can also be affected at up to the 20% level with respect to a dark matter only simulation, if the feedback is sufficiently energetic e.g., Velliscig et al. (2014). The feedback will also reduce the masses of the satellites prior to accretion. The reduction of the satellite and host masses could, in turn, also affect the resulting spatial distribution of the satellites somewhat, and hence the velocity dispersion. Given these potential effects, it is therefore worth explicitly testing the sensitivity of the velocity dispersions to baryon physics.

[1] Due to a bug found post-publication of Caldwell16, σ_v needs to be divided by the correction factor of $\sqrt{(h)}$. This bug was introduced from a program, written by an external collaborator, that converts between comoving and physical units in the simulation. The velocity dispersions affected are in Chapter 3, and sections 4.1 and 4.2 in Chapter 4.

To test the sensitivity of the velocity dispersions to baryon physics, an important test was performed by Ian McCarthy. The (WMAP9) hydro simulation-based results are compared with those derived from a dark matter only version of the simulation (i.e., using identical initial conditions but simulated with collisionless dynamics only). To make a fair comparison with the dark matter only simulation, he selects the same satellite population as in the hydro simulations. In order to do this, first the stellar masses are assigned to the subhaloes using the subhalo abundance matching (SHAM) results of Moster et al. (2013). Specifically, the Moster et al. stellar mass–halo mass relation (including their estimated level of intrinsic scatter) is converted into a stellar mass–maximum circular velocity ($V_{\rm max}$) relation, using the M_{200}–$V_{\rm max}$ relation for centrals from the dark matter simulation. Then the stellar masses of all subhaloes (centrals and satellites) are estimated using this stellar mass–$V_{\rm max}$ relation. (The resulting galaxy stellar mass function from the dark matter simulation reproduces the observed SDSS galaxy stellar mass function well, as found in Moster et al. 2013.) Furnished with stellar mass estimates for the subhaloes, the same galaxy and group selection criteria are applied on the dark matter only simulation as imposed on the hydro simulations (as described in Section 3.1.1) and the velocity dispersions are estimated in the same way. Then the groups/clusters in the dark matter only simulation are matched to those in the hydro simulation using the dark matter particle IDs.

In Fig.3.1, I compare the mean fractional difference in the velocity dispersions between the hydro and the dark matter only simulations, plotted as a function of the dark matter only halo mass. For comparison, I also show the effect of baryon physics on the halo mass. Baryon physics (AGN feedback, in particular) lowers the halo masses of galaxy groups by $\sim 10\%$ (consistent with Velliscig et al. 2014) and also reduces the velocity dispersions by $\approx 5\%$, approximately independent of (the dark matter only) mass. Comparing these differences to the differences in the predicted VDFs for different cosmological models (see Fig. 3.2), the effect is not large but is also not negligible.

Therefore, if one plans to use velocity dispersions from dark matter only simulations (+SHAM), the velocity dispersions should be appropriately scaled down by $\approx 5\%$. Alternatively, if one starts from a halo mass function from a dark matter only simulation,

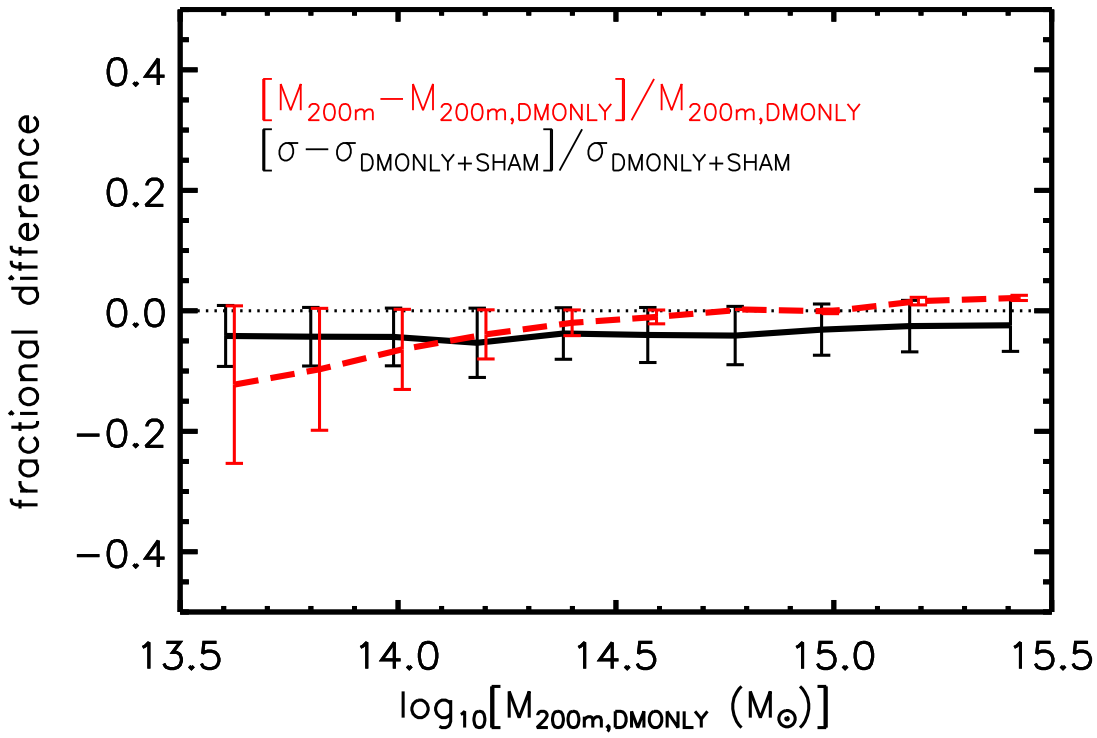

Figure 3.1: Mean fractional differences in the velocity dispersion and halo mass of matched haloes between BAHAMAS and a corresponding dark matter-only simulation (WMAP9 cosmology). The error bars represent the standard error on the mean. Note that I use subhalo abundance matching (SHAM) to assign stellar masses to subhaloes in the dark matter only simulations (see text), in order to apply the same selection criteria as imposed on the hydro simulations. Baryon physics (AGN feedback, in particular) lowers the halo masses of galaxy groups by $\sim 10\%$ (consistent with Velliscig et al. 2014) and also reduces the velocity dispersions by $\approx 5\%$.

the halo masses first need to be adjusted (e.g., as proposed by Velliscig et al. 2014) and then my hydro-simulated velocity dispersion–halo mass relation can be applied (including the scatter and evolution, as described below).

3.2 Velocity dispersion function

The velocity dispersion function (Φ), or VDF, is defined as the number of systems per unit comoving volume per decade in velocity dispersion; i.e., $\Phi \equiv \mathrm{d}n/\mathrm{d}\log_{10}\sigma_v$. In Figure 3.2 (top panel), I show the $z = 0$ VDFs for various cosmologies. The errors on the VDF are the square root of the number of groups in a velocity dispersion bin, divided by the volume of the simulation. The VDF clearly depends on cosmology, as expected. Note that the turnover in the VDF at low σ_v is due to the fact that I impose a richness cut of $N \geq 5$ on the simulated groups (i.e., each system must have at least 5 galaxies meeting the selection criteria noted in Section 3.1.1).

The lower panel of Figure 3.2 shows the ratios of the predicted VDFs with respect to that of the WMAP9 case with massless neutrinos. It more clearly demonstrates the strong cosmology dependence of the VDF. For example, at a velocity dispersion $\sigma_v \sim 1000$ km/s, adopting a Planck 2013 cosmology results in $\approx 50\%$ more systems compared to adopting a WMAP9 cosmology (both assuming massless neutrinos). Even at a relatively modest velocity dispersion of ~ 300 km/s (corresponding roughly to haloes with masses $\sim 10^{14}\mathrm{M}_{\odot}$) the difference is still significant ($\approx 20\%$). The introduction of massive neutrinos suppresses the number of high-velocity dispersion systems, as expected.

3.3 Number counts

Because the systems of interest have space densities of only $< 10^{-4}$ Mpc^{-3}, observational surveys covering a large fraction of the sky are required to detect massive systems in appreciable numbers. Given the limited statistics, splitting the sample into

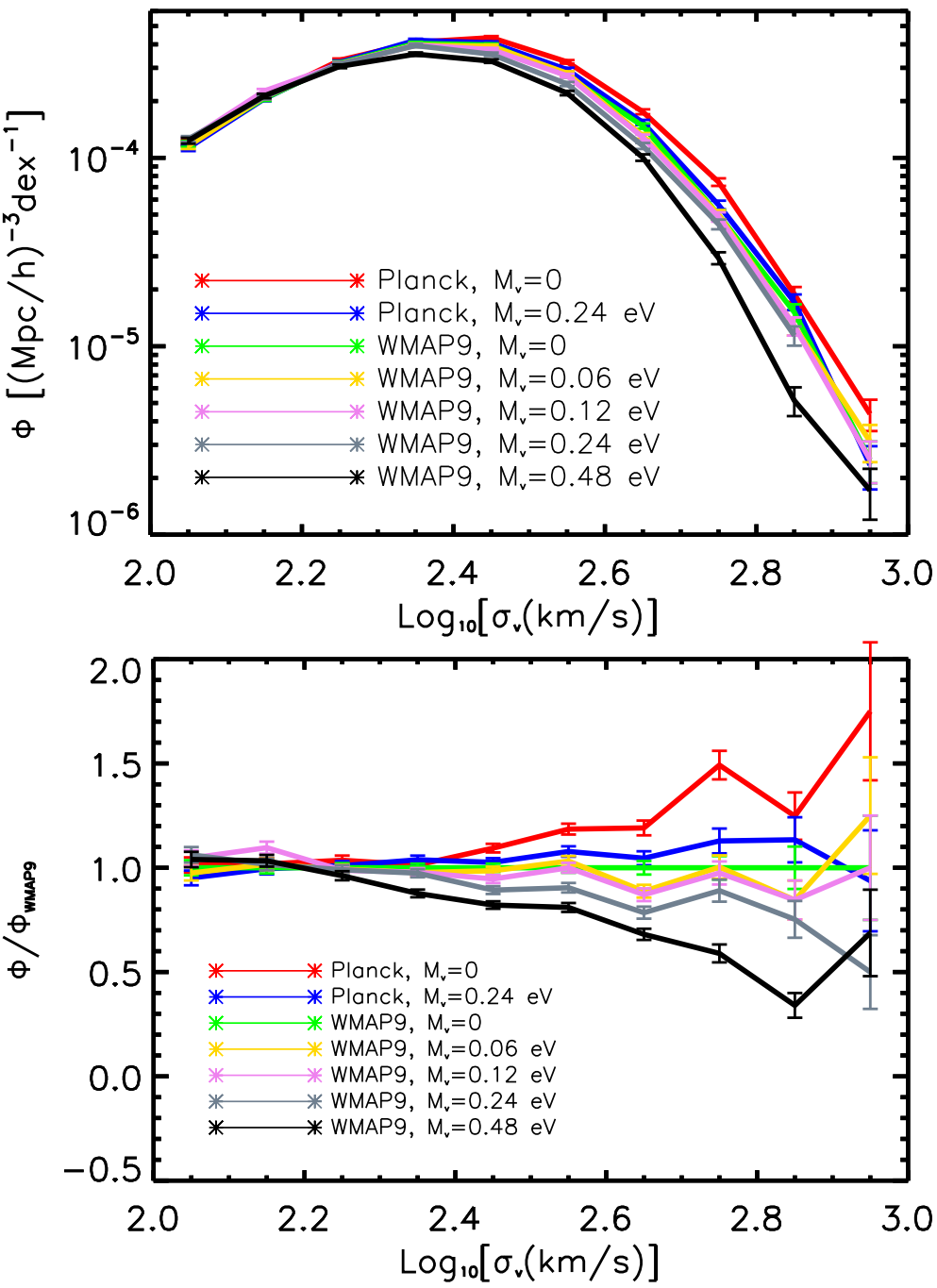

Figure 3.2: The predicted one-dimensional velocity dispersion function $\Phi \equiv \mathrm{d}n/\mathrm{d}\log_{10}\sigma_v$, or VDF, for the WMAP9 and Planck 2013 cosmologies for various choices of neutrino mass (including massless) at $z = 0$. The error bars represent Poisson sampling errors and are estimated as the square root of the number of systems in a given velocity dispersion bin divided by the simulation volume. The lower panel shows the ratio of the predicted VDFs with respect the WMAP9 case with massless neutrinos. Velocity dispersions are calculated using member galaxies within a 3D radius r_{200m} that have stellar masses $M_* \geq 10^{10}\mathrm{M}_\odot$. Only groups/clusters having at least 5 member galaxies are included, which is why the VDFs turns over at $\log_{10}\sigma_v(\mathrm{km/s}) < 2.4$. The predicted VDFs are a strong function of cosmology, like the halo mass function, but offer the advantage that velocity dispersions are directly measurable.

bins to measure a differential function, like the VDF, may not always be possible, particularly as one moves to higher redshifts. An alternative, therefore, is to measure the cumulative number counts above some threshold value in the observable. With this in mind, I show, in Figure 3.3, the number density of systems with $\sigma_v > 300$ km/s as a function of redshift for the various cosmologies considered in this work. This plot is analogous to the SZ number counts in Planck Collaboration et al. (2014) (see their Fig. 7). There is a clear stratification between the different cosmologies presented in this plot.

It is interesting to note that the velocity dispersion number counts do not drop off very steeply with redshift, in contrast to the halo mass counts. This is due to the fact that the radius enclosing a spherical overdensity mass (e.g., r_{200m}) decreases with increasing redshift (because the background density increases with increasing redshift), and hence the typical orbital velocity, which scales as $(GM/r)^{1/2}$, will increase for a halo of fixed mass with increasing redshift. The net result of this is that the number of systems above a given threshold value in velocity dispersion will not drop off as quickly as the number of haloes above a given halo mass threshold.

3.4 Scaling relations

3.4.1 Velocity dispersion–halo mass relation

Present-day relation

I model the mean relation between velocity dispersion and halo mass at a given redshift using a simple power-law of the form:

$$\langle \sigma_v | M_\Delta \rangle = a \Big(\frac{M_\Delta}{10^{14} \mathrm{M}_\odot} \Big)^b . \tag{3.2}$$

To derive the mean relation, I first compute the mean velocity dispersions in mass bins of width 0.25 dex. A power-law is then fit to these mean velocity dispersions. Note

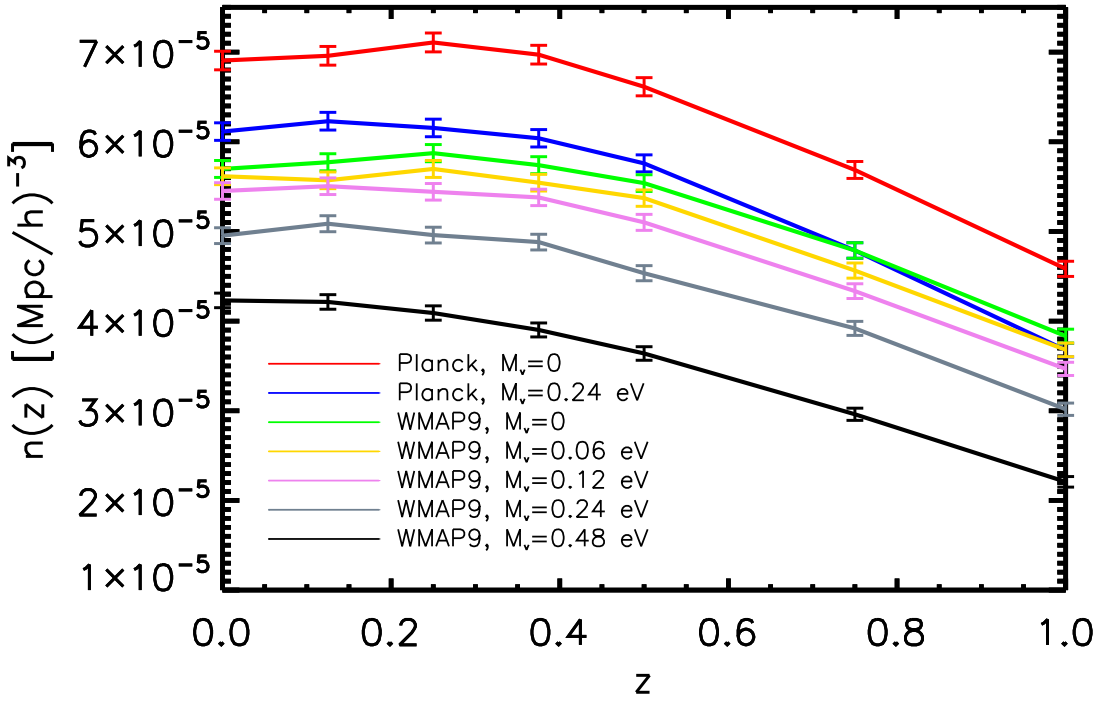

Figure 3.3: The number density of systems with $\sigma_v > 300$ km/s as a function of redshift for the various cosmologies that are considered in Figure 3.2. The error bars are the square root of the number of objects in a redshift bin, divided by the volume of the simulation.

that by deriving the mean velocity dispersion in bins of halo mass before fitting the power-law, I give equal weight to each of the mass bins. If instead, one were to fit a power-law to all systems, groups would clearly dominate the fit due to their much higher abundance compared to clusters. However, I want to accurately characterise the relation over as wide a range of halo masses as possible, motivating binning the data in terms of mass first.

In Figure 3.4, I show the velocity dispersion–halo mass relation for the Planck 2013 cosmology (with massless neutrinos). The small black dots show the individual groups and clusters, the red circles connected by a solid red curve show the mean velocity dispersions in halo mass bins, and the gold line represents the best-fit power-law to the mean relation (i.e., to the red circles).

The mean $z = 0$ σ_v–halo mass relation for this particular Planck 2013 cosmology simulation, adopting a group mass defined as M_{200m}, and selecting satellites within

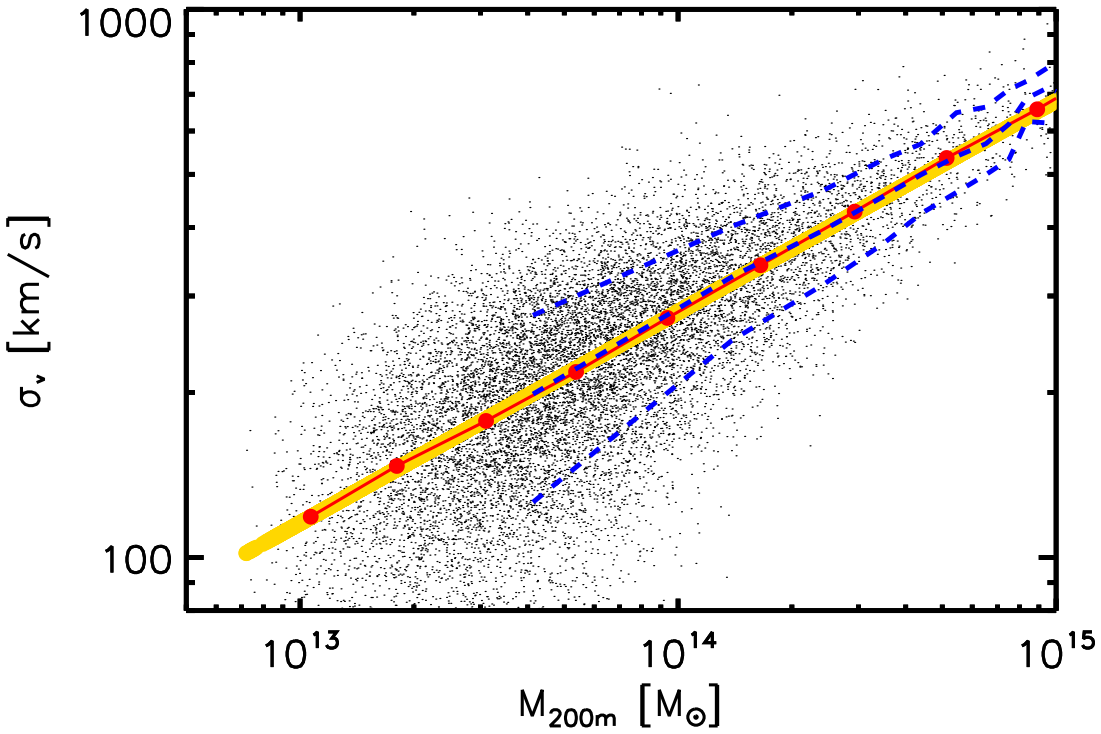

Figure 3.4: The velocity dispersion–halo mass relation for the *Planck* 2013 cosmology with massless neutrinos. Velocity dispersions are calculated using member galaxies within a 3D radius r_{200m} and that have stellar masses $M_* \geq 10^{10}\mathrm{M}_\odot$. The small black dots show the individual groups and clusters, the red circles connected by a solid red curve show the mean velocity dispersions in halo mass bins, and the gold line represents the best-fit power-law to the mean relation (i.e., to the red circles). The upper and lower dashed blue curves enclose 68% of the population. The mean relation and scatter are well-represented by a simple power-law relation with lognormal scatter.

r_{200m} with a minimum stellar mass of 10^{10} $\mathrm{M}_{\odot}$, is:

$$\langle \sigma_v | M_{200m} \rangle_{z=0} = 280.5 \pm 1.0 \ \mathrm{km/s} \left(\frac{M_{200m}}{10^{14} \mathrm{M}_{\odot}} \right)^{0.385 \pm 0.003}. \tag{3.3}$$

The errors quoted above are merely errors on the fit to the data and should not be used to reconstruct the σ_v–halo mass relation. A full description of modelling the spread of the distribution is presented in chapter 4.1.1. Note that although this relation was derived from simulations run in a Planck 2013 cosmology, the best-fit relations for other cosmologies I have examined are virtually identical. This likely just reflects the fact that once systems are virialized, the orbital motions of satellites are mainly sensitive to the *present* potential well depth and not to how that potential well was assembled (which will change with the cosmology). The lack of a cosmological dependence of the velocity dispersion–halo mass relation, at redshifts less than one, considerably simplifies matters, as it means one does not need to re-fit the relation for every cosmology and can just convolve this 'universal' relation with the halo mass function (which does depend strongly on cosmology, but for which there are many models in the literature for quickly calculating the HMF for a particular choice of cosmological parameters).

It is interesting to note that the best-fit relation has a slope of $b = 0.385$, which is comparable to the self-similar prediction of $1/3$. A similar finding has been reported recently by Munari et al. (2013), who also used cosmological hydro simulations to examine the velocity dispersion–halo mass relation (although they did not address the issue of velocity dispersion counts).

Furthermore, the best-fit *amplitude* differs significantly from that found previously by Evrard et al. (2008) for dark matter particles in pure N-body cosmological simulations:

$$\langle \sigma_v | M_{200m} \rangle_{\mathrm{Evrard+08},z=0} = 342 \pm 1 \ \mathrm{km/s} \left(\frac{M_{200m}}{10^{14} \mathrm{M}_{\odot}} \right)^{0.355 \pm 0.002}, \tag{3.4}$$

suggesting that the satellite galaxies have a $\approx -20\%$ velocity bias with respect to the velocity dispersion of the dark matter. M16 have confirmed this to be the case for BAHAMAS by comparing the satellite velocity dispersions to the dark matter particles

in the same simulation.

Is the mass–velocity dispersion relation derived from BAHAMAS realistic? As I have already argued, self-consistent simulations ought to be able to predict velocity dispersions as reliably as they can halo masses, so long as an appropriate selection is applied. However, one can also attempt to check the realism of the relation by comparing to observational constraints, noting the important caveat that observational halo mass estimates could have relevant systematic biases (which is what motivated the proposed use of velocity dispersion counts in the first place). Of the methods currently in use to estimate halo masses, weak lensing mass reconstructions are expected to have the smallest bias (of only a few percent) when averaged over a large number of systems (e.g., Becker & Kravtsov 2011; Bahé et al. 2012). M16 have compared the mean halo mass–velocity dispersion relation from BAHAMAS (using the same galaxy stellar mass selection as our fiducial selection employed here) to that derived from the maxBCG cluster sample (Koester et al., 2007), derived by combining the stacked velocity dispersion–richness relation of Becker et al. (2007) with the stacked weak lensing mass–richness relation of Rozo et al. (2009). Fig. 10 of M16 demonstrates the excellent agreement between the simulations and the observational constraints.

For completeness, in Table 3.1, I provide the best-fit power-law coefficients for the mean velocity dispersion–halo mass relation for different combinations of mass definition and aperture.

Cosmology independence

One benefit of using velocity dispersions to probe cosmology is the mean velocity dispersion–halo mass relation is generally insensitive to the choice of cosmology and uncertain subgrid (feedback) physics in the simulations. This means it can easily be used to convert masses to velocity dispersions or vice a versa without affecting the cosmological information contained within the data.

In Figure 3.5, I compare the mean relations for the *Planck* and WMAP9 (massless neutrino) cases (dashed orange and dotted green curves, respectively). The subgrid

physics model is identical in the two cases, the only difference is in the background cosmology. The trends are nearly identical.

The solid red and dashed blue curves represent the OWLS 'AGN' and 'REF' models (see Schaye et al. 2010) run in a $200\ h^{-1}$ Mpc box with 1024^3 particles (i.e., a factor of 8 better mass resolution than the BAHAMAS runs) in a WMAP7 cosmology. Neither of these models reproduce the galaxy stellar mass function, particularly the 'REF' model, which neglects feedback from black holes and suffers from strong overcooling at high halo masses. Since the mapping between stellar mass and halo mass differs strongly between the two runs and both differ strongly from the BAHAMAS runs (which do reproduce the GSMF), if one were to naively select satellites above a given stellar mass cut one would be selecting different tracer populations compared to the BAHAMAS analysis, which could result in a somewhat different relation (though the effect would not be very strong).

In any case, to rectify this mismatch the stellar masses are re-assigned in the 'AGN' and 'REF' runs using subhalo abundance matching results of Moster et al. (2013) by Ian McCarthy. Specifically, Moster et al.'s abundance matching, stellar mass–halo mass mapping (including intrinsic scatter) is applied to the central galaxies. The satellites are abundance matched using the M_{200}–$V_{\rm max}$ relation of centrals to infer M_{200} for the satellites, which is then used to assign a stellar mass. The simulations still reproduce the observed galaxy stellar mass function.

The derived mean velocity dispersion–halo mass relations for the two OWLS models are in good agreement with the BAHAMAS result, in spite of the differences in cosmology, resolution, and subgrid physics.

Note that cosmological independence does not extend to other cluster scaling relations. For example, in figure 3.6, the mean mass vs richness relation is shown for several cosmologies with and without SHAM. In the cluster regime, with halo masses greater than $10^{14}\mathrm{M}_{\odot}$, the WMAP9 results with baryons are approximately 35 percent higher than the abundance matched WMAP9 clusters. There is also a slight difference between the fully hydrodynamic simulations of Planck and WMAP9.

Therefore, not only is understanding the effects of subgrid physics and abundance matching employed in other simulations necessary before interpreting results, but a wise choice of observable must be made. Velocity dispersions have been shown to be an excellent tracer of mass, and can be used to estimate masses without losing cosmological information.

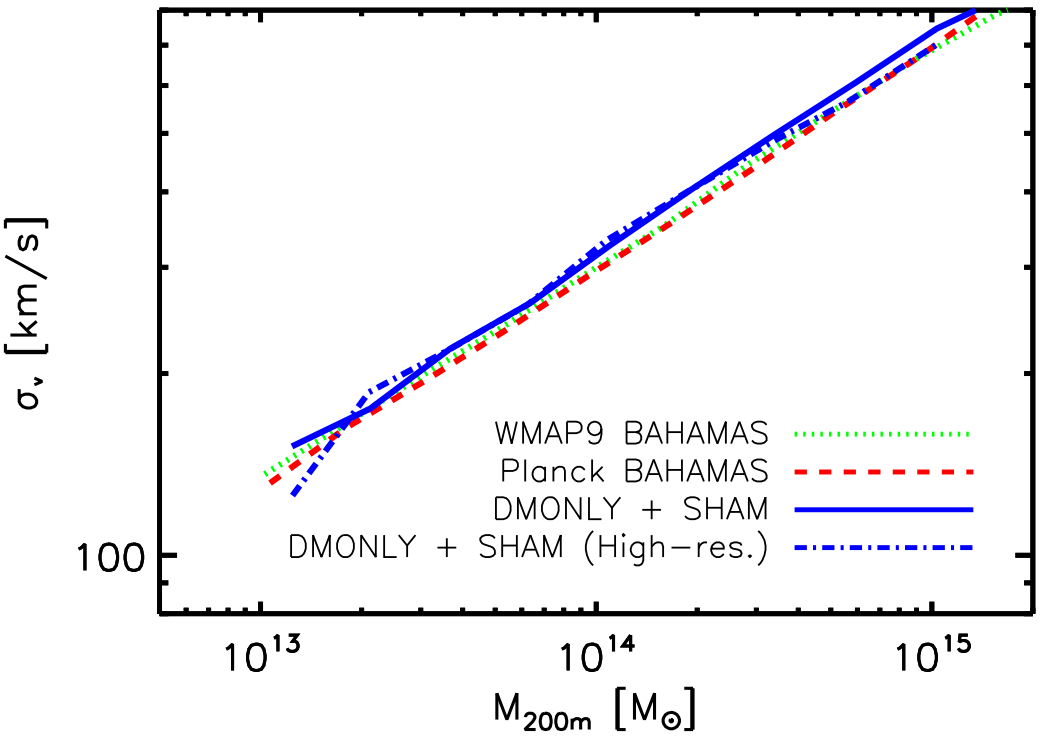

Figure 3.5: The mean halo mass–velocity dispersion relation for four models with different baryon physics and cosmology. The solid red curve and dashed blue curves represent the OWLS 'AGN' and 'REF' models (see text), while the dotted green and dashed orange curves correspond to the calibrated BAHAMAS simulations in WMAP9 and Planck cosmologies, respectively. The mean relation is generally insensitive to changes in background cosmology and feedback physics.

Evolution

To predict the evolution of the velocity dispersion counts, I need to know how the velocity dispersion–halo mass relation evolves with redshift. To estimate the evolution, I make the assumption that the galaxy groups are self-similar objects, essentially being the same object at different ages of the universe, so that the only thing that changes

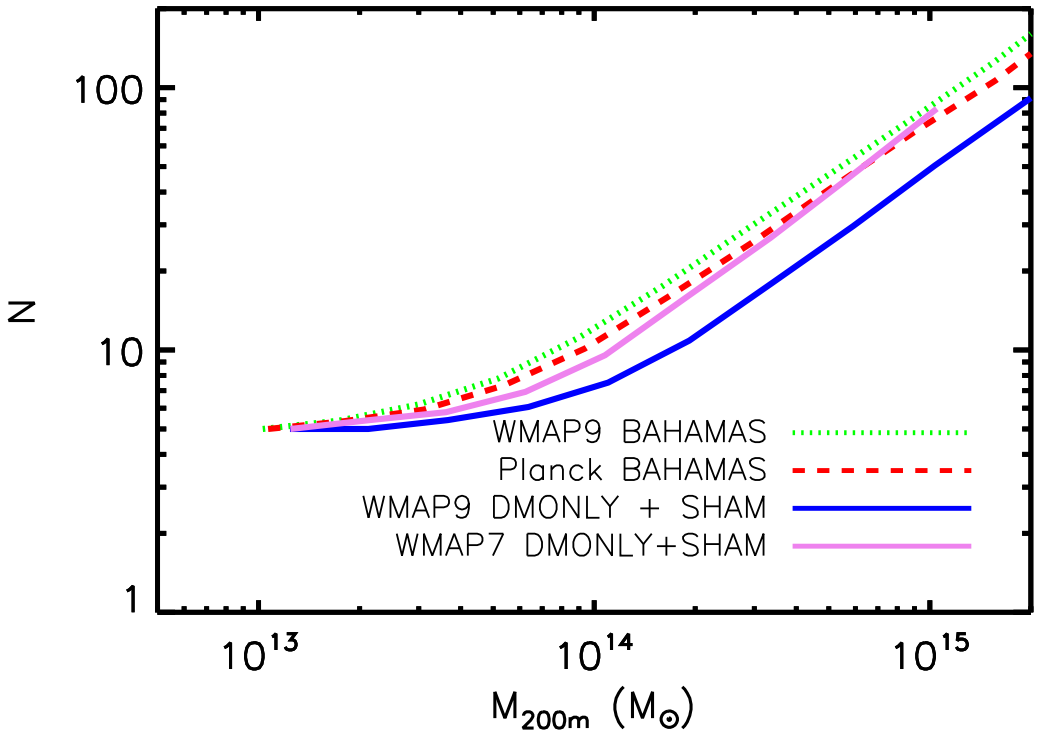

Figure 3.6: Unlike the velocity dispersion - mass relation, this figure shows that the mass-richness relation is sensitive to subhalo abundance matching. Here are the mass-richness mean relations is shown for three cosmologies: WMAP7, WMAP9, and Planck, and for two different methods of handling baryons, either through the subgrid models discussed in the simulation section, or by abundance matching. The difference between the top green dashed line(WMAP9) and its abundance matched analogue in blue, is approximately 35 percent. A clear separation between each cosmology is also apparent.

between a group at redshift 3 and a group at redshift 0.5 is its size, which is primarily due to the growth of the universe. Under the assumption of self-similar evolution, the typical orbital velocity of a halo of fixed spherical over-density mass evolves as $\sigma_v \propto E(z)^{1/3}$, where $E(z) = [\Omega_m(1+z)^3 + \Omega_\Lambda]^{1/2}$, if the mass is defined with respect to the critical density, or as $\sigma_v \propto (1+z)^{1/2}$ if the mass is defined with respect to the mean matter density. Note that even though I have already shown that the dependence on halo mass (the power-law index) at $z = 0$ is not exactly self-similar, this does not automatically imply that the redshift evolution of the amplitude will not be well approximated with a self-similar scaling. Indeed, such behavior is seen in other variables such as the X-ray luminosity–temperature relation, which displays a strong departure from self-similarity in the slope of the relation but, according to some current analyses, evolves at a close to self-similar rate (e.g., Maughan et al. 2012).

In the top panel of Fig. 3.7, I plot the mean velocity dispersion–halo mass relation at a variety of redshifts going back to $z = 1$. Clearly, there is a strong increase in the amplitude of the relation with increasing redshift. In the bottom panel of Fig. 3.7, I scale out the self-similar expectation, which has the effect of virtually removing the entire redshift dependence seen in the top panel. In other words, to a high level of accuracy ($\lesssim 2\%$), I find that the velocity dispersion–halo mass relation evolves self-similarly. This statement remains the case if one instead defines the mass according to the critical density and uses $E(z)^{1/3}$ as the self-similar expectation, as opposed to $(1+z)^{1/2}$, so that:

$$\begin{aligned} \sigma_v(M_{\Delta,\mathrm{mean}}, z) &= \sigma_v(M_{\Delta,\mathrm{mean}}, z=0)\,(1+z)^{1/2} \quad \text{, or} \\ \sigma_v(M_{\Delta,\mathrm{crit}}, z) &= \sigma_v(M_{\Delta,\mathrm{crit}}, z=0)\,E(z)^{1/3}. \end{aligned} \tag{3.5}$$

I note that although the assumption of self-similar evolution works spectacularly well in the case of velocity dispersions, it is not always so effective at explaining the evolution of observables. For an example, I demonstrate the ambiguous evolution of the temperature-mass relation in section 3.4.3. The compatibility of velocity dispersions

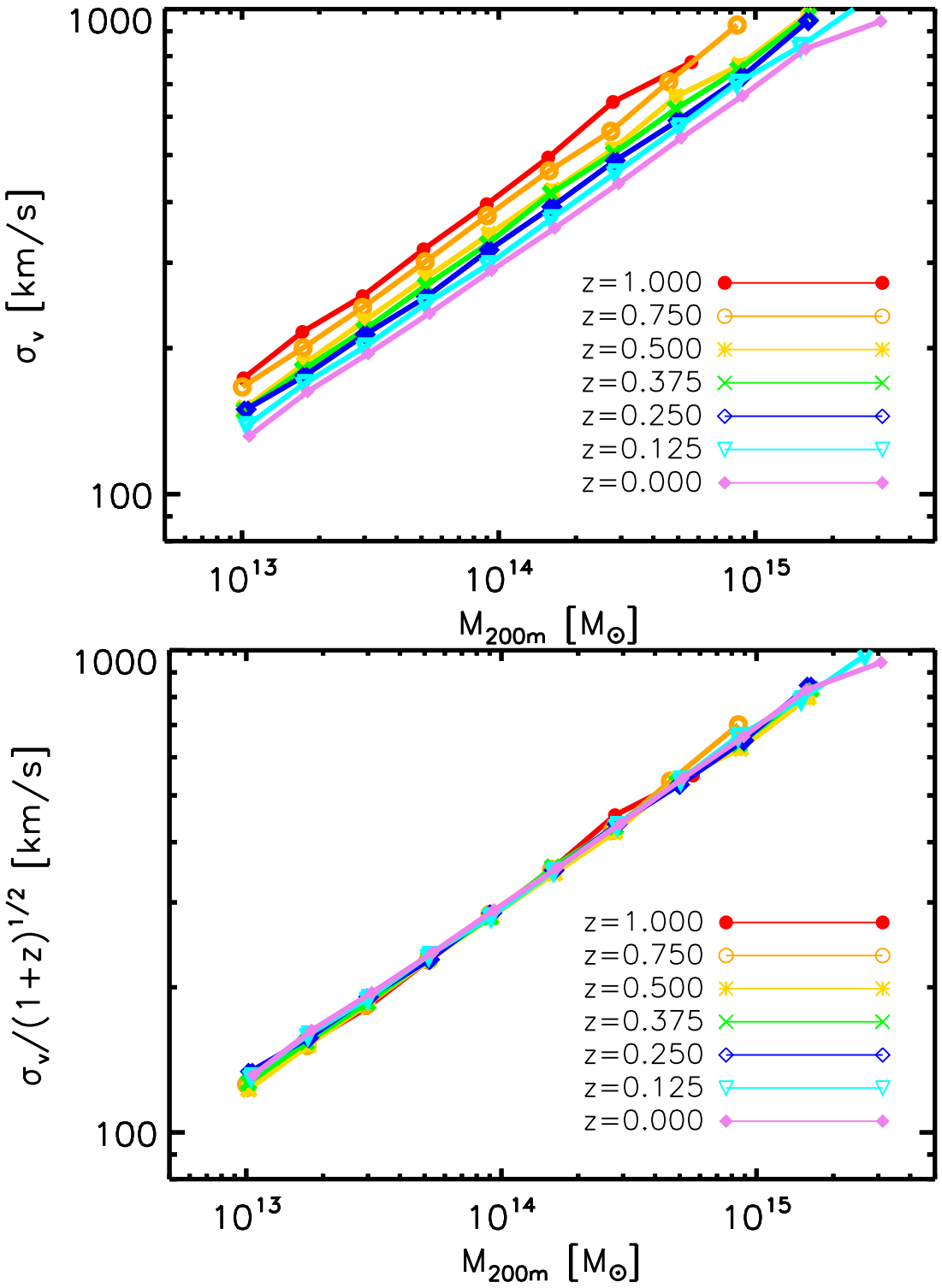

Figure 3.7: Evolution of the mean σ_v–halo mass relation back to $z = 1$. Velocity dispersions are calculated using member galaxies within a 3D radius, r_{200m}, and that have stellar masses $M_* \geq 10^{10}\mathrm{M}_\odot$. In the top panel I show the unscaled relations, while in the bottom panel the mean velocity dispersions have been re-scaled to account for self-similar evolution. The velocity dispersion–halo mass relation evolves at the self-similar rate to a high level of accuracy.

with the self-similar assumption should improve its reputation as a mass proxy, since one can select self-similar objects with certainty in velocity dispersion space.

Total scatter and its evolution

The scatter about the mean σ_v–halo mass relation is non-negligible at all masses and can be particularly large at low masses, due to poor sampling (as I will show below). Modeling this scatter is necessary if one wishes to predict the velocity dispersion counts by convolving the velocity dispersion–halo mass relation with a halo mass function, as Eddington bias will become quite important. Here, I characterize the scatter in the velocity dispersion as a function of halo mass and redshift.

To aid analysis of the scatter, I first divide the velocity dispersion of each system by that predicted by the best-fit power-law to our mean velocity dispersion–halo mass relation. After dividing out the mean mass relation, the residuals (see Fig. 3.8) clearly show that the scatter decreases with mass. To improve statistics, the velocity dispersions for different redshifts have been rescaled to $z = 0$ using equation 3.5, stacked, and binned to model the scatter as function of halo mass. The bin widths are chosen to equally sample the range in $\log_{10}$ halo mass space, while avoiding large statistical errors from low bin populations. The first four halo mass bins are 0.25 dex in width, increasing to 0.5 dex for the following two bins, and final bin has a width of 0.25 dex.

It is interesting to note that previous studies that used dark matter particles or subhaloes to estimate the velocity dispersions (e.g., Evrard et al. 2008; Munari et al. 2013) found that the scatter did not vary significantly with system mass. The difference between these works and the current one is that I select only relatively massive galaxies, which should be more appropriate for comparisons to observations. Since massive galaxies become increasingly rare in low-mass groups, the *statistical* uncertainty in the derived velocity dispersion increases. Studies that use dark matter particles (or, to a lesser extent, all dark matter subhaloes), on the other hand, have essentially no statistical error and therefore any scatter present is likely to be intrinsic in nature (e.g., due to differences in state of relaxation). These studies therefore suggest that the intrinsic

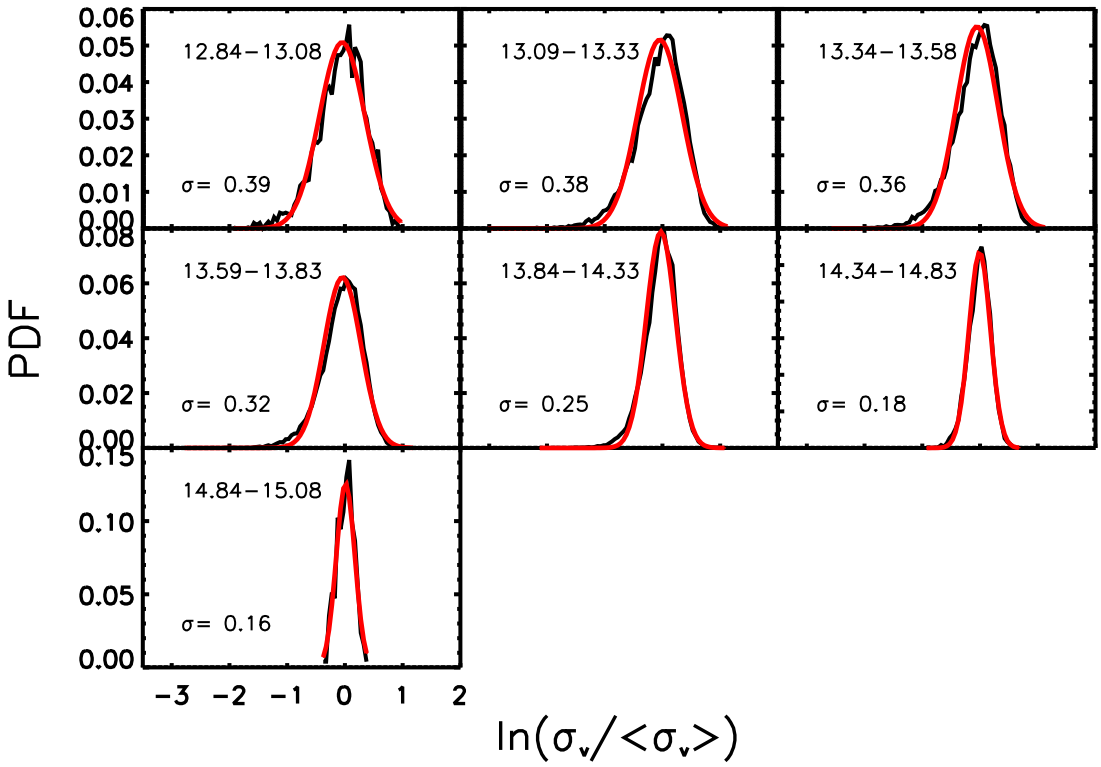

Figure 3.8: Residuals about the best-fit power-law to the mean velocity dispersion–halo mass relation. The 7 histograms correspond to different mass bins. The solid black curve represents the residuals about the mean, while the solid red curve represents the best-fit lognormal distribution. To boost our statistics, I stack the velocity dispersions from all redshifts and vary the binning in halo mass. Lognormal distributions describe the residuals about the mean relation quite well, but the width of the distribution (i.e., the scatter) about the mean decreases strongly with halo mass.

scatter does not depend significantly on halo mass, a finding which I confirm below.

I fit the total scatter residuals about the mean relation in each mass bin with a lognormal distribution. Fig. 3.8 shows histograms of logged velocity dispersion residuals, and the normal curve fit. A lognormal distribution describes the residuals well in all of the mass bins we consider. Note that in the first three (lowest) mass bins, the distribution becomes somewhat skewed relative to lognormal when systems with less than 5 members are included in the analysis. As discussed in Section 3.1.1, I have excluded these systems from our analysis, noting that when comparing to observed velocity dispersion counts from GAMA (Caldwell et al., in prep), I also plan to impose a richness cut of ≥ 5 on the observed sample.

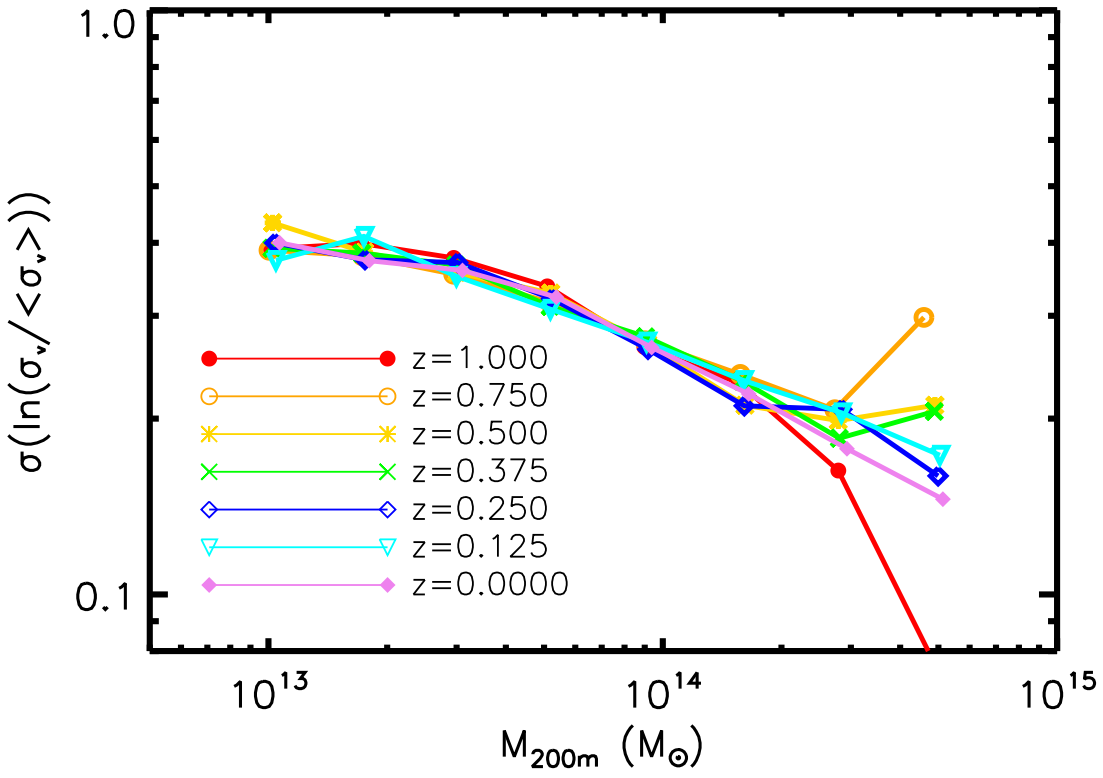

Figure 3.9: Evolution of the total scatter about the mean velocity dispersion–halo mass relation for seven redshifts from $z = 0$ to $z = 1$. There is no evidence for significant evolution in the scatter about the mean relation.

In Fig. 3.9, I show the evolution of the total scatter–halo mass relation for seven redshifts from $z = 0$ to $z = 1$. Here one can more clearly see that the scatter varies strongly with halo mass. However, it does not appear to vary significantly with red-

Table 3.1: Power law fits to the $z = 0$ σ_v–halo mass relation for *Planck* 2013 cosmology. Fits are of the form $\log_e(y) = a + b \log_e[M/10^{14}\mathrm{M}_\odot]$. The average intrinsic scatter is provided for each halo mass and aperture cut. The value for intrinsic scatter quoted below adds with the natural logarithm of statistical scatter in quadrature to equal the $\log_\mathrm{e}$ of total scatter for a group or cluster on the velocity dispersion-halo mass plane.

Halo mass	Aperture	σ_v–M intercept	σ_v–M slope	intrinsic scatter
$M_{500,mean}$	$R_{500,mean}$	5.7788	0.4003	0.1881
$M_{500,crit}$	$R_{500,crit}$	6.0084	0.4113	0.1897
$M_{200,mean}$	$R_{200,mean}$	5.6366	0.3852	0.1864
$M_{200,crit}$	$R_{200,crit}$	5.8220	0.4019	0.1906
$M_{200,mean}$	1 Mpc	5.6672	0.3986	0.1877
$M_{200,crit}$	1 Mpc	5.8138	0.3908	0.1877
$M_{200,mean}$	0.5 Mpc	5.7104	0.4060	0.1889
$M_{200,crit}$	0.5 Mpc	5.8583	0.4058	0.1889

shift, at least back to $z = 1$.

Now that the method for calculating the mean power law and scatter has been explained, I can present the power law coefficients for a range of popular overdensity values. Table 3.1, shows models for the velocity dispersion- mass relation and its scatter. Since the relation changes slightly depending on the distribution of the galaxies in the cluster, I have calculated the fits for several mean and critical mass definitions and cluster radii.

Summary of velocity dispersion–mass relation

Here I summarize our characterization of the velocity dispersion–halo mass relation for groups with at least 5 members with stellar masses $M_* \geq 10^{10}\mathrm{M}_\odot$. The mean relation can be well-described by a simple power-law spanning low-mass groups to high-mass clusters (see Fig. 3.4) is approximately independent of cosmology (for example, the amplitude for the mean $\sigma_v - \mathrm{M}$ power-law differs by $\approx 0.3\%$ between Planck and WMAP9 cosmologies). The mean power-law evolves self-similarly back to $z = 1$ at least (see Fig. 3.7). Note that the amplitude of the relation is $\approx 5\%$ lower than that predicted by a dark matter only simulation where a consistent selection of satellites is applied (see Fig. 3.1). The scatter about the mean relation can be well-represented by

a lognormal distribution whose width varies strongly as a function of halo mass (see Fig. 3.8) but not with redshift (see Fig. 3.9).

3.4.2 Velocity Dispersion - Richness relation

Powerlaw and comparisons with literature

Although quantifying the total scatter as a function of halo mass (in order to interpolate it with a halo mass function later) is the primary focus of this project, a deeper understanding of the scatter is required if one wishes to consistently compare with observations. That is because the scatter is composed of both intrinsic and statistical components and the latter is clearly going to be a function of observational survey parameters (e.g., limiting magnitude). Therefore, I must decompose the total scatter into its two components as a function of richness.

To begin, I proceed in a method similar to the one used to understand the velocity dispersion - mass relation in the previous section. First, I construct a mean power law from the trend in the simulated groups. Then I investigate the scatter, however, I continue the analysis a bit longer to decompose the scatter into two more fundamental groups, statistical scatter, which is determined by Poisson counting statistics and intrinsic scatter which is determined by astrophysical processes.

To model the mean velocity dispersion - richness relation, I once again assume, based on the distribution of the scatter plot, that it can be well modeled by a power law. Figure 3.10 shows the result of the power law fit, in yellow, to the mean bins of the simulated groups, in red. Blue contours enclosing 68% of the population indicate that the fit is well within the one-sigma interval of the points. I find a power law of :

$$ln(\sigma_v(km/s)) = 6.69 + 0.51(ln(N) - ln(100)), \tag{3.6}$$

describes this distribution well. In the following chapter, I show, in figure 4.7, that there is good agreement between the mean and 1 sigma contours of the GAMA groups

$\sigma - N$ relation and the simulated values. This agreement suggests that proceeding to compare these two surveys will produce accurate results.

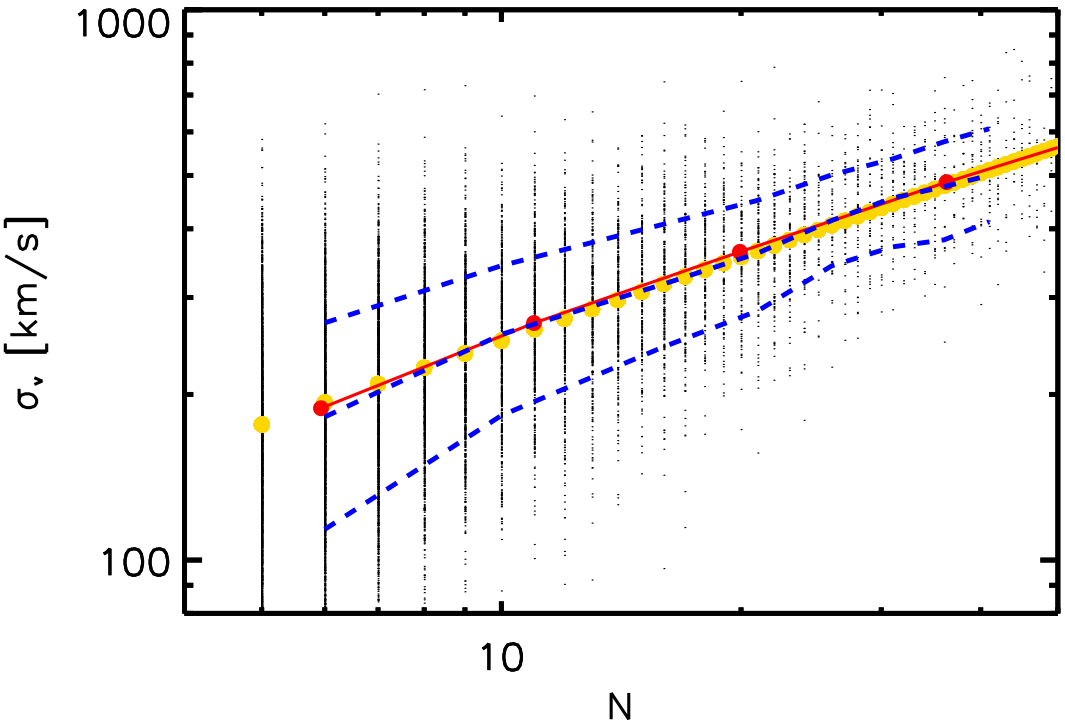

Figure 3.10: The velocity dispersion–richness relation for the *Planck* 2013 cosmology with massless neutrinos. Velocity dispersions are calculated using member galaxies within a 3D radius r_{200m} and that have stellar masses $M_* \geq 10^{10}\mathrm{M}_\odot$. The small black dots show the individual groups and clusters, the red circles connected by a solid red curve show the mean velocity dispersions in halo mass bins, and the gold line represents the best-fit power-law to the mean relation (i.e., to the red circles). The upper and lower dashed blue curves enclose 68% of the population. The mean relation and scatter are well-represented by a simple power-law relation with lognormal scatter.

Total scatter of the Velocity Dispersion- Richness relation and components

In section 3.4.1, I focused on the (total) scatter as a function of mass, but the statistical component is best understood through its dependence on richness, since fundamentally it is the number of tracers that determines how well the (true) velocity dispersion can be determined.

Similar to the previous investigation of scatter, I proceed by dividing the galaxy groups

by the mean relation to remove the richness slope. The residuals after this process are binned in richness and a normal curve is fit to the distribution of groups in that bin to determine the spread or width of the scatter. Figure 3.11 shows histograms of σ_v residuals are very well fit by a log normal curve (in red). The width of the log normal curve is the estimate of the scatter around the mean velocity dispersion - richness in that richness bin. The bin limits can be found at left corner of each plot.

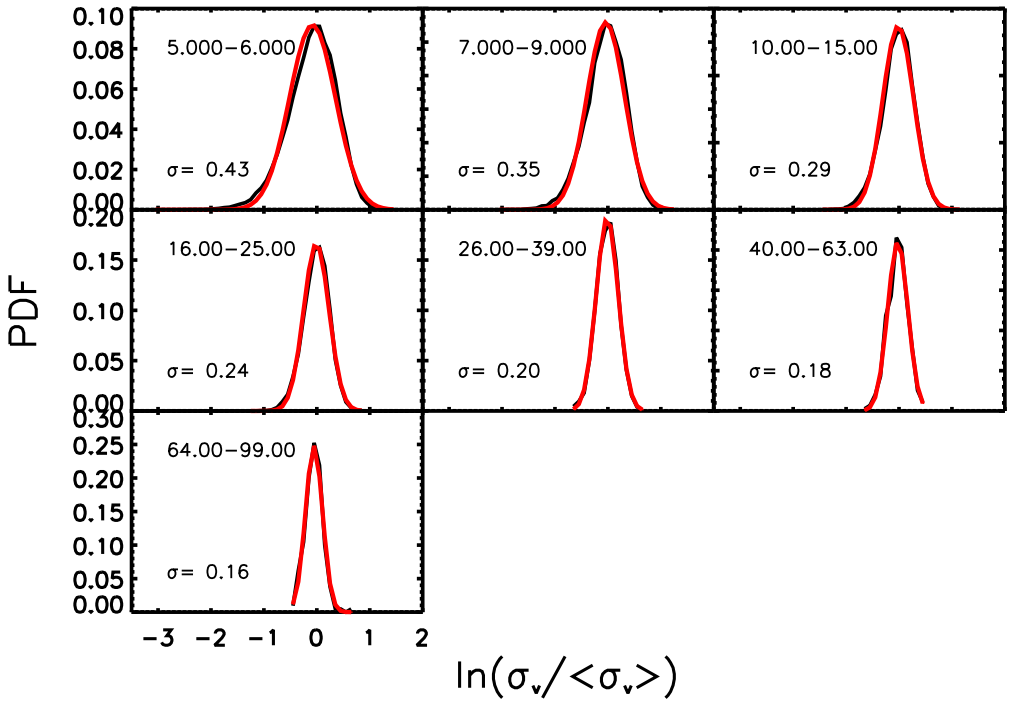

Figure 3.11: Residuals about the best-fit power-law to the mean velocity dispersion–richness relation. The 7 histograms correspond to different richness bins. The bin limits appear in the upper left corner of each plot. The histogram represents the residuals about the mean, while the solid red curve represents the best-fit lognormal distribution. To boost our statistics, I stack the velocity dispersions from all redshifts and vary the binning in richness. Lognormal distributions describe the residuals about the mean relation quite well, but the width of the distribution (i.e., the scatter) about the mean decreases strongly with halo mass.

Now, I investigate the sources of the total scatter: statistical scatter and intrinsic scatter. Statistical scatter is the scatter caused by randomly sampling a distribution with a finite number of points. In this particular case, sampling the velocity distribution of a galaxy group or cluster with a finite number of galaxies means that I can only measure the velocity dispersion to a certain level of accuracy. Clearly, the more tracer galaxies

one has, the more precise and accurate the measurement of the velocity dispersion will become.

To help understand the level of statistical scatter contributing to the total scatter, I use simple Monte Carlo simulations to determine the accuracy to which the velocity dispersion of a system can be determined given a finite number of tracers. I assume a normal distribution for the velocities and vary the number of tracers from 2 up to 1500 (which approximately spans the range of richnesses relevant for groups and clusters), drawing 1000 random samples for each number of tracers I consider. So, for example, to determine how well one can measure the velocity dispersion for a system with 5 members, I would randomly draw 5 velocities from a normal distribution and then compute the velocity dispersion using the gapper method. I repeat this 1000 times, each time recording the derived velocity dispersion. This gives a spread of velocity dispersions at fixed richness, which I then fit with a lognormal distribution. The width of this lognormal distribution is the statistical scatter in the velocity dispersion for a system with 5 members.

In Fig. 3.12, I plot the derived statistical scatter as a function of richness. As expected, the statistical scatter increases with decreasing richness. I find that for $N \geq 5$, the scatter is well modeled by a simple power-law of the form:

$$\sigma_{\rm stat}(\ln(\sigma_v)) = 0.07\Big(\frac{N}{100}\Big)^{-0.5} \text{for } N \geq 5 \tag{3.7}$$

This result is generally applicable for systems that have an underlying normal distribution, regardless of whether they are simulated or real clusters. Note that this does not depend on whether the multiplicative Eke correction is applied because the scatter is modeled in $\ln(\sigma_v)$.

Now I have a measurement of the statistical scatter at fixed richness. The total scatter is assumed to be composed of statistical and intrinsic components (summed in quadrature), so I can now also determine the intrinsic scatter as a function of richness.

In Fig. 3.13, I show the contribution of the statistical and intrinsic scatter to the total

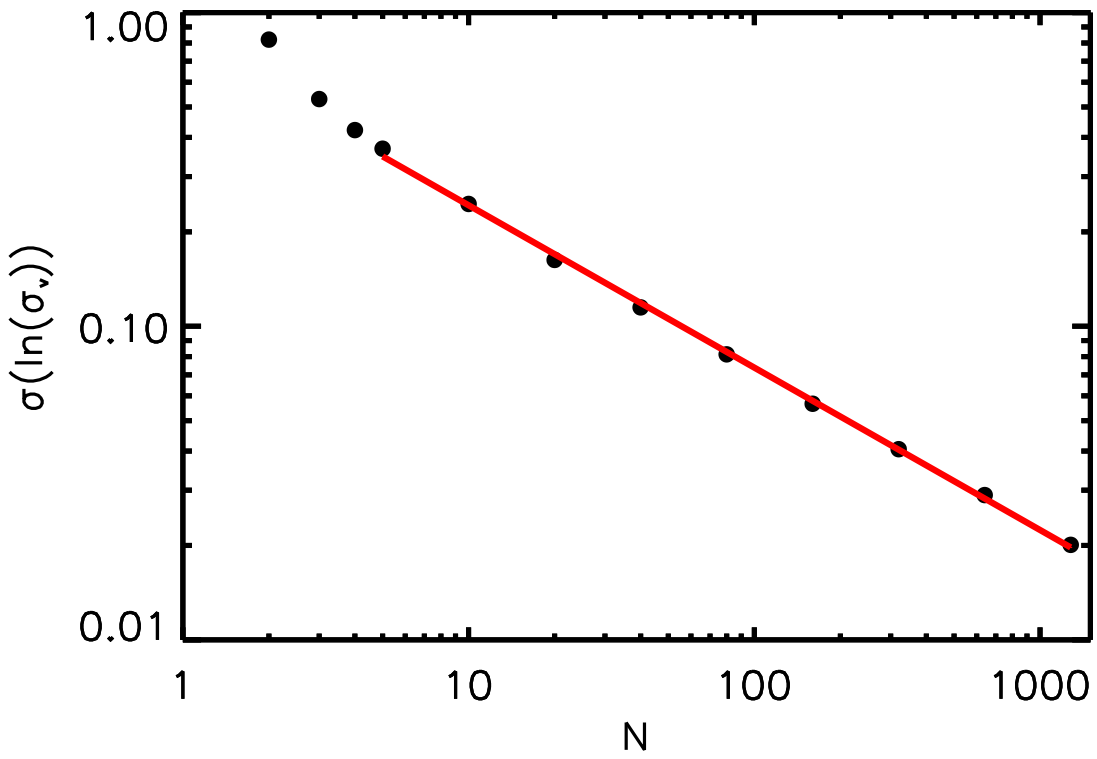

Figure 3.12: Statistical scatter as a function sample size, N, determined from Monte Carlo (MC) simulations (see text). The black points are the calculated value (derived from the MC simulations) for each sample size, and the red line is a power-law fit to the points with $N \geq 5$. A simple power-law relation works well for $N \geq 5$.

scatter as a function of richness. I find that statistical scatter dominates the total scatter for all but the richest (highest-mass) systems.

Note that it is galaxy selection criteria that determine the degree of statistical scatter. In the simulations, I use a galaxy stellar mass limit of $10^{10}\mathrm{M}_{\odot}$, but if one were able to lower that limit (e.g., by using higher resolution simulations) the statistical scatter would decrease. Likewise for observational surveys, if the apparent magnitude limit of the survey were increased (i.e., so that we could measure fainter systems), the number of galaxies will increase, and so too will the accuracy of the velocity dispersions. Other selection criteria (such as red sequence selection) can also affect the estimated velocity dispersion (e.g., Saro et al. 2013) via their influence on the number of tracers used to measure the velocity dispersion.

Note that while the statistical scatter is a strong function of richness, the intrinsic scatter does not vary significantly over the range of richnesses I have examined, consistent

with previous studies (e.g., Evrard et al. 2008; Munari et al. 2013). In table 3.1, I provide the mean intrinsic scatter for a variety of mass definitions and apertures. The average intrinsic scatter varies little with mass definition and choice of aperture with values ≈ 0.19 in $ln(\sigma)$.

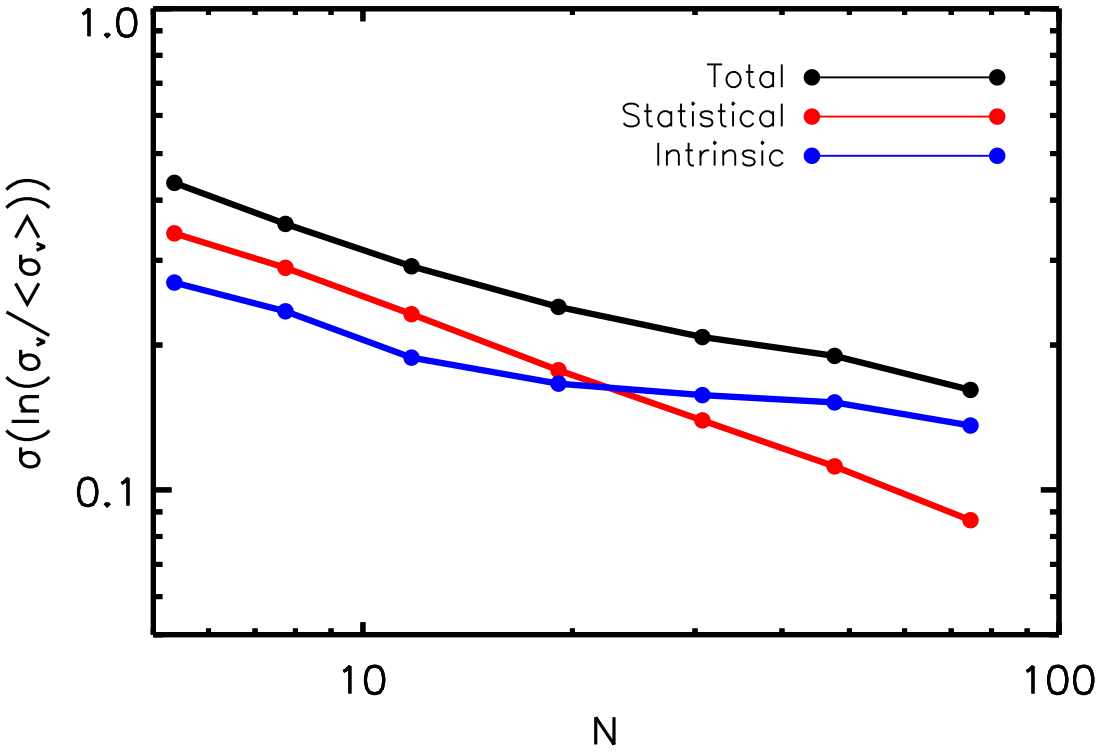

Figure 3.13: Contributions of intrinsic and statistical scatter to the total scatter about the mean velocity dispersion–richness relation, for the case of a *Planck* cosmology with massless neutrinos and selecting only groups with at least 5 member galaxies with stellar masses $M_* \geq 10^{10}\mathrm{M}_\odot$ and that are within r_{200m}. The black curve is the total scatter, the red curve is the statistical scatter, and the dashed blue curve is the derived intrinsic scatter (assuming the intrinsic and statistical scatters sum in quadrature to give the total scatter). Statistical scatter dominates for all but the most rich/massive systems. The intrinsic scatter does not depend strongly on richness/mass.

Summary of Velocity Dispersion- Richness relation

This subsection was an investigation of how the velocity dispersion of galaxy groups varies with the richness of the system. It was motivated by the need to understand the causes of the scatter in the velocity dispersion- mass relation. I find that the main cause of scatter in the velocity dispersions is due to statistical scatter. Therefore, richness

rather than mass is the natural way to understand the scatter.

I have shown that the mean velocity dispersion of groups increases with richness. This is due to the fact that as the number of galaxies in a group increases, so does mass, and as discussed in the previous subsection, velocity dispersions are dynamically related to the mass of the group or cluster. In Chapter 2, the N-M relation derived from simulation and the GAMA survey are in excellent agreement. This is promising for future comparisons with the GAMA survey which will be conducted in later chapters. I also showed that the scatter around the velocity dispersion-richness relation is composed of intrinsic and statistical scatter. The statistical scatter was modeled by a power law and is the dominant source of scatter in groups. The intrinsic scatter is relatively constant, and as a source of scatter, becomes more prevalent in clusters and larger groups. This information can be used to model the expected scatter in observational surveys.

3.4.3 Mass - Temperature relation

The following scaling relations were produced for the simulation comparison part for Susan Wilson's observational paper on X-ray scaling relations, Wilson et al. (2016). As she is an X-ray astronomer, the main analysis and interpretation was left to her. I provide my own brief context and analysis below.

Moving from optical probes of mass to X-ray, the temperature of the gas visible in the X-ray that surrounds a galaxy cluster is used as a tracer of cluster mass. The energetic state of the cluster describes the state of relaxation, that is, how closely the kinetic and potential energy of the cluster follow the Virial theorem. Instead of using the kinetic energy derived from the dynamics of the cluster, which was discussed in the previous section, one can use the kinetic energy from the gas temperature of the cluster to estimate the mass via the Virial theorem.

The Virial theorem says objects are in energetic equilibrium when twice the kinetic energy of the system is equal to the potential energy. In the case of a gravitationally

bound object, like a group or cluster, the potential energy is described by

$$-\Phi/2 = \frac{3}{2}\mathrm{kT}. \tag{3.8}$$

The gravitational potential, Φ, is equal to the gravitational constant times the mass of the cluster, divided by the radial distance from the center of the cluster. The average kinetic energy of a gas, derived from the ideal gas law, is related to the temperature as 3/2 kT. Where k is the Boltzmann constant, $8.6173324(78) \times 10^{-5}\mathrm{eVK}^{-1}$. Therefore, using the Virial theorem one can show that the potential energy, and therefore the mass of the cluster, is proportional to the temperature.

In this section, I calculate the mass -temperature (M-T) and investigate the evolution of the normalization. Then I construct the temperature-velocity dispersion (T-σ) scaling relation.

Powerlaw and comparisons to literature

To calculate the mass-temperature relation, I used the simulation run with a Planck cosmology and a group mass definition of 500 times the critical density of the universe at the time of the snapshot. The groups from the simulation are represented by grey dots in figure 3.14. These groups are binned in increments of 0.25 $\log_{10}$M500c and the mean value of the temperature is calculated for that mass bin. These mean temperature values are fit with a power law, described in equation 3.9, and pictured in figure 3.14 as the gold line.

$$\ln(\mathrm{kT(keV)}) = 1.204 + 0.523(\ln(\mathrm{M500c}) - \ln(3 \times 10^{14}\mathrm{M}_{\odot})) \tag{3.9}$$

The scatter about the mass-temperature relation is much smaller than the mass-velocity dispersion relation seen in the previous section. Presently, I have not conducted an investigation of the scatter around this relation, but will do in a future work.

The slope of the M-T relation found here to be ≈0.5 is in good agreement with Shimizu

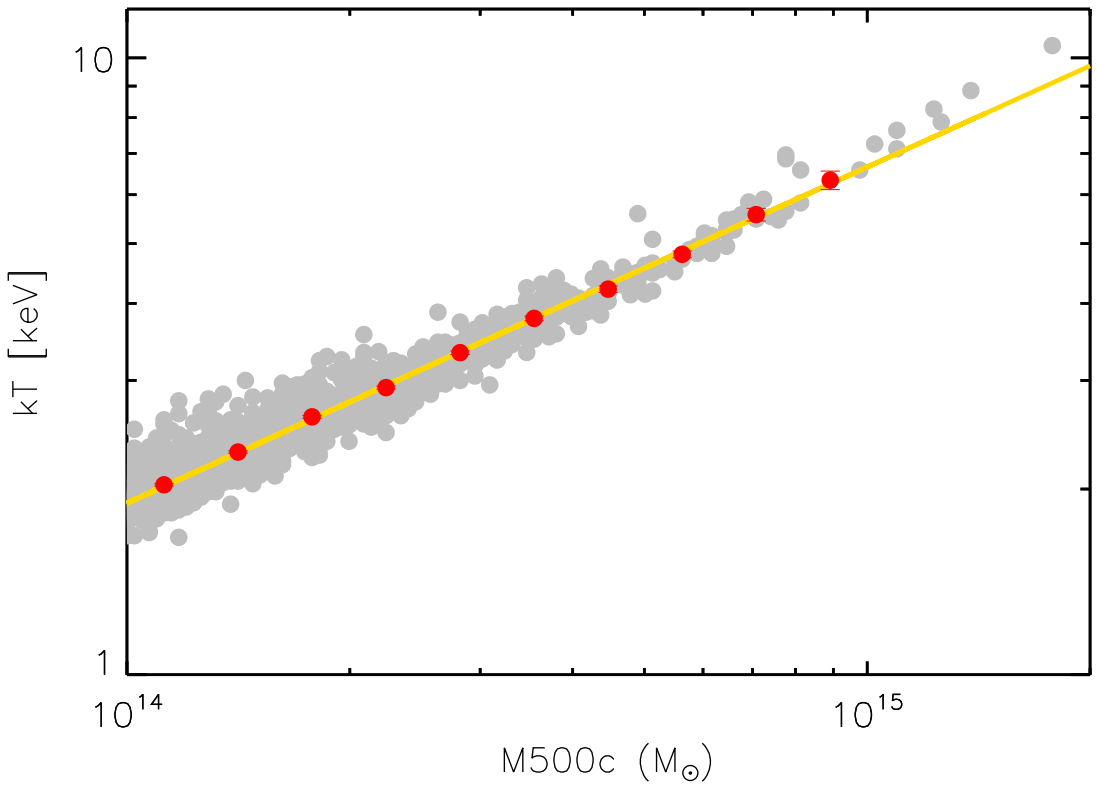

Figure 3.14: The mean power law fit to the temperatures and masses of clusters from BAHAMAS is shown in red. The underlying grey scatter points are the groups from the simulation. There is a small departure from the mean power law beginning around M500c=1e15 $M_\odot$. This could be an indication of more cluster-like processes becoming more dominant at that mass, indicating a need for an additional power law at high masses.

et al. (2003), and, in that paper's figure 4, also shown to be comparable to Finoguenov et al. (2001); Allen et al. (2001). Figure 4 in Shimizu et al. (2003) also shows that all of these slopes are shallower than the Virial relation suggesting that, on average, the gas is hotter in systems that have not reached equilibrium. A number of causes can be contributed to the additional heating of non Virialized systems, such as stellar or AGN feedback, or disturbance from a recent merger.

Evolution

The applicability of the self-similar scaling relation for the evolution of the mass - temperature relation is debatable. There are many examples in the literature of both observed (Shimizu et al., 2003; Finoguenov et al., 2001; Allen et al., 2001) and simulated (Le Brun et al., 2016) deviations from self-similarity. I also find that the evolution of the normalization of the temperature-mass relation is not best described by the self similar expectation of $T \propto M^{2/3}$. Figure 3.15, shows the effects of three different scalings of E(z): $1/2, 1/3$ and $2/3$ on the mean relation shown at redshifts ranging from one to the present.

In this figure, the bottom panel shows the effect of scaling the mean relations by the self-similar coefficient of $2/3$. Note that the mean relations do not return to the z=0 trend. A crude test of alternative scalings $E(z)^{1/3}$ (middle panel), and $E(z)^{1/2}$ (top panel), show that the relations scale best by $E(z)^{1/2}$. This slower than self-similar scaling is suggested, by Le Brun et al. (2016), to be caused by non-thermal pressure support that increases with redshift.

3.4.4 Velocity Dispersion - Temperature relation

The velocity dispersion - temperature relation is interesting, despite not returning a mass estimate, because it shows the relationship between the dynamics and energetic state of the group or cluster. It also allows a test of the baryon physics used in the simulation, because gas properties should be more closely linked to the particular recipe

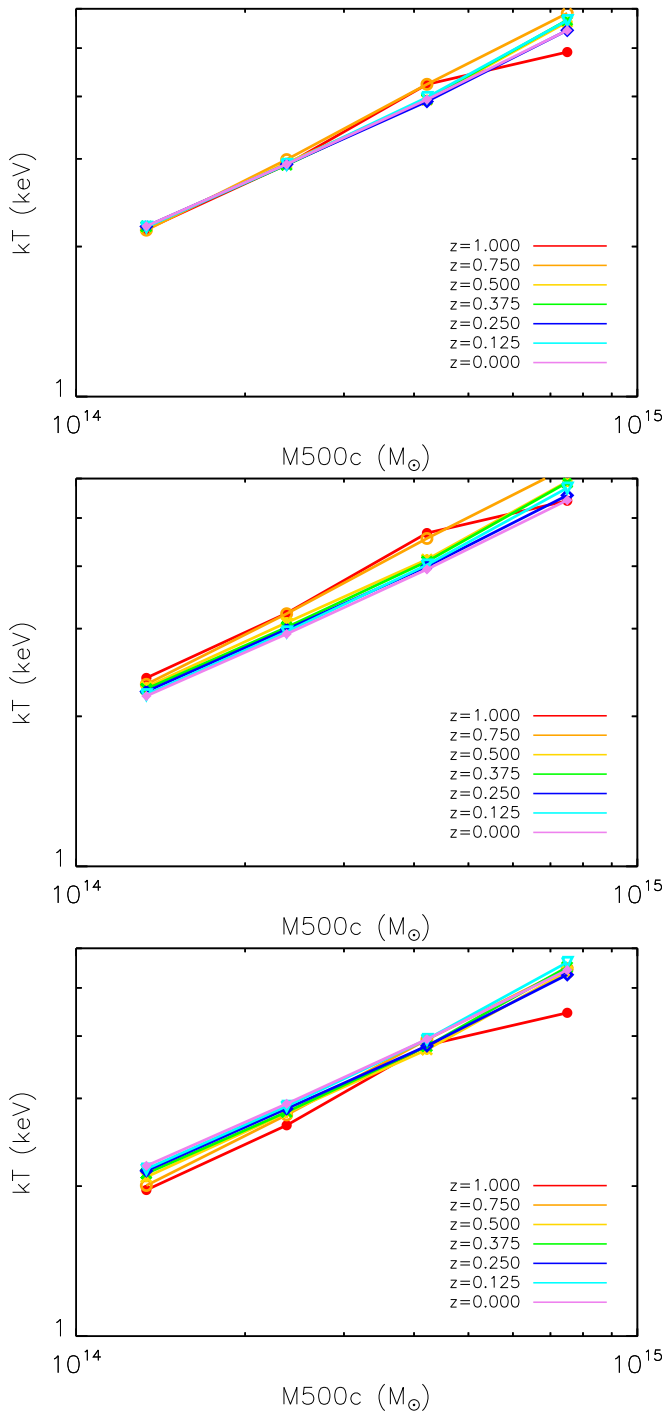

Figure 3.15: Here I show the effect of applying different exponential scaling factors of E(z) to the mean mass versus temperature relation. From top to bottom, the scalings of E(z) are 1/2, 1/3, and 2/3. A successful scaling would cause the mean relations to fall on the redshift zero line, however none of these scalings achieve this over the entire mass range. The best scaling of these three is $E(z)^{1/2}$,which is lower than the self-similar scaling relation.

of physics used. I have already shown that while velocity dispersions have high scatter, they evolve self-similarly, and the opposite can be said of temperature. Additionally, if the velocity dispersion is squared, a direct proportionality between velocity and temperature is expected. First, I will show the velocity dispersion - temperature relation and its evolution, because this is the plane commonly used in the literature, and then the relation with the squared velocity dispersion.

Powerlaw and comparison to literature

The velocity dispersions are calculated using the RMS velocity of all galaxies with $M_* > 5 \times 10^9 M_\odot$, by Ian McCarthy. A group mass limit imposed of M500c $> 1 \times 10^{14} M_\odot$ is imposed to be a realistic limit of current surveys out to z ≈ 1. Because of the large scatter in the velocity dispersions the T-σ relation is obtained using a method that attempts to minimize the effects of the scatter. First, the functions to σ-M500 and kT-M500 are fitted separately, and then their power law coefficients are combined to get σ-kT. The coefficients for the M-T relation are shown in section 3.4.3, and although, I have not shown the σ-M500c relation in this thesis, I have demonstrated the method in the previous section, and shown that changing aperture and mass definitions does not greatly affect the relation, see table 3.1.

In figure 3.16, the red powerlaw of σ-T relation is compared to the median and 1-σ contours (dashed blue lines) of the underlying distribution. Note that the points on the σ-T plane as shown were not used to fit the powerlaw, instead the powerlaw was derived from the σ-M500 and kT-M500 relations. Nevertheless, there is very good agreement between the underlying distribution and the powerlaw. The relation is described in equation 3.10. Additionally, in figure 3.17, the best fit slope is 1.09. The slope's proximity to unity indicates that the velocity dispersions and temperatures are finding the same potential well.

$$\ln(\sigma_v(\mathrm{km/s})) = 6.64 + 0.557(\ln(\mathrm{T}) - \ln(5\mathrm{keV})) \tag{3.10}$$

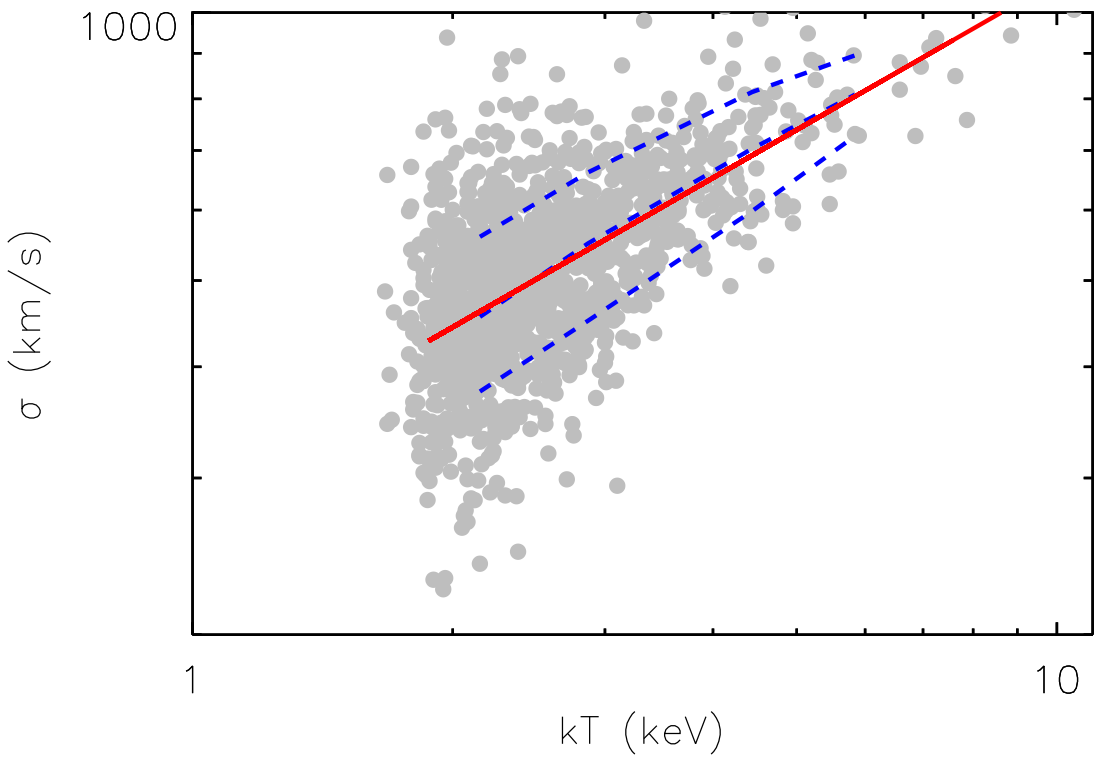

Figure 3.16: The velocity dispersion - Temperature relation from the BAHAMAS simulations is shown in red, as well as the 1-sigma upper, lower, and median contours in dashed blue lines. Despite the large scatter in velocity dispersion the mean, median, and underlying data points are in agreement.

Evolution

Unlike the M-T relation, the squared velocity dispersion versus temperature relation is very well constrained since because both quantities scale like the energy of the system, the scalings should cancel. Figure 3.18 shows that without any scaling, such as E(z) used in previous sections, the mean trends at redshifts up to redshifts of 0.75 very closely coincide.

3.4.5 Summary of Temperature as a mass proxy

In the previous two sections, I looked at the relationship between X-ray temperature and Mass, and then compared the temperature to another mass proxy to test baryon physics models, and see if both estimates of gravitational potential agree, on average.

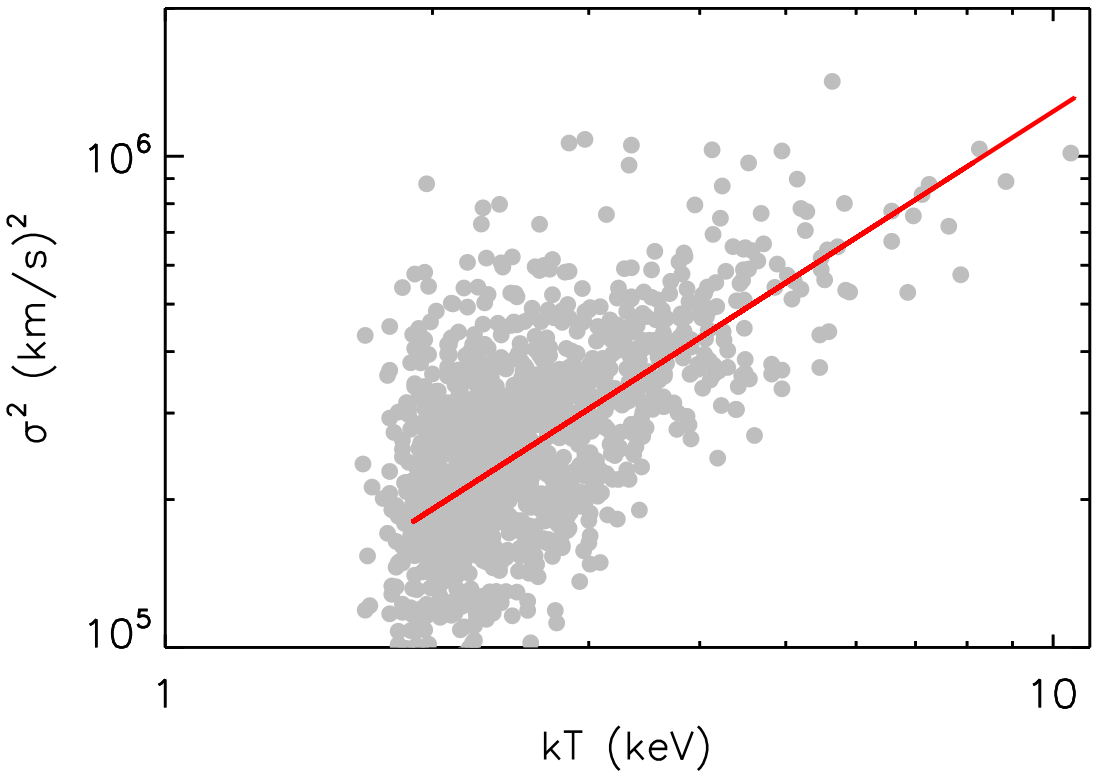

Figure 3.17: The mean powerlaw fit to the the velocity dispersion squared versus the temperature in keV.

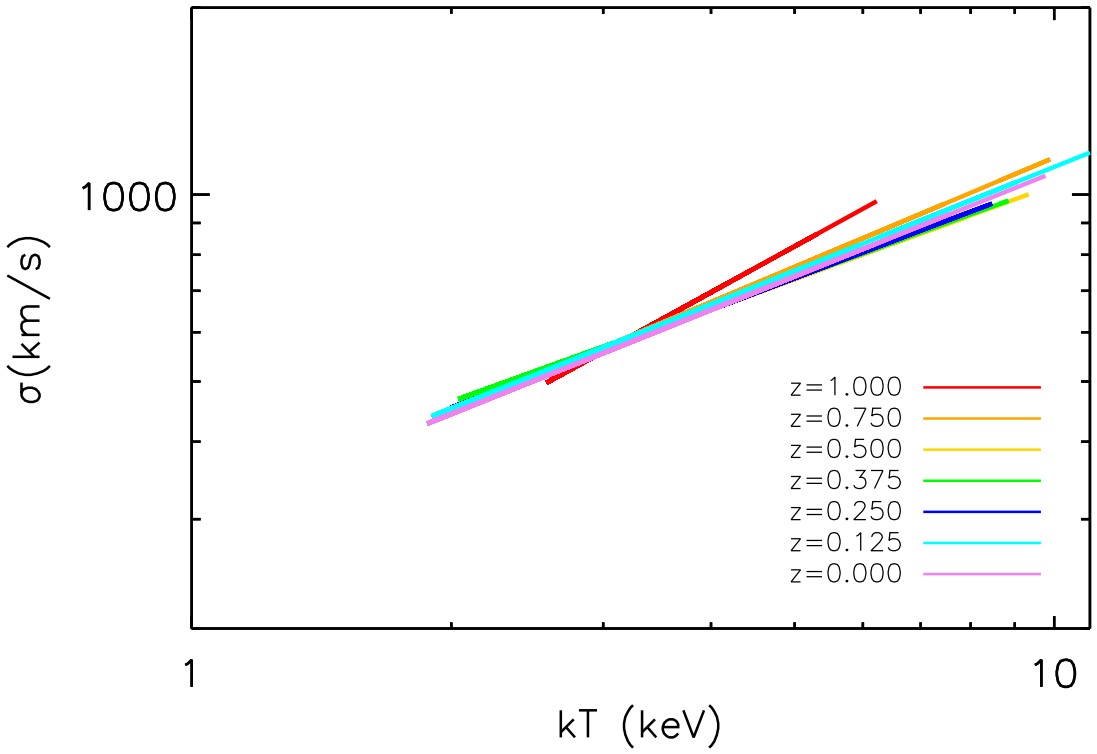

Figure 3.18: Here I show the redshift evolution of the velocity dispersion versus temperature relation is minimal due to both quantities representing the same thing; the energy of the system.

First I found that the X-ray temperature and Mass relation has much less scatter than the velocity dispersion - mass relation. Therefore if one uses temperature as a mass proxy, the mapping is more certain than with velocity dispersion. However, when examining the evolution of the M-T relation, I found that it did not scale self-similarly. This has been confirmed by previous studies in the literature. I found that a E(z) scaling factor of 1/2 produces a better result than the self-similar scaling of 2/3. Then, I used my previous analysis of σ-M and M-T to construct a mean powerlaw for σ-T and σ^2-T. The quantities in the latter relation both are proportional to the energy of the system, and should have a slope of unity and not evolve with redshift. I find, for the groups in the BAHAMAS simulations, that both of these requirements are met. This ensures that both σ and T are measuring the potential of the group, and that the choice of subgrid physics in BAHAMAS is not dramatically affecting the gas properties in groups.

3.5 Summary of the properties of Galaxy Groups and Clusters from Simulation

Two common mass proxies are the velocity dispersion and temperature. I begin with a discussion of the necessary selection criteria that must be imposed to make a observationally realistic sample, and I discuss the effects of baryon physics on the observables, and show that velocity dispersions are more robust to various choices of baryon physics (fig. 3.1) because velocities are more closely linked to the dark matter halos than energetic processes. However, as a discussion later in the chapter shows, the gas temperatures in the BAHAMAS simulation yield similar results to the velocity dispersions (fig. 3.17), and are still reliable tracers of the potential.

I calculated the mean σ-M powerlaw (fig. 3.4) and looked at the evolution of this mean trend as a function of redshift (fig. 3.7). I found that it evolves self-similarly, which is not a trait that other observables, such as the T-M relation share (fig. 3.15). I also look at the scatter around the σ-M and σ-N relations (figs. 3.8, and 3.11, respectively). The total scatter around the σ-M relation is large at masses less than $1 \times 10^{14}\mathrm{M}_{\odot}$.

It does not appear to evolve with redshift (fig. 3.9). The dominant source of scatter at low masses is due to statistical scatter (fig. 3.12). Lower mass groups tend to have less galaxies in them, and the lack of tracers produces a large uncertainty when determining velocity dispersions. Mass dependent scatter was not found in previous studies using simulations. This is because they were looking primarily at larger groups that are intrinsic scatter dominated. I find a similar result when looking at more massive and rich groups. When N is large enough ($>$10 galaxies) to determine the velocity dispersion accurately, the remaining source of scatter, is constant with respect to mass.

I also ask the reader to consider velocity dispersions as physical quantities, and argue that they can, like mass, be used to probe cosmology. I show that the velocity dispersion function (fig. 3.2) and number counts from velocity dispersions (fig. 3.3) are sensitive to changes in cosmological values. There is a statistically significant separation between WMAP9 and Planck cosmologies and between several different values of neutrino mass. In Chapter 4, I will use the discriminating power of velocity dispersions to constrain cosmological values from the GAMA survey.

Chapter 4

Constraining Cosmological Parameters

4.1 Predicting the velocity dispersion counts for different cosmologies

In the previous section, I calculated, directly from the simulation, cluster number counts as a function of velocity dispersion and redshift for seven different combinations of cosmology and neutrino masses. The computational expense of running large simulations like BAHAMAS prohibits us from running a dense grid of cosmologies for comparison with observations, which is ultimately necessary to determine not only the best-fit cosmology, but also the uncertainties in the best-fit cosmological parameters. I therefore require a means to rapidly compute the predicted velocity dispersion counts for many different cosmologies.

Here I propose a method to combine the results of the simulations with the halo model formalism to predict the velocity dispersion counts. Specifically, I show that when the mean and scatter of the mass-sigma relation are convolved with the distribution of halo masses in the simulations, it closely predicts the velocity dispersion counts. One can therefore take advantage of popular theoretical models for the halo mass function (e.g.,

Sheth et al. 2001; Tinker et al. 2008), provided they are appropriately modified for the effects of baryon physics (e.g., Cui et al. 2014; Velliscig et al. 2014), and my velocity dispersion–halo mass relation to quickly and accurately predict the velocity dispersion counts as a function of cosmological parameters.

4.1.1 Testing the model

I now test the accuracy of our simple velocity dispersion–halo mass relation model by convolving it with the halo mass distribution drawn from the simulations and comparing the predicted velocity dispersion distribution with the one drawn directly from the simulations. In particular, for the model prediction, I use the mass of each halo to infer the predicted mean velocity dispersion using eqns.3.3 and 3.5. I then (additively) apply scatter by randomly drawing from a lognormal distribution with a width set by the total scatter–halo mass relation, which is characterized by the black curve in Figure 3.13.

Figure 4.1 compares the VDF derived directly from the simulations with that predicted by my simple model of the velocity dispersion–halo mass relation convolved with the halo mass distribution, both imposing a richness cut of $N \geq 5$. I also show the effect of ignoring the scatter in the velocity dispersion–halo mass relation. In spite of its simplicity, the model prediction (with scatter) reproduces the simulation VDF remarkably well (to better than 10-15$\%$ accuracy) over the full range of velocity dispersions that we sample. By contrast, ignoring the scatter causes the curve to strongly under predict the VDF above velocity dispersions of 300 $\mathrm{km\,s^{-1}}$. Modeling the scatter is therefore crucially important if one wishes to make an accurate prediction for the velocity dispersion counts and obtain unbiased constraints on cosmological parameters.

In Figure 4.2, I compare the evolution of the velocity dispersions counts for systems with $\sigma_v \geq 300$ km/s from various simulations with different cosmologies with that predicted by my simple model. There is good agreement with between model predictions and the simulations.

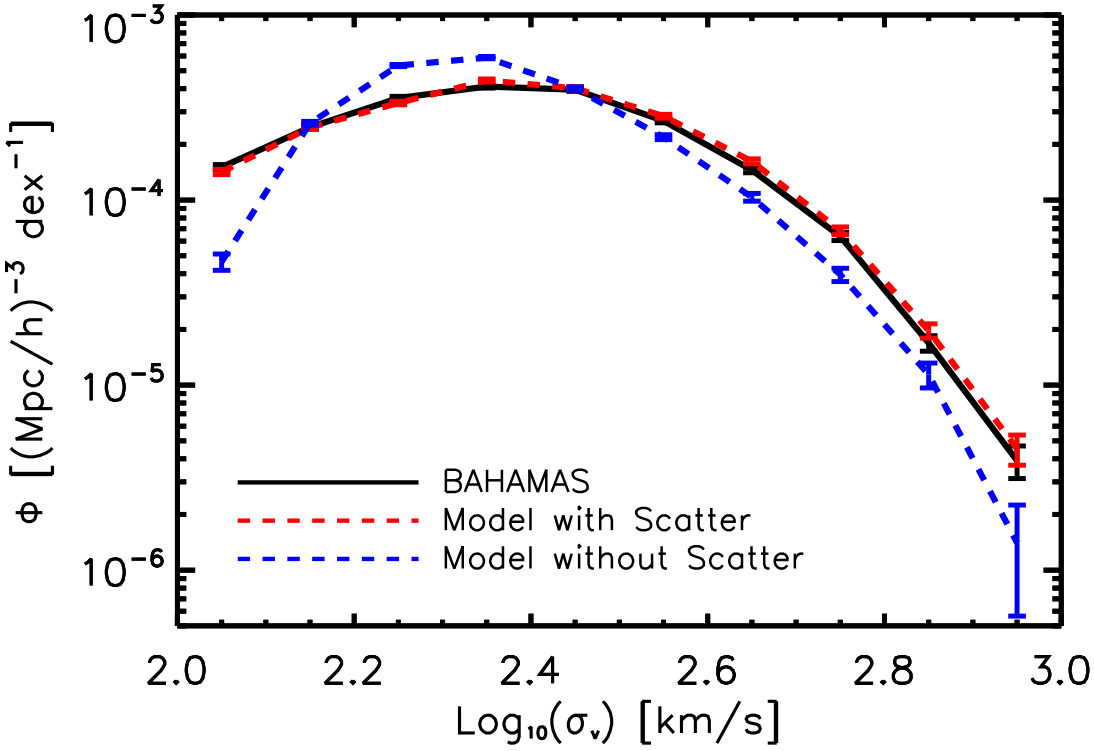

Figure 4.1: Comparison of the VDF from the Planck 2013 (massless neutrino) simulation (solid black curve) with that predicted by a simple model of the velocity dispersion–halo mass relation convolved with the halo mass distribution from the simulations (red dashed curve). Also shown is the model prediction when the scatter in the velocity dispersion–halo mass is ignored (blue dashed curve). The model with scatter reproduces the simulation VDF quite well over the full range of velocity dispersions. Ignoring the effects of scatter and associated Eddington bias leads to an underestimate of the number of systems with velocity dispersions exceeding 300 km s^{-1}.

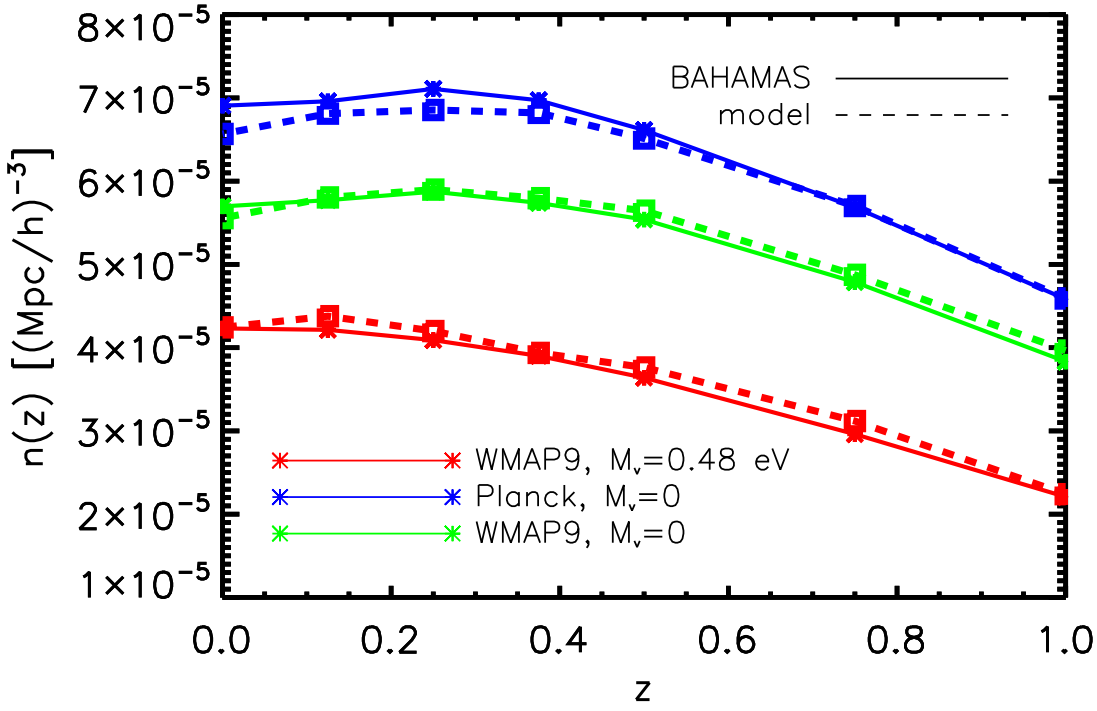

Figure 4.2: The number density of systems with $\sigma_v \geq 300$ km/s as a function of redshift. Solid lines are from the simulation, dashed lines are velocity dispersions constructed from the models described in the previous section and convolved with the halo mass function from the BAHAMAS simulation. The colors indicate different cosmologies: blue=Planck, green= WMAP9, and red = WMAP9 with neutrino mass = 0.48 eV.

Finally, note that in the above analysis the effects of feedback have already implicitly been included. As demonstrated in Section 3.1.3, feedback can affect both the halo mass and the velocity dispersion. Therefore, in order to predict the velocity dispersion function from the halo mass function one must appropriately account for feedback effects on the halo mass and then apply the above velocity dispersion–halo mass relation. The modification of the halo masses is already implicitly included in my analysis, as we use the halo mass distribution directly from the hydro simulations. If, however, one wishes to use theoretical mass functions in the literature that are based dark matter simulations (e.g., Sheth et al. 2001; Tinker et al. 2008) appropriate feedback modifications should be applied (such as those proposed by Velliscig et al.).

4.2 Cosmological constraint forecasts

In Section 4.1, I outlined a simple yet accurate method for predicting the velocity dispersion counts for different cosmologies. Here I use this apparatus to make some simple forecasts for current and future spectroscopic surveys. In particular, I examine the kind of constraints that these surveys will place on the σ_8–Ω_m plane and on the summed mass of neutrinos.

I consider three different synthetic spectroscopic surveys, with characteristics chosen to approximately match those of the completed GAMA survey (Driver et al., 2011), the upcoming WAVES-Wide survey (Driver et al., 2015), and the upcoming DESI bright galaxy survey (Levi et al., 2013). For the synthetic GAMA-like survey, I adopt a survey field of view of 180 square degrees and galaxy stellar mass limit of $10^{10}\mathrm{M}_{\odot}$. For the synthetic WAVES-like survey, I adopt 1000 square degrees and a stellar mass limit of $10^{9}\mathrm{M}_{\odot}$. For the synthetic DESI-like survey, I adopt 14,000 square degrees and a stellar mass limit of $10^{10}\mathrm{M}_{\odot}$. For all three cases, I examine the cosmological constraints that can be derived using the velocity dispersion number counts exceeding 300 $\mathrm{km\,s^{-1}}$ within a redshift $z < 0.2$. Note that it may be possible to obtain improved constraints by looking at multiple thresholds in velocity dispersion and/or multiple redshift bins, which I intend to explore further in future work.

4.2.1 The σ_8–Ω_m plane

I construct a 151×151 grid of [σ_8,Ω_m] values ranging from $0.7 < \sigma_8 < 0.9$ and $0.2 < \Omega_m < 0.4$. For the other parameters, we adopt a 'WMAP9-based' cosmology, fixing $h = 0.7$, $\Omega_b = 0.0463$, $n_s = 0.972$ and $\Omega_\Lambda = 1 - \Omega_m$. For a given set of cosmological parameters (of which there are 22801 independent sets), I use CAMB to compute the $z = 0$ linear transfer function, which is used as input for the Tinker et al. (2008) halo mass function. I convolve the predicted halo mass function with the halo mass–velocity dispersion relation derived in the previous sections. Note that for the case of the synthetic WAVES-like survey, I have decreased the statistical scatter in the

velocity dispersions in line with the adopted lower stellar mass limit of that survey. This was done by using the abundance matching procedure described in Section 3.1.3 to estimate how much the richnesses would increase by dropping the stellar mass limit from $10^{10}\mathrm{M}_{\odot}$ to $10^{9}\mathrm{M}_{\odot}$.

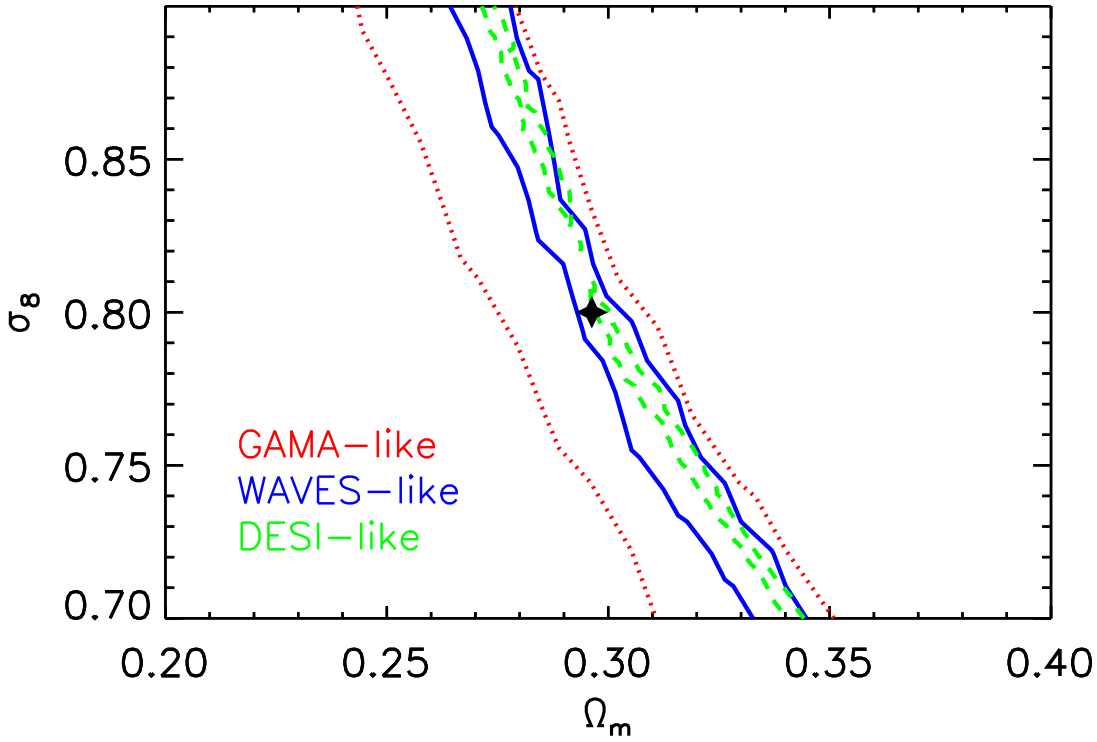

Figure 4.3: Forecasted constraints on σ_8 and Ω_m using the velocity dispersion number counts. Dashed contours define the 1-σ confidence interval for the GAMA-like, WAVES-like, and DESI-like synthetic surveys that we consider. The black star indicates the adopted test cosmology. The joint constraint scales approximately as $\sigma_8\Omega_m$ (see text). The amplitude can be determined to approximately 20%, 10% and 4% accuracy with the GAMA-like, WAVES-like, and DESI-like synthetic surveys, respectively.

Figure 4.3 shows the 1-σ confidence interval for a test cosmology of $\sigma_8 = 0.8$ and $\Omega_m = 0.3$; i.e., I assume these are the truth and see how well this is recovered. The 1-σ confidence interval shows a strong degeneracy in the joint constraints on σ_8 and Ω_m, as expected. I find that a simple power law with $\sigma_8 \propto \Omega_m^{\alpha}$ with $\alpha \approx -1$ describes the degeneracy relatively well. The exact slope of the degeneracy depends somewhat on which synthetic survey is considered; I find $\alpha = -0.86 \pm 0.01$, -1.08 ± 0.01, and -1.13 ± 0.01 for the GAMA-like, WAVES-like, and DESI-like surveys, respectively.

It is worth noting that the degeneracy found here is significantly steeper than that found

in some previous halo mass counts studies, which indicate $\alpha \approx -0.6$ (e.g.,Vikhlinin et al. 2009; Rozo et al. 2010). The reason for this difference is not that I am using velocity dispersions as opposed to halo mass, but is instead due to the specific velocity dispersion threshold of 300 $\mathrm{km\,s^{-1}}$ that I adopt. In particular, this velocity dispersion threshold corresponds roughly to a halo mass of $\sim 10^{14}\mathrm{M}_{\odot}$, which is lower than most current halo mass counts studies (certainly compared to X-ray- and SZ-based studies). Note that the abundance of groups is somewhat more sensitive to Ω_m than to σ_8, whereas the reverse is true for high-mass clusters. I have verified that using higher velocity dispersion thresholds leads to a flatter degeneracy between σ_8 and Ω_m, similar in shape to that found previously for studies based on massive clusters. This motivates my comment above, that one can potentially use multiple velocity dispersion thresholds to help break the degeneracy between the two cosmological parameters.

It is immediately evident from Figure 4.3 that upcoming spectroscopic surveys will severely constrain the amplitude of the degeneracy. I can quantify this by comparing the width of the 1-σ confidence interval (i.e., the width perpendicular to the degeneracy) to the best-fit amplitude. I find that a GAMA-like survey would be expected to constrain the amplitude to $\approx 20\%$, whereas a WAVES-like survey would constrain it to $\approx 10\%$ and a DESI-like survey would constrain it to better than 4% accuracy.

Note that in the above analysis I have held the other cosmological parameters fixed. Allowing these to be free will likely broaden the constraints on σ_8 and Ω_m slightly.

A recent study by Ntampaka et al. (2016) that also uses velocity dispersions of clusters to constrain cosmological parameters found the slope of the $\sigma_8\Omega_m$ interval to be 0.29. The slope from my work is much steeper, even for the 180 square degree survey, and as the width of confidence interval, which biases our slope fitting function, shrinks with increased survey volume, the value of the slope converges to 1.105, which is very different from the value in Ntampaka et al. (2016). A possible explanation for this is although there is agreement between the slopes of the σ_v – Mass relation in the two studies, the normalization for this work is much lower, even after accounting for differences in mass normalization. One significant difference between the two studies is Ntampaka et al. (2016) has a mass limit of 3.5 $\times 10^{14}\mathrm{M}_{\odot}\mathrm{h}^{-1}$, while my

model extends to groups with $\mathrm{M}_{200m} > 7 \times 10^{12}\mathrm{M}_{\odot}$. The extra information at lower masses may affect the normalization, however, other studies velocity dispersion studies of higher mass clusters, such as Evrard et al. (2008), find the normalization of the $\sigma_v - -\mathrm{M200m}$ relation to be closer to my value of ≈ 300 km s^{-1}. Finally, in addition to the subtleties of the simulations used in either work, the method of calculating confidence intervals varies between the two studies. While I use a minimum delta χ^2 interval, the Ntampaka et al. (2016) study uses a confidence interval derived from a covariance matrix. However, one would expect to recover relatively similar values from either statistical approach.

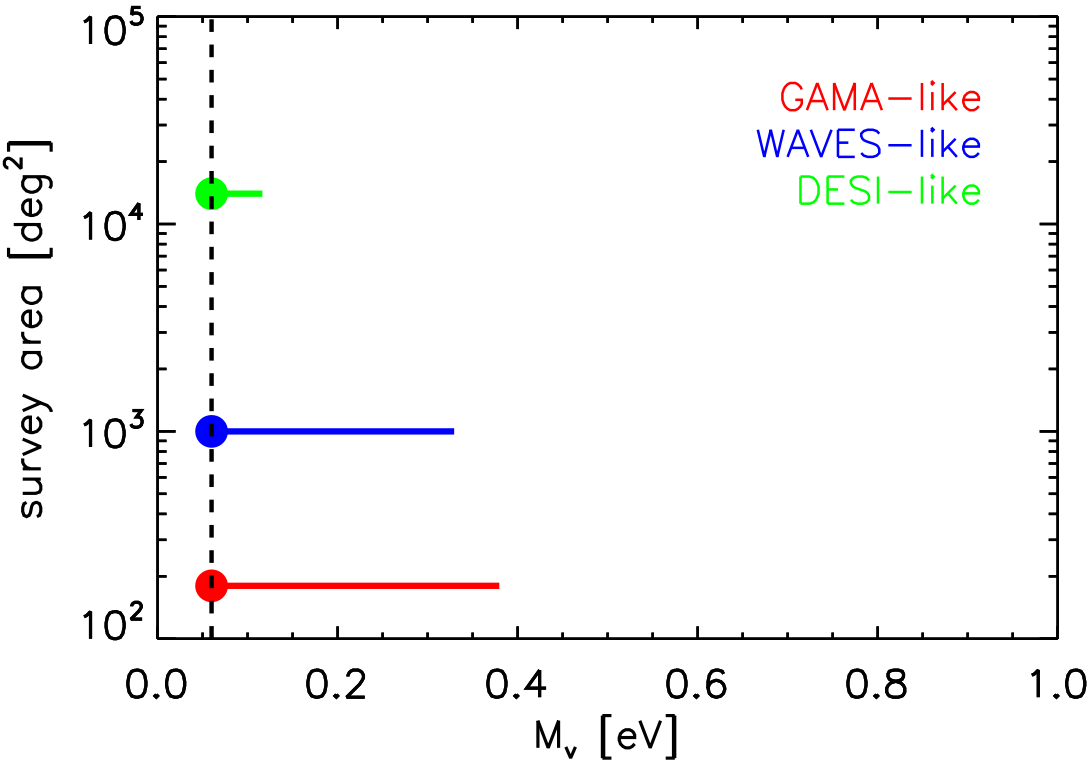

Figure 4.4: Forecasted constraints on the summed mass of neutrinos, M_ν. The 1-σ confidence intervals are plotted in red, blue and green for the GAMA-like, WAVES-like, and DESI-like synthetic surveys that I consider. I adopted $M_\nu = 0.06$ eV as the test cosmology.

4.2.2 Summed mass of neutrinos, M_ν

Here I examine how well the velocity dispersion counts can be used to constrain the summed mass of neutrinos. For this case I adopt a Planck-based cosmology, fixing

$h = 0.6726$, $\Omega_b = 0.0491$, $\Omega_{\rm cdm} = 0.2650$, $n_s = 0.9652$, and assume a flat universe (i.e., as I increase M_ν and Ω_ν, Ω_Λ is decreased to maintain $\Omega_{\rm tot} = 1$). By holding all parameters apart from M_ν and Ω_Λ fixed, I am essentially considering a case where I take the primary CMB cosmology to be a correct description of the Universe at early times and quantify how well adding measurements of the velocity dispersion counts constrains the summed mass of neutrinos.

I consider 151 different values of the summed neutrino mass, ranging from the minimum allowed value of 0.06 eV up to 1 eV. I adopt $M_\nu = 0.06$ eV as our test case.

In Fig. 4.4 I explore the constraining power of the three synthetic surveys described above. The error bars show the 1-σ confidence errors. A GAMA-like survey, when combined with primary CMB constraints, would be expected to constrain $M_\nu < 0.38$ eV. A WAVES-like survey will improve on this somewhat, while a DESI-like survey will tightly constrain the summed mass of neutrinos ($M_\nu < 0.12$ eV) when it is combined with primary CMB measurements. The potential constraints from a DESI-like experiment are interesting from a particle physics perspective, as they could potentially allow one to distinguish between the 'normal' and 'inverted' neutrino hierarchy scenarios (see Lesgourgues & Pastor 2006 for further discussion). However, I note that the forecasts are still fairly simplistic, in that I have held the other cosmological parameters fixed (although they are strongly constrained by the primary CMB) and I have not considered the effects of redshift errors, group selection, etc. On the other hand, I have also not used the full information available in the dataset (e.g., multiple redshifts and velocity dispersion thresholds), which would be expected to improve the precision of the constraints.

4.3 Comparing GAMA with BAHAMAS

Although simulations excel at forecasting constraints for future surveys, and in this way guide observational astronomy along productive research paths, they can not single-handedly constrain the cosmological parameters in the real Universe. To con-

strain the parameters in our Universe, simulations and observations must be used in tandem.

In this thesis, I will compare a volume limited, mass limited, sample of GAMA data with results from BAHAMAS, and need to know how well the group finder recovers groups in this simulation. There is a discussion in Robotham et al. (2011), about how well the group finder detects groups in the entire GAMA survey and the mock catalogs from the Millennium simulation. However, there are differences between the mocks used to calibrate the group finder and BAHAMAS. Therefore, it is necessary to conduct an investigation into the group finder's results on the BAHAMAS simulation.

In the following section, I test the group finder's ability to recover the groups in the simulation. For clarity, I will refer to Robotham's Friend of Friends group finding algorithm used in this analysis as RFOF. I will show several scaling relationships with velocity dispersion, richness, and "radius" as measured from the RFOF. These quantities will test the accuracy of the simulation to create realistic groups. First, however, I will describe how the light cones are constructed from the BAHAMAS simulation.

4.3.1 Light cones

To make like-with-like comparisons of the simulations to the observations, light cones must be constructed. In brief, if the observer is at z=0 (as assumed here), then light cones contain all of the matter and radiation within some solid angle (the survey area) back to some earlier time, z_{max}. In a flat Universe characterized by Euclidean geometry, light rays travel in straight lines in comoving coordinates. Making light cones from simulation outputs is therefore straightforward under these conditions.

Ian McCarthy created the light cones for this project. He stacked randomly rotated and translated simulation snapshots at differing redshifts along the line of sight. The maximum opening angle, theta, that a light cone can subtend depends on the size of the simulation box (400 Mpc/h in this case) and the maximum redshift one wishes the cone to extend to. He chose a maximum redshift of $z_{max} = 0.5$. Given the simulation

box size, this translates into an opening angle of 15 degrees. Therefore, each light cone has a FOV of 225 squared degrees, which is comparable to (slightly larger than) that of the GAMA survey. For each simulation volume (i.e., for each of the different cosmologies considered), 10 quasi-independent light cones are created by adopting randomized viewing angles through the simulation boxes (i.e., different random translations and rotations).

Robotham then subdivided each cone into three slices, each with 5 degrees in declination. This matches the GAMA survey geometry. He also imposes on the light cones a stellar mass cut of $10^{10}\mathrm{M}_{\odot}$, and a further redshift cut of $z < 0.2$, to match the GAMA volume-limited sample. Finally, Robotham runs each subdivided light cone through RFOF. This program detects the groups and calculates the richness, radius, and gapper velocity dispersion of the group.

4.3.2 Purity of BAHAMAS groups

One test of the effectiveness of the group finding algorithm is to compare how many groups it finds to the known number of groups in the simulations. The number of groups in the simulations can be determined accurately when the simulations are in original form, and have all three dimensions of position information available. When the simulations are converted to light cones, this grouping metadata is still available for comparison purposes. However, the RFOF does not know the original groupings, and has to disentangle the positions from redshift space distortions, just like in real observations. Therefore, assuming the simulation is a good model of the universe, the group finder should work equally well on GAMA as BAHAMAS.

To calculate the detection fraction, I have created a program that matches known central galaxies (BCGsim) to centrals in the simulated light cone as determined by RFOF (ITERCEN). For this task, I search for ITERCEN galaxies within one R500 of the true BCGsim. I also apply a redshift limit of ± 3000 km/s of the BCGsim redshift. If one or more ITERCEN galaxies fall within that search radius, I classify the group as detected. I only search for matches of groups with 5 or more members. This is for two reasons.

First, I will not be using N< 5 groups for my analysis due to the low accuracy of their velocity dispersion, and secondly, RFOF has not been optimized to search for groups below this limit.

In figure 4.5, the results of the detection fraction program show that detections increase steeply with velocity dispersion. Detection fractions range from 0.17 to 1.00. Lower velocity dispersion groups are much less likely to be detected, while large groups with $\sigma > 1000$ km/s are always detected in the light cone. In Robotham et al. (2011), 73 per cent of the mock groups are recovered. If I average the detection fractions above 300 km/s, the region of interest for my research, I find the mean detection fraction is 64 percent. Since the detection fraction is a steep function of velocity dispersion, it is difficult to confidently produce one value to compare with the value in the original paper.

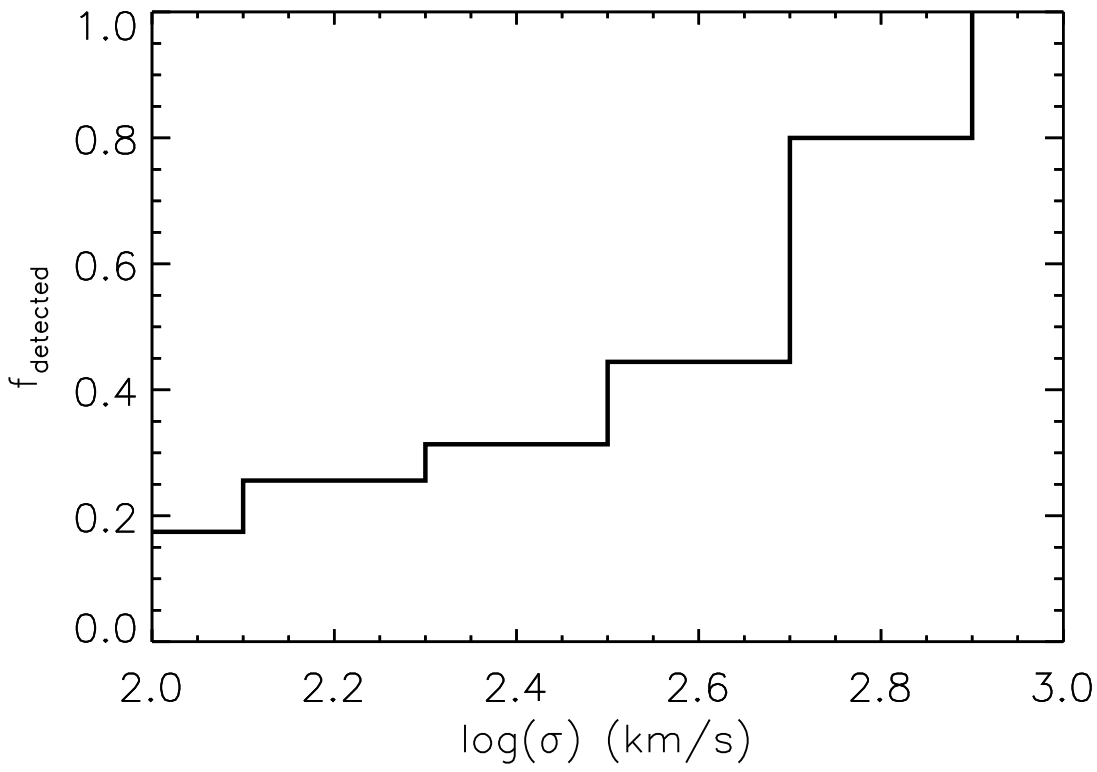

Figure 4.5: The fraction of BAHAMAS groups recovered by RFOF shown as a function of logged velocity dispersion. The detection fraction is a steep function of velocity dispersion, however, if averaged over the velocity dispersion range of interest for this work ($\sigma \gtrsim 300$ km/s), then the detection fraction is 64 per cent.

The low detection fraction is puzzling. One explanation, provided in the Robotham et al. paper, is that the group finder detects more high richness groups in the mock than it does in the GAMA survey. Another reason for the low detection fraction is the group finder is splitting larger groups into smaller ones. To check, I perform a quick test. For each galaxy in a RFOF group, I referenced the original simulation catalog and looked up its actual group number. In several cases, the RFOF group was composed of galaxies that were originally assigned to separate groups. In these cases, I calculated the statistical mode of the groups that the galaxies belong to, in order to choose the group I think RFOF algorithm was targeting.

For example, a RFOF group, alpha, is composed of 5 galaxies. I look up the original group assigned to each of those galaxies. Say, three of those galaxies are assigned to group A and two are assigned to group B. The mode is group A, and I look up group A's richness and it happens to be ten. Another RFOF group, beta, has a similar set up, where most galaxies belong to group A and a few do not. Now I have two RFOF groups assigned to group A, which has a true richness of ten. That is how the points are determined. At the time of writing, this test has only been performed on one light cone.

Figure 4.6 shows the result of crossmatching groups assigned to galaxies from the simulation with groupings from the algorithm. The x axis is the richness of the simulated group calculated within R200m. The y axis shows how many times the members of a FoF group have the mode of their originally assigned groupings equal to the group whose richness is plotted below. For figure 4.6, I plot the subset with $300 < \sigma(km/s) < 1000$ and N> 4 within the volume limited sample. At richnesses less than 10, the probability of a group being split into two is 46%. For richnesses greater than 10, it is highly probable that multiple FoF groups will be assigned to a single simulated group. Although more work is needed to extend this analysis to the whole sample, it is clear that splitting larger groups into smaller groups could contribute the low detection fraction at intermediate velocity dispersions. However, this cannot completely explain the phenomena in fig.4.5 because the highest σ bin is completely detected.

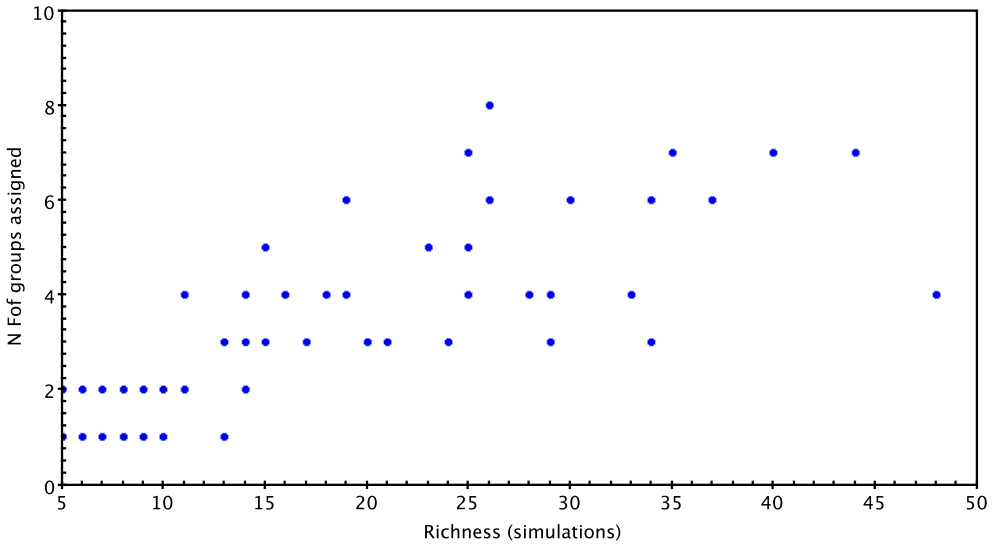

Figure 4.6: The number of FoF groups assigned to a single simulated group as a function of simulation group richness within a radius of R200m. There is a clear positive trend with richness, implying that large simulation groups are being split into smaller groups by the group finding algorithm.

4.3.3 Scaling Relations

Another approach to testing the compatibility between simulations and observations is to see if their mean properties are similar. To illustrate this, I show three different compatibility tests based on the velocity dispersion, richness and radius. All three of these quantities are products of the Robotham et al. group finding code. To ensure a similar selection of groups, both the simulated light cones, and the GAMA data have undergone group selection using the GAMA group finder. The velocity dispersion is calculated using the "gapper" method, described in Beers et al. (1990); Robotham et al. (2011) and chapter three of this thesis. The richness is the number of galaxies belonging to the group, according to the RFOF algorithm, and the radius is the quantity named "Rad50" in the RFOF catalog. It is the radius that contains 50% of the galaxies in the group. Please see chapter three for an in-depth discussion of the scaling relations. Here I present them as a means to qualitatively judge the compatibility of GAMA and BAHAMAS.

Velocity Dispersion - Richness relation

First, I present the velocity dispersion - richness relation.[1] The figure 4.7 shows the contours of the 14th and 86th percentiles of the distribution, which approximates one standard deviation in a normal distribution. I also show the median value. The colors represent several different cosmologies from the BAHAMAS simulation, and the black line shows the GAMA values. This looks like a very good match.

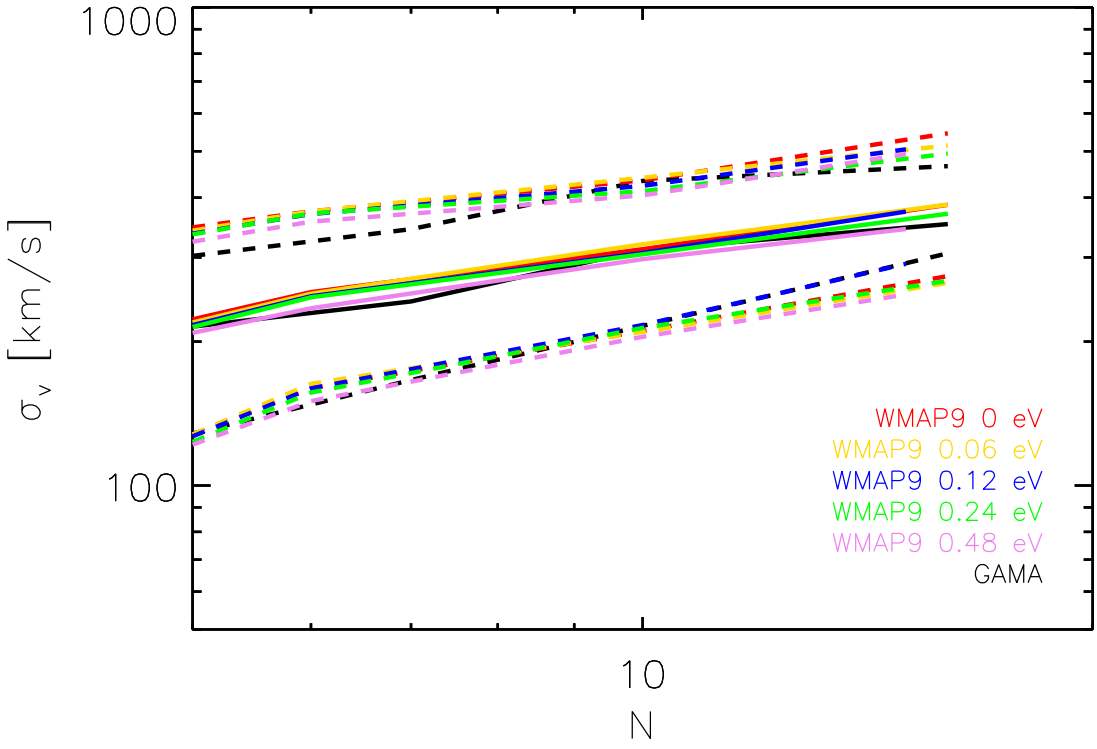

Figure 4.7: The mean velocity dispersion - richness relation for the volume-limited GAMA groups (black) and several different neutrino mass light cones from the BAHAMAS survey.

Richness - Radius relation

Next, I investigate the richness versus radius relation between GAMA and BAHAMAS. It is not as compatible as the velocity dispersion-richness relation. In figure 4.8, the lines represent the same surveys as in figure 4.7. However, in this plot the slope of the

[1] From this point on, the velocity dispersions from BAHAMAS are multiplied by the inverse square root of little h. This is necessary to correct an error that occurred when converting the BAHAMAS velocities from comoving space to physical.

median simulated groups is much steeper than the GAMA relation. Statistically, the median simulated values fall within the 1σ contours of the GAMA distribution, and that should be an acceptable match, but the discrepancy in slopes begs an explanation.

Surely, since velocity dispersion and radius are related through the gravitational potential, one would expect something to look awry with the velocity-richness plot as well. However this is not the case. Perhaps this is because the radius definition used in the FoF group finder is based on the assumption that the group is complete before calculating the radius of half the population? In their paper, Robotham et al. claim that at high richness, there was a discrepancy between number of systems. It could be that the number of systems is different because the radii are not the same, allowing for groups to be combined that shouldn't be.

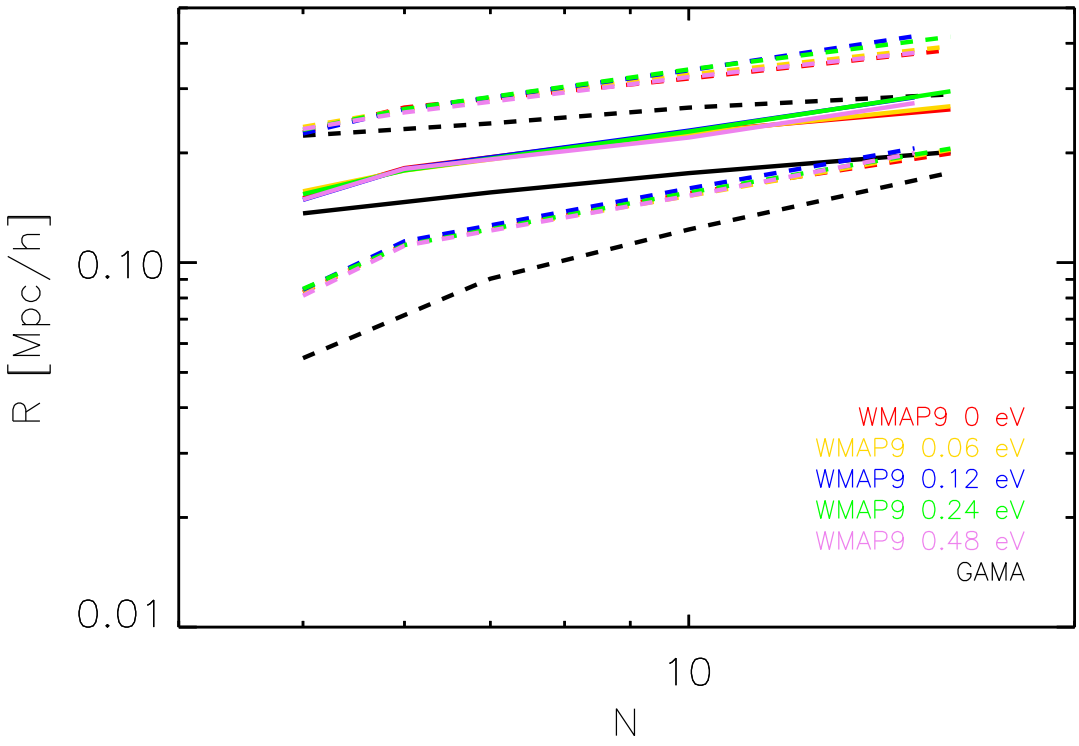

Figure 4.8: The mean radius - richness relation for the volume-limited GAMA groups (black) and several different neutrino mass light cones from the BAHAMAS simulation.

Velocity Dispersion - group radius

As a third and final scaling relation test, I examine the velocity dispersion-group radius distribution. Again, in figure 4.9 the colors of the simulations are the same as in figure 4.7 and the percentiles of GAMA are in black. Unlike the previous radius plot, the simulation and observations seem to be in very close agreement. If richness was affecting the distribution, as assumed above, then since velocity dispersion is proportional to richness, I would expect some discrepancy at high velocity dispersions, but there is none. From these plots it is clear that despite one puzzling, yet insignificant, deviation in the richness-radius plot, the simulations and observations are in good agreement.

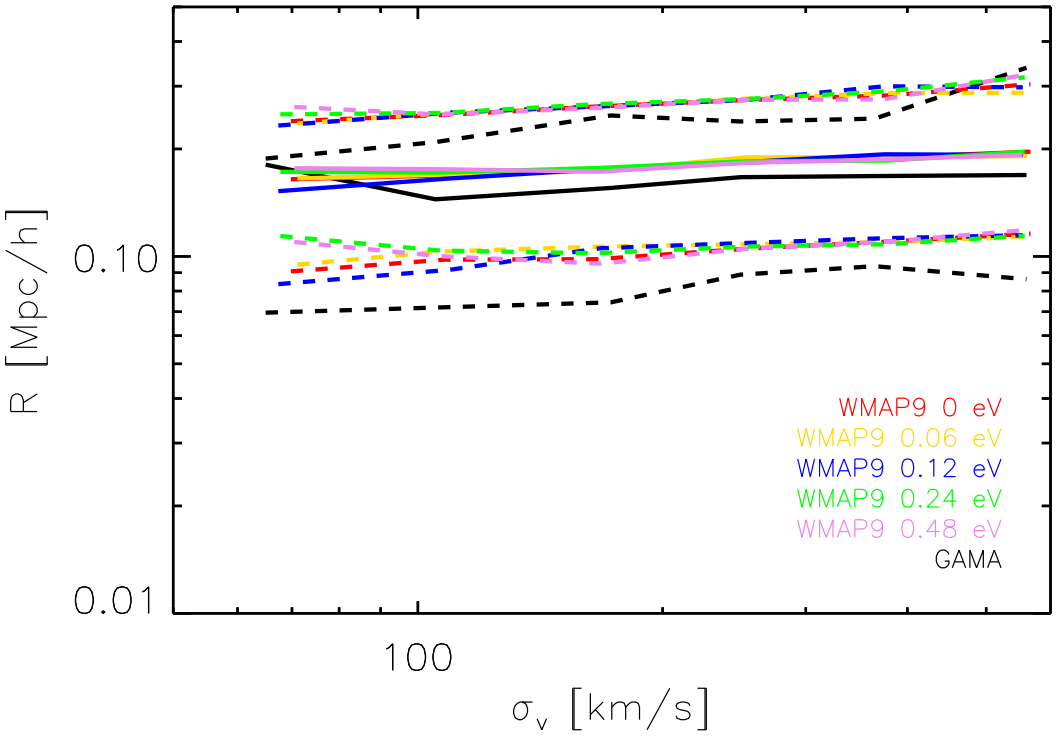

Figure 4.9: The mean velocity dispersion - group radius relation for the volume-limited GAMA groups (black) and several different neutrino mass light cones from the BAHAMAS survey.

The agreement between the simulations and observations in the scaling relations shows that the bulk physical properties of the real universe and simulated universe are similar. However, the low detection fraction indicates that number densities need to be treated cautiously. As I proceed to use the simulated and mock surveys to estimate cosmological parameters in Chapter 4, I will discuss further the corrections necessary to derive

reliable answers from the comparison.

4.4 Abundance of Groups in the GAMA Survey

Now that I have explored the effects of the group finding algorithm, I proceed to calculate the abundance of groups in the volume-limited GAMA sample. Since I have already shown that the constraining power depends on population size, I stack all three GAMA slices (G09, G12, and G15) to take advantage of the full 180 square degree survey area. Then, I count the groups with $5 < N < 20$ members that have velocity dispersions greater than 300 $\mathrm{km\,s^{-1}}$. The upper limit is informed by low number of groups at the $N > 20$ range, as well as the group finder's bias to detecting large groups in the mocks compared to the observational data. I find that GAMA has a number density of groups equal to $6.19 \times 10^{-05} \pm 4.24 \times 10^{-06} (\mathrm{Mpc/h})^{-3}$ at a mean redshift of 0.14.

Abundances are sensitive to the chosen mass or velocity dispersion thresholds. The GAMA data enables me to use a low threshold of 300 $\mathrm{km\,s^{-1}}$, which corresponds to $\mathrm{M}_{200m} \approx 10^{14} M_{\odot}$. As low mass groups are more prevalent than higher mass structures, this allows me to gain predictive power by increasing the sample size. Most abundance work, eg. Planck Collaboration XX et al. (2014), are unable to reach the sensitivity of GAMA and use massive clusters and higher thresholds. Therefore it is difficult to make a direct comparison with the literature.

To estimate the best-fit cosmological model, I compare the GAMA abundance to the BAHAMAS simulations. For this comparison, I use BAHAMAS light cones that have had groups identified by the GAMA group finder. For each cosmology there are ten light cones, of which A. Robotham has trimmed in declination to match the dimensions of a GAMA slice. One light cone becomes three 60 degree wide light cones. This aids in direct comparison to individual GAMA slices, but for this test, large sample size is required. So the slices and cones are stacked. Then, I limit the light cones to groups with $z < 0.2$ and $4 < \mathrm{N} < 20$. The original light cones and volume limited GAMA

sample have already been mass limited to M$> 10^{10}$M$_\odot$. Finally, I create figure 4.10 by counting the number of groups above 300 km s^{-1}.

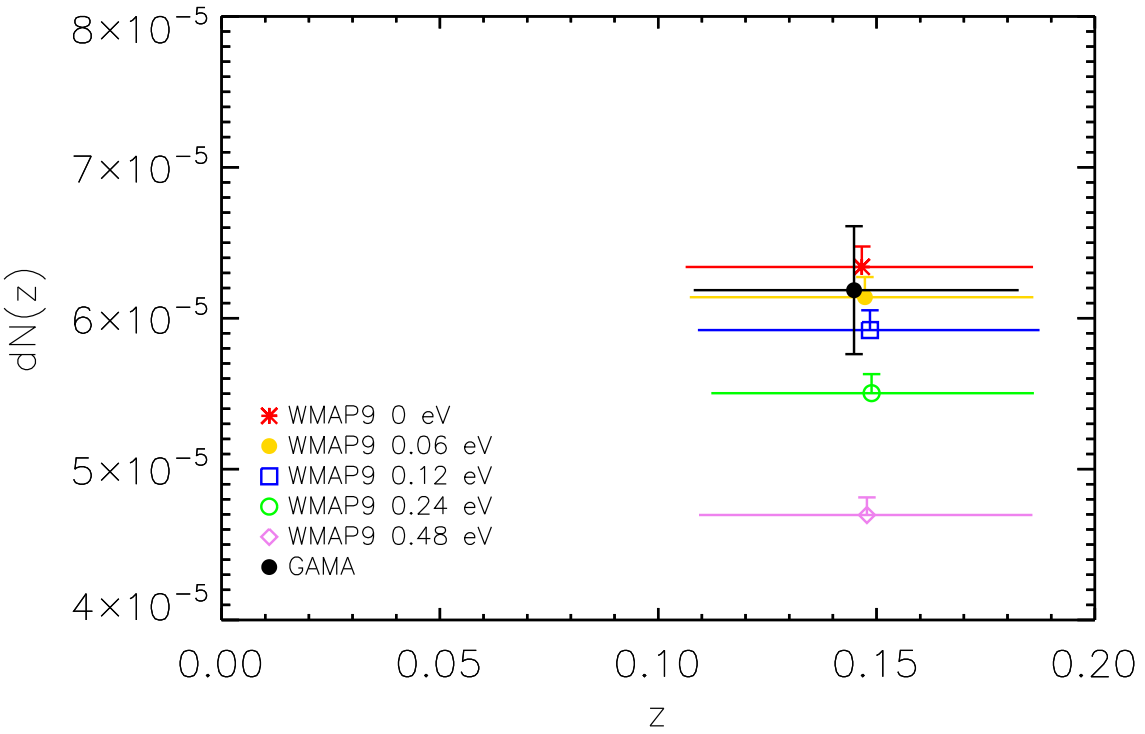

Figure 4.10: Number density of groups from the GAMA survey and number counts from the BAHAMAS light cones with, which have groups selected by the GAMA FoF, for comparison. The simulations shown here are based on a WMAP9 cosmology with neutrino masses of 0, 0.06, 0.12, 0.24, and 0.48 eV. The GAMA point between the WMAP9 cosmologies with 0 and 0.24 eV summed neutrino masses. All abundances are shown with Poisson 1σ vertical error bars and horizontal error bars represent the 14 and 86 percentiles of the redshift distribution. Each abundance is placed at the mean of the median group redshifts.

Figure 4.10 shows that the GAMA abundances are within the range of the WMAP cosmologies from BAHAMAS, and that the appropriate summed neutrino mass lies between 0 and less than 0.24 eV. The upper GAMA error bar lies above the neutrinoless WMAP9 abundance. However, considering the trend in fig. 3.3, this would imply a Planck cosmology with neutrino masses greater than 0.24 eV, which is ruled out by Planck CMB ΛCDM models, that place the upper limit on summed neutrino mass at 0.59 eV (Hannestad, 2016; Planck Collaboration et al., 2016). This upper limit is further constrained to 0.23 eV when large scale structure is added (Planck Collaboration et al., 2016). Therefore, the GAMA data agree with models of WMAP9 cosmology

with $0\mathrm{eV} < \sum \mathrm{M}_\nu < 0.24\mathrm{eV}$. A chi-squared test using the method described in section 4.1 will have to be conducted to officially exclude Planck cosmologies and obtain a statistically verified constraint.

4.5 Summary

Constraining cosmological parameters provides insight into how the universe formed. In this chapter, I present methods to constrain cosmological parameters with velocity dispersion based group abundances. First, I show that a simple model can be constructed from the mean mass-velocity dispersion relation, and its scatter that will accurately reproduce velocity dispersion functions and number counts for a variety of cosmologies. I exploit this simple model to create a grid of abundances, each with a different set of underlying cosmological parameters. I make multiple grids to account for differences in surveys. Then, I calculate the minimum chi-squared statistic to find the 1σ confidence interval for several mock surveys.

I also attempt to constrain cosmological parameters using the GAMA survey by comparing the GAMA group abundance to several simulated abundances from BAHAMAS. First, I investigate the detection capabilities of the group finder using BAHAMAS. Although, the detection fraction was a steep function of richness, the mean detection fraction, 64%, is close to the detection fraction stated in Robotham et al. (2011). More work on the compatibility between GAMA and BAHAMAS will improve the accuracy of the constraints derived from this comparison. Finally, I show the abundance of GAMA groups at a median redshift of 0.15. The GAMA point falls near the WMAP9 cosmologies with neutrino masses between $0\mathrm{eV} < \sum \mathrm{M}_\nu < 0.24\mathrm{eV}$.

Chapter 5

Part One Conclusions and Future Work

In the first part of this thesis, I constrain cosmological parameters using a non standard technique: velocity dispersion based group number counts.

In chapter 2, I describe the simulation and survey that I use in this research. The BAHAMAS simulation (McCarthy et al., 2016) is a new hydrodynamic simulation based on the insights gained from the OWLs and CosmoOWLs simulations(Le Brun et al., 2014; McCarthy et al., 2014). The GAMA survey is a spectroscopic redshift survey that has been designed for uniform spatial completeness that makes it ideal for characterizing galaxy groups. There are 652 groups in the volume limited and richness limited sample.

In chapter 3, I explore properties of groups and how they evolve over time using several well known scaling relations. The temperature - velocity dispersion relation does not scale self similarly, but the velocity dispersion - mass relation does. The scatter around the velocity dispersion - mass relation is large, particularly at masses less than M200m$< 10^{13}$ M$_{\odot}$. I have investigated the sources of this scatter and created a parametric model to describe it. The powerlaw coefficients for several 2D and 3D volumes are presented in Table 3.1.

In chapter 4, I create a method for constraining cosmological parameters using velocity dispersions of groups. From the number counts plot in chapter 3, it is clear that velocity dispersions of groups can be used in this context to discriminate between different cosmological models, including non standard models that include massive neutrinos. To constrain cosmological parameters using BAHAMAS, I follow three steps: 1. Generate a power spectrum for a chosen cosmology using CAMB, 2. Convert the power spectrum into a mass function using the Tinker mass function (Tinker et al., 2008), and 3. Use the Mass-velocity dispersion power law and scatter to get the velocity dispersion function for that cosmology. Then I forecast the constraining power of current and future surveys. These predictions show a steep degeneracy on the $\sigma_8 - \Omega_m$ plane. The precision of the constraint is a strong function of number of groups, and therefore survey area. I predict that the constraint on summed neutrino mass will be precise enough using the DESI bright galaxy survey to break the degeneracy between inverted and normal neutrino hierarchy.

In the final part of chapter 4, I begin to compare GAMA data and the BAHAMAS simulation. First, I check that the BAHAMAS simulation has accurately reproduced some important scaling relations from the GAMA survey. I also investigate the group finding algorithm's ability to recover groups by testing it on BAHAMAS. After confirming the compatibility of the GAMA and BAHAMAS simulations, I compare the abundance of GAMA groups at z ≈ 0.15 to BAHAMAS. I find that the GAMA point lies within the bounds of neutrino masses currently set by other cosmology based estimates.

There are two main future work projects for this section. First, I will redo the analysis involving scaling relations so that the correction factor $(h)^{-0.5}$ is applied to the velocities from the BAHAMAS simulation. This is to correct for a bug in the black box that converts velocities from comoving to physical units. Due to time constraints, I was not able to complete this before submission. However, with respect to the scaling relations, this will only produce a simple offset.

Secondly, I will finish the GAMA cosmological constraint project. As mentioned in the text, the correction to the velocity dispersion has been applied in section 4.3 and those that follow it. Additionally, there is some discrepancy in the radii and richnesses of

GAMA and BAHAMAS groups, as seen in the scaling relation comparison in chapter 4. I will conduct a full investigation into the group finding algorithm to understand why the detection fraction is a strong function of richness, and why the average radii of GAMA and BAHAMAS groups do not coincide. Following a thorough characterization of the effects of RFOF on group selection properties, I will correct incompleteness. Then, the number count grids will be calculated using the Tinker mass function with a correction to account for the effects of baryons (Velliscig et al., 2014). Finally, I will follow the method described in section 4.2 to calculate the constraints on σ_8, Ω_m, and M_ν.

Part II

Effect of Active Galactic Nuclei Feedback on Host Galaxy Morphology

Chapter 6

Introduction

6.1 AGN and Galaxy Evolution

6.1.1 The Color Bimodality

It has been demonstrated that galaxies in the local Universe can be grouped into two color bins, red and blue (Baldry et al., 2004; Strateva et al., 2005). Blue galaxies are undergoing star formation or have had star formation recently quenched, and red galaxies have stopped forming stars. Since all galaxies originally were blue, star-forming galaxies, the color bimodality in the recent universe indicates that at some point, something must have happened to some of the galaxies to make them stop forming stars permanently.

The questions remain of when and how this bimodality began. There have been several attempts to constrain the point at which red galaxies first formed. Work by Cirasuolo et al. (2007), shows the red sequence being populated from a redshift of 2 to 0.6. Brammer et al. (2009) traced the existence of a red sequence back to a redshift of 2.2, see figure 6.1. This places an upper limit on the formation of the red sequence. Simpson et al. (2012) show that the FRII population peaks at $z \sim 2$. A high amount of energetic radio activity may indicate that a dramatic change in the galaxy population is

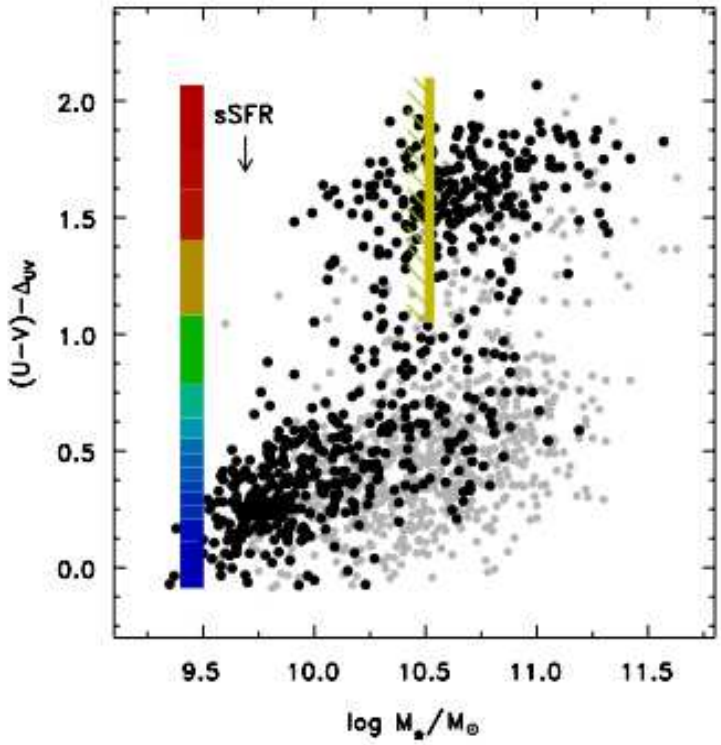

Figure 6.1: This is the color bimodality near redshift = 2 (Brammer et al., 2009). There are two clearly defined populations. The red sequence consists of the objects between U-V colors of approximately 1.3 and 2, and the blue cloud consists of the objects below a U-V color of 1.3.

occurring at this epoch. More observations are needed beyond a redshift of 2 to view the Universe at earlier times to uncover the origin of the red sequence.

Initially, theoretical models of galaxy evolution were unhelpful in understanding the color bimodality. They typically produced large massive, bright galaxies (Somerville & Primack, 1999; Cole et al., 2000), emphasizing the fact that the mechanism for star formation quenching was unknown. Later, modelers obtained successful results by artificially switching off and on the cooling in massive halos in order to curb the growth of massive galaxies (Kauffmann et al., 1999), but it was unclear what could physically control the halo's on/off switch in the galaxy. Finally, recent models (Croton et al., 2006; Bower et al., 2006; Cattaneo et al., 2006), improved the agreement with observation by suggesting that active galactic nuclei feedback could be the physical analogue to the switch in the simulation. The most recent models (Booth & Schaye, 2009; Bower et al., 2012) use a combination of stellar and AGN feedback to control

star formation, but the specific contribution of these various feedback modes needs to be confirmed by observation.

It has been observed that red galaxies dominate the high mass regime of the galactic mass distribution. The most massive galaxies are also predominantly elliptical. Additionally, the strong correlation that is observed between masses of the black hole and the bulge, (Ferrarese & Merritt, 2000; Gebhardt et al., 2000) suggest that quenched massive elliptical galaxies host some of the largest black holes in the universe.

Silk & Rees (1998) suggested that AGN feedback could affect galaxy evolution by ejecting gas, if its energy is coupled with the baryonic matter in the galaxy. Active galactic nuclei (AGN) feedback is the process where energy is released back into the galaxy when a galaxy's central supermassive black hole is accreting matter. It limits the further accretion of matter by the black hole. AGN feedback has been observed to produce massive radio jets and lobes that create X-ray bubbles and cavities (Carilli et al., 1994; McNamara et al., 2000; Bîrzan et al., 2004). This is evidence that AGN feedback does input energy back into the galaxy, and could be an agent of star formation quenching. The theory of "Eddington fueled feedback events" (Rawlings 2003), dynamical models, and observations all provide strong evidence that AGN feedback is responsible for shaping the bulge and depositing enough energy into the galaxy to balance the effects of halo cooling and create the color bimodality.

6.1.2 Galaxy Growth

Quenching star formation is not the only effect that AGN can have on their host galaxy. Fan et al (2008) propose that rapid mass loss from high power AGN winds can cause a galaxy to dramatically expand in radius. If the mass loss occurs faster than a dynamical time then the galaxy finds itself in a energetically unbalanced state with velocity dispersions of the stars (kinetic energy) too large for the new (lower) mass (potential energy). The orbits of the stars then expand because the gravitational potential is less than before. In the Fan et al paper, this growth mechanism was used to explain the evolution of 'red nugget' galaxies - very compact, quiescent galaxies found only at high

redshift. This effect was originally theorized for globular clusters and was scaled up to make predictions for galaxies. One important difference between globular clusters and elliptical galaxies, is the latter has a dominant dark matter halo that suppresses mass loss. This condition was accounted for in their predictions. Despite the damping effects of the dark matter halo, for galaxies with pre-ejection masses of greater than 2×10^{10} M_*, the authors predict that the radius could increase to a maximum of twice its original size.

The predicted size decrease is shown in figure 6.2. This is figure 1 in the original Fan et al. paper. This complex figure shows the effective radius - stellar mass relation for, GMASS data (filled symbols) and numerical models (open symbols). Since the radial growth is caused by AGN powered mass loss, this effect will be seen most clearly in the most massive galaxies, that on average host more massive black holes (Ferrarese & Merritt, 2000; Gebhardt et al., 2000). Therefore Fan et al. direct the reader to observe the evolution in galaxies with stellar masses greater than 2e10 Mstar. For the most massive galaxies, the radius evolves from 0.5 kpc to 1 kpc in the time between the last AGN mass loss episode and the present day. The authors calculate the timescale of this growth to be approximately 2 Gigayears, scaling up an estimate from globular clusters of 40 dynamical times. Assuming the last AGN outburst was at the peak of AGN activity, redshift 2, then galaxies should reach virialization (denoted by the open stars in the figure) at around a redshift of 0.8.

6.2 Radio Galaxies

Radio galaxies are a class of AGN that are known for the powerful jets that are emitted from the centre of the galaxy. The most powerful jets extend up to megaparsecs outside their host galaxy. The powerful AGN that drive these jets could produce the rapid mass loss described in Fan et al. (2008). In this section, I will describe the various types of radio galaxies and explain why one particular type, High Energy Radio Galaxies (HERGs), are relevant for my study of galaxy size evolution.

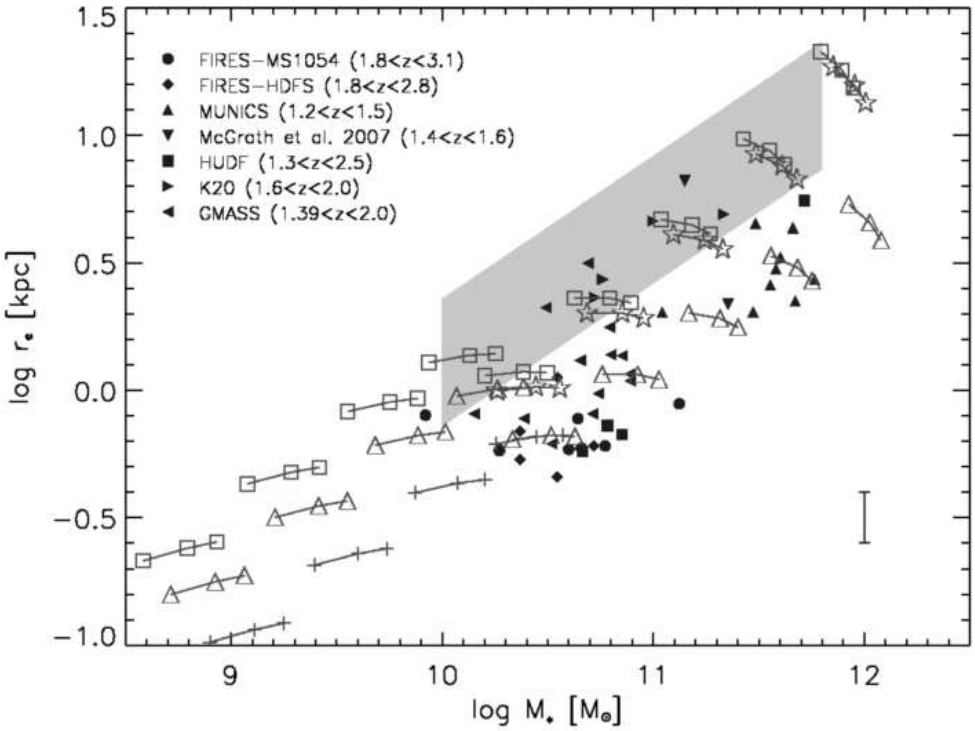

Figure 6.2: This figure is from Fan et al 2008. For galaxies greater than 2×10^{10} M star, it shows the effective radius as a function of stellar mass galaxies in three different stages of evolution. The solid points are observational data from various surveys that are explained on the plot. The open symbols are predictions from a numerical simulation. The triangle symbols denote galaxies at the end of the bright quasar phase. The stars represent galaxies that have reached a new virial equilibrium after the quasar phase, and the square symbols show the radius of these galaxies at the present. This figure also shows evolution for galaxies less than 2×10^{10} M star. The crosses are galaxies at the end of baryon collapse, the triangles are after 0.5 Gyr, and squares show the current size. The gray area shows the $\pm1\sigma$ local size-Mstar relation (Shen et al 2003).

6.2.1 Types of Radio Galaxies

There are two main classes of radio galaxies. Those with strong, powerful jets, are called Fanaroff and Riley Class Two (FRII) sources, and galaxies with weaker jets, FRI (Fanaroff & Riley, 1974). There is a similar division based on spectral properties. Hine & Longair (1979), found that some radio galaxies had strong emission lines, and others had weak lines. These are named Class A and Class B, respectively. Class A roughly corresponds to the FRII type, and Class B roughly corresponds to the FRI type. However, unlike the Hine and Longair classification, the morphological (FR) classification system is not directly indicative of the processes in the central engine of the AGN. The spectral properties identified by Hine and Longair suggest that there are fundamentally different processes at work in the central engine of Class A and Class B sources. The presence of strong emission lines indicate that cold-mode accretion via an accretion disk is present. Likewise, the absence of lines in Class B types suggest that the black hole is undergoing hot-mode accretion, that is accretion in a less radiatively efficient way, perhaps in a spherical, Bondi-Hoyle manner. Another distinction is based on radio luminosity. Low Energy Radio Galaxies (LERGs) are radio galaxies with energies lower than $L_{rad} = 10^{25} W Hz^{-1}$, and the radio emission could be produced by stars to low powered AGN jets. High Energy Radio Galaxies (HERGs) definitely correspond to very strong AGN activity.

Low-luminosity Radio-loud AGN (a.k.a."hot-mode" AGN), or LERGs, which accrete matter in all directions (Bondi and Hoyle 1944) rather than from an accretion disk (Silk & Rees, 1998), (Best & Heckman, 2012), are the best candidate to deposit enough heat into the halo via feedback that the halo will not be able to cool and form stars (Best et al., 2005, 2006). I will investigate if this class of AGN could be responsible for the end of star formation in massive galaxies, and create an empirical evolutionary history of AGN to $z \sim 3$.

6.2.2 Duty Cycle Hypothesis

The Duty Cycle Hypothesis (DCH) (Best et al., 2005, 2006) applies the proposed effect of hot-mode AGN feedback to galaxy evolution. The hypothesis proposes that over long time scales, the energy deposited into the galaxy from the hot-mode AGN balances cooling from the halo, which, if left unbalanced, could return the galaxy to conditions where star formation is possible. If hot-mode feedback balances halo cooling then star formation would be quenched indefinitely.

Figure 6.3 describes how a galaxy moves onto the red sequence and how the duty cycle maintains an environment where star formation cannot occur. In the first panel, there is a blue, star forming galaxy with an active AGN. The AGN feedback is apparent from the massive jets that extend outside of the galaxy. According to the DCH these jets can drive gas out of the galaxy, thus stopping star formation and the fueling of the AGN. The second panel shows that after star formation has been quenched, some time passes while the massive, blue stars are extinguished. When this occurs, the galaxy is left with less massive stars that emit in longer wavelengths, and it appears golden or red like the galaxy M87, pictured in the chart.

Focusing on the rightmost panel in figure 6.3, now that the galaxy has arrived on the red sequence, the duty cycle begins. Gas ejected from the central part of the galaxy returns and fuels the AGN. This returning gas could also condense and form stars, but the AGN feedback, which has now returned with the fueling of the AGN, prevents this by heating, in the form of mechanical energy, the intergalactic medium. The extra energy in the system, prevents the formation of stars. Once the gas supply is exhausted, the process ceases until more gas returns to the system.

Figure 6.4 shows observational evidence for the duty cycle hypothesis. It shows the X-ray luminosity and the B band luminosity of elliptical galaxies. The solid line shows the modeled X-ray emission from the hot haloes of the galaxies (Best et al., 2006). The good fit of the observational data to the model is evidence that the heating and cooling are balanced by AGN feedback in elliptical galaxies.

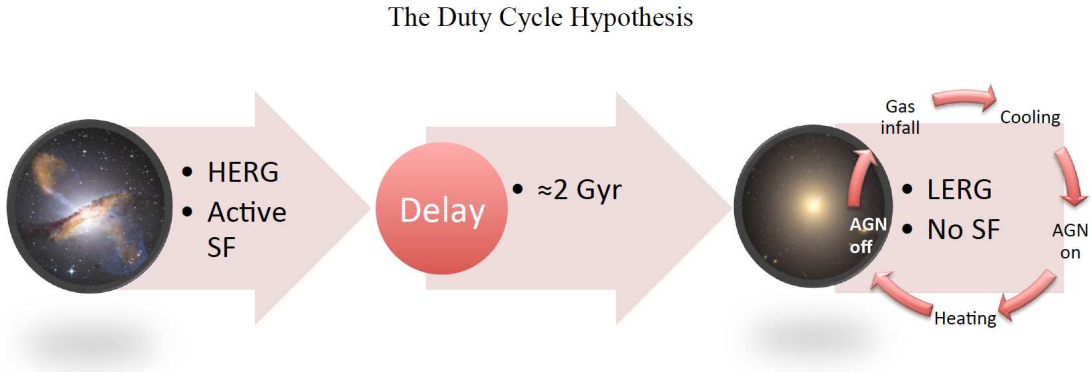

Figure 6.3: This flow chart shows the process of the duty cycle hypothesis. A full explanation is included in the text.

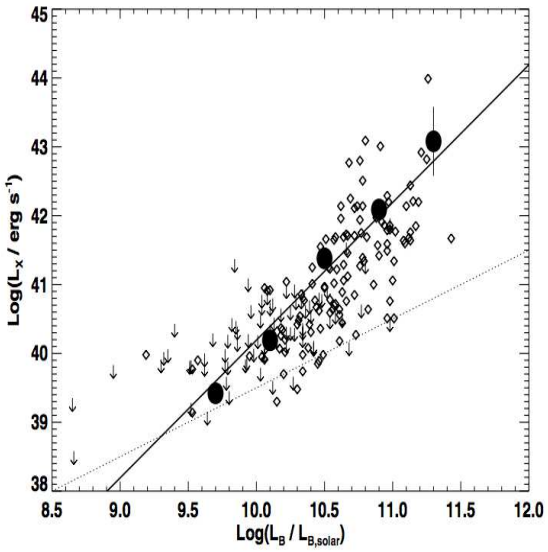

Figure 6.4: This plot from Best et al. (2006) shows the observed luminosities in the X-ray and B band (represented by the small points), and the median of the observed luminosities (the large points) fit nicely along the solid line that is a model of a galaxy that has the heating and cooling balanced by AGN feedback. This is strong evidence for the duty cycle hypothesis.

The Duty Cycle part of the hypothesis comes from the idea that initially, the cold gas in the galaxy would be removed, perhaps by the AGN emitting a powerful FRII type jet. Then star formation would cease until some of the gas found its way back into the galaxy. As the gas returns to the galaxy, some will find its way back to the central supermassive black hole. Then AGN activity will resume, however, this time, since the central region is less dense, the feedback will be less powerful. Over several iterations of gas expulsion, the feedback will be hot-mode, and only as powerful as the halo cooling which drove the gas back to the central engine, thus balancing the cooling, and quenching star formation.

In 1996, Cowie et al. coined the term "downsizing" to describe the observational result that massive galaxies stopped forming before less massive galaxies (Cowie et al., 1996). If the duty cycle hypothesis is true, then it could partially explain the apparent downsizing in the universe.

6.2.3 Source Counts

Figure 6.5 shows the expected source counts for different objects. The FRII objects have a steep decline in number density by S= 1milliJansky. One Jansky has units of $10^{-26} W m^{-2} \mathrm{Hz}^{-2}$. The FRI objects, which are in some cases similar to the low luminosity AGN involved in the DCH, continue to be well represented out to microJansky regime and beyond. The actual turn off of in number density for FRI sources is unknown due to lack of data at the microJansky level. My work will increase the sample size of these objects, provide insight into their evolution, and help refine the shape of the number density function of FRI sources.

6.3 The Square Kilometre Array

One future application of the proposed work involves the Square Kilometre Array (SKA), which will be built in South Africa and Australia. The Square Kilometre Array

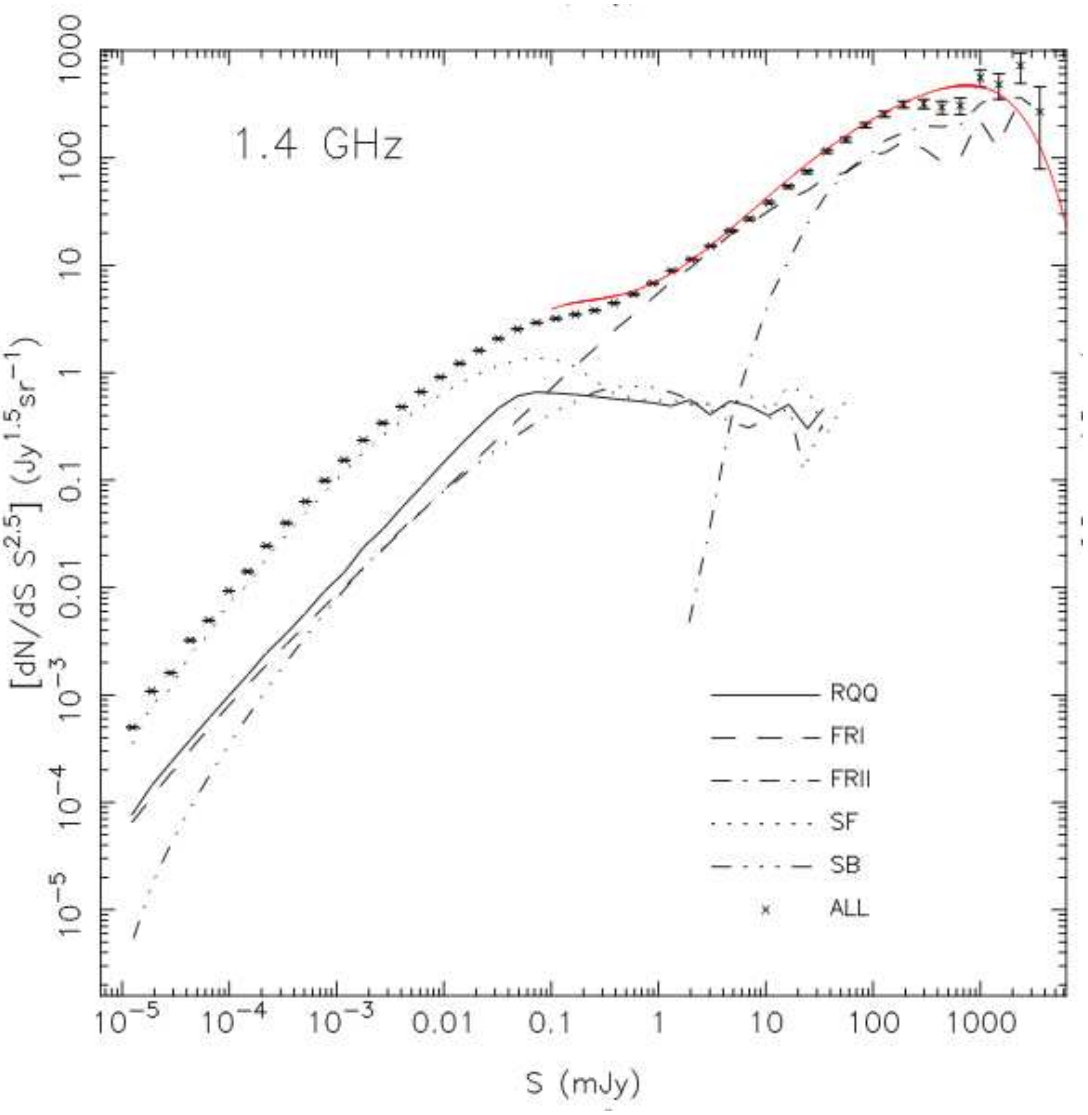

Figure 6.5: Using semi-empirical models, this plot from Wilman et al. (2008) shows the expected source counts for many types of radio emitting objects. These predictions will inform observations on the Square Kilometre Array.

is a new radio telescope array that will be able to trace hydrogen emission from the first stars and galaxies (Carilli & Rawlings, 2004). The SKA will be ~ 2 orders of magnitude deeper than the VLA for the same integration time (Norris et al., 2013). This will finally allow for the detailed analysis of low luminosity and radio quiet populations at higher redshift.

Galaxy evolution is one of the telescope's main science objectives, and the data from this telescope will provide the most complete observational history of the evolution of galaxies. It is important for us to understand the mechanisms behind the growth of galaxies in order to use this new facility to its fullest ability. The predictions from the proposed work can be tested when the SKA goes online in the mid 2020's.

6.3.1 Pathfinders

There are other telescopes that will act as pathfinders to SKA that will be online in the near future. The Low Frequency Array (LOFAR) is the newest pathfinder to come online. It will survey the radio sky of the Northern hemisphere in unprecedented detail, and a follow up project on the William Herschel Telescope's WEAVE (first light 2016) will provide optical spectroscopy. Using simulations of the radio sky (Wilman et al., 2008), it is predicted that WEAVE will be able follow up bright radio sources at high redshift due its large field of view and high survey speed (Trager & the Science Teams, 2012). These objects will help trace galactic evolution in the early universe, and test our theories about source counts and properties of hot-mode AGN at these epochs.

6.4 Comparing the Morphologies of LERGs and ellipticals

Using the duty cycle hypothesis, I can test the theory of radius growth due to rapid mass loss from AGN winds. The DCH says HERGs turn into LERGs after a large expulsion of gas (AGN fuel) from the galaxy. HERGs host the quasars that could

potentially cause the rapid mass loss described in the radius growth theory (Fan et al., 2008). Therefore, the presence of a LERG at low redshift indicates that a HERG phase happened at earlier times, and now some of that expelled gas has returned to the center of the galaxy, refueling the AGN, but at a lower rate. If this link holds I can trace the size evolution due to rapid mass loss by looking at LERGs between the last AGN outburst, around redshift 2, and in the present epoch. According to the evolution theories discussed above, I expect current LERG hosts to be red, and larger than ellipticals that never experienced a HERG phase.

Throughout the AGN investigation we adopt a flat ΛCDM cosmology with $H_0 = 70\,\mathrm{km\,s^{-1}\,Mpc^{-1}}$ and $\Omega_\Lambda \equiv 1 - \Omega_\mathrm{m} = 0.7$. All magnitudes are on the AB system.

Chapter 7

The Data

K-band selected, multi-wavelength catalogs in the ULTRAVISTA COSMOS (Muzzin et al., 2013), and UKIDSS UDS (Arumugam et al., in prep) fields are used in this research. I also use morphological information derived from HST/CANDELS data in the F814W (Griffith et al., 2012), F160W and F125W bands (van der Wel et al., 2012). Radio data for COSMOS and UDS are from the catalogs of Schinnerer et al. (2010), and Simpson et al. (2012), respectively.

The Muzzin et al., Ks-selected catalogue, includes 30 bands of photometry including data from GALEX, Subaru, CFHT, UltraVISTA, and Spitzer. The Muzzin et al. catalog has a 90 per cent completeness at Ks_{AB}=23.4. In addition to multi-wavelength data, the COSMOS field has a spectroscopic subset of data, zCOSMOS, which has been matched to the rest of the data (Lilly et al., 2009). We use radio data from the vlaCOSMOS deep survey (Schinnerer et al., 2010).

The ULTRAVISTA Spitzer data have a considerably larger point spread function (PSF) than the ground based data. The Muzzin et al. catalogue uses a technique of cleaning the Spitzer data using the Ks band as a high resolution template. This extra step of cleaning the Spitzer data improves the quality of the image, and by removing assumption that all the objects have the same Ks – IRAC magnitude, allows the flux of each object in the Spitzer data to be measured more accurately. After the flux has been calculated from the cleaned image, an aperture correction factor, which is a ratio of fluxes

in different apertures, is applied to get the final flux.

The UDS, data release 8, covers 0.8 degrees^2 and has 5-σ completeness to 24.6 AB magnitude in the K band (Lawrence et al., 2007). The UDS DR8 has data in the J,H, and K bands and other wavelengths (B, V,R_c,i',and z') are described in the Subaru-XMM Newton Deep Field optical catalog paper (Furusawa et al., 2008). Catalog matching was performed by Chris Simpson and documentation cannot be found. 1.4 GHz radio data in the UDS field is presented in Simpson et al. (2012).

The 24 micron data was included in the Muzzin et al. (2013) catalog, and the UDS 24 micron fluxes were measured on the 24 micron image at the K band source position using an IRAF task to fit a Gaussian near the specified position and calculate the flux under the curve. During the fitting, if the Gaussian position tries to move by$>$2.2 arcsec, then the peak position is fixed at the input position.Due to the large point spread function of the 24 micron image, occasionally the gaussian peak value in the 24 micron image was more than 2.2 arc seconds away from the specified K band position. In these instances, an interactive IRAF task was used to remove noise in the target area to ensure only the flux from the intended source was measured. Then upper limits for the UDS 24 micron sources, where the flux was less than the signal to noise, were calculated by taking three times the noise.

The van der Wel et al. (2012) catalogue of GALFIT structural parameters for a subset of objects in the UltraVISTA/COSMOS and UDS fields is used to determine a radial separation between stars, quasars and galaxies. The structural parameters of the van der Wel catalogue are determined from HST/CANDELS data in the F125W and F160W filters, which correspond roughly to the J and H bands, respectively (Grogin et al., 2011; Koekemoer et al., 2011). The Griffith et al. (2012) catalog of structural parameters for the COSMOS field, using the ACS F814W band was used along with the F160W data for the radius analysis in section 8.3.1. When an object was found in both the F814W and F160W catalogs, the F814W radius measurement was used.

Table 7.1 shows the number of galaxies at different stages of the analysis. After identifying the galaxies, I combine the UDS and ULTRAVISTA catalogs to obtain a sample

Table 7.1: The number of galaxies in the sample after matching additional catalogs.

Total combined galaxy sample	364,891
Galaxies with spectroscopic z	12,041
Galaxies with radii information	162,062
Galaxies with radio flux	1,711
LERGs	151

size of 364,891 galaxies. 12,041 galaxies have spectroscopic redshifts. There are 162,062 galaxies with either F814W or F160W radius information, and 1711 galaxies with radio counterparts. See chapter 8.2.2 for more information about how the radio catalog was matched to the photometry. Finally, I identify 151 radio galaxies as LERGs using the q24 method discussed in chapter 8.2.3.

Chapter 8

Analysis and Results

Galaxy evolution theories state that AGN feedback can quench star formation (Best et al., 2014) and dramatically increase the radius of AGN host galaxies (Fan et al., 2008). The aim of this research is to examine the effects of AGN feedback on the radius and star formation and test these galaxy evolution theories.

This chapter describes the methods and techniques used to turn the fluxes in the catalogs into useful quantities for the radius comparison which will test the role of AGN heating in elliptical galaxies. Photometric redshifts and masses are calculated from the photometry. Then stars and quasars must be removed from the sample, and the galaxies are carefully matched with radio sources. Finally, the radio emission must be classified as radio-loud or radio-quiet before radius comparisons between radio-loud AGN and quiescent ellipticals can be made. Then, using these data products, I present the results of a comparison of AGN host galaxy radii with a matched population of non-active ellipticals.

8.1 Calculating redshift and mass

As I am using both the UDS and ULTRAVISTA catalogs, I will need to calculate zero point offsets to ensure that the zero points of the bandpasses used in the two surveys

are calibrated consistently. Slight differences occur between filters. Then, I need to calculate a redshift of each object, and finally estimate its mass. In the following section, I describe my methods to calculate these fundamental quantities.

8.1.1 Photometric redshifts

Both COSMOS and UDS have subsets of data with optical spectroscopy, however these spectra do not cover the redshift range required, and so I take advantage of the excellent multi wavelength coverage to calculate photometric redshifts. I used the photometric redshift code, EAZY (Brammer et al., 2008), along with the Charlot and Bruzual 07 template set, to calculate 15 band photometric redshifts for the ULTRAVISTA dataset, and 11 band photometric redshifts for the UDS data. Spitzer/IRAC channels 3 and 4, and the g and Y band were not available for the UDS catalog. As the EAZY code uses template fitting, the accuracy of the fit and of the redshift improve when the user provides more band passes to characterize the spectral energy distribution (SED).

I fine tune the redshifts using the subset of data with optical spectroscopy, by calculating the small zero point offsets which exist between the different bandpasses. This calculation is done by holding the K band fixed, and running a simulated annealing code on the matrix of filters until it minimizes the EAZY parameter σ_{NMAD} (Brammer et al., 2008), which is the normalized median absolute standard deviation between the photometric and spectroscopic redshifts. Table 8.1 shows the offsets in magnitude applied to each filter when the redshifts were calculated.

8.1.2 Masses

The masses (see Figure 8.1) were calculated by Chris Simpson, and are derived using the SED fitting method of Simpson et al. (2013). This method fits linear combinations of a large set of simple stellar population templates (Charlot and Bruzual 2007) to the source at the spectroscopic redshift. If spectroscopic redshift is not available, the photometric redshift is used.

Table 8.1: Photometric magnitude zero point offsets for ULTRAVISTA COSMOS and UKIDSS UDS.

Filter	UltraVISTA	UDS
u	-0.004	-0.051
B	0.010	0.005
g	-0.019	–
V	-0.006	-0.026
r	0.008	0.114
i	0.007	-0.015
z	0.029	-0.028
Y	-0.008	–
J	0.018	-0.028
H	-0.007	0.011
ch1	-0.009	0.021
ch2	0.007	0.002
ch3	0.011	–
ch4	-0.009	–

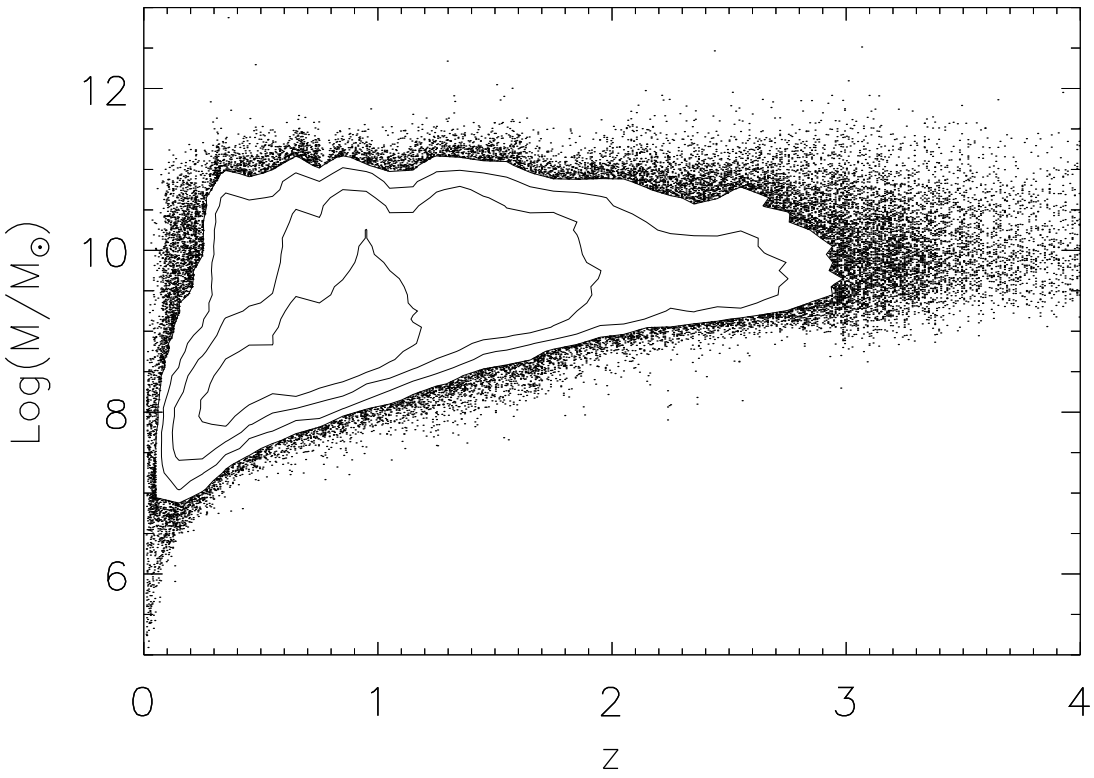

Figure 8.1: Masses of all objects in the UltraVista and UDS fields out to a redshift of 4. The contours have bin sizes of 0.1 on both axes, and have levels of 100,200,400, and 800.

8.2 Selecting AGN host galaxies

Now I will describe how I transform a catalog of fluxes into a targeted sample of LERGs. First the galaxies must be selected from the catalog. Then, since the radio emission catalog is separate from the multi-wavelength catalog, I will have to match radio emission to the right galaxy. This is complicated by the fact that radio emission extends much farther across the sky than the radius of the host galaxy. Finally, I will classify the radio galaxies into HERGs and LERGs.

8.2.1 Star, Quasar, and Galaxy Separation

Multiwavelength photometry offers many different methods of discriminating between stars and galaxies. In the following subsection, I will discuss two: color-color, and radial profile.

Color-Color diagrams compare the flux in two band passes to distinguish stars from galaxies. Two prominent methods are UVJ diagrams (Williams et al., 2009) and BzK diagrams (Daddi et al., 2004). Although there are subtle differences between each method, in general, these operate on the principle that galaxies will undergo additional reddening by cosmological redshift, and therefore be redder than stars.

Another object classification method is using the radius of the object. This requires accurate imaging of the galaxy, which is not always possible to acquire. The radius method uses the principle that stars are point sources and galaxies are extended objects. There is a degeneracy in this method between stars and quasars. Quasars are distant galaxies that host powerful AGN. The light from the galaxy is dominated by the AGN and appears as a point source on the sky.

To perform the object selection on my sample, I selected the galaxies from the catalogs by analyzing the effective radius (r_e) as calculated by GALFIT in the F160W and F125W band passes from the CANDELS survey. When plotted against each other (figure 8.2) these two bands show a bimodal distribution of point sources, that is, stars

and quasars, occupying the area of the plot with r_e <0.05 arc seconds, and the galaxies forming a long sequence beginning a r_e >0.05 arc seconds. This is because stars and quasars are point sources and galaxies are not. A break at 0.05 arc seconds can be seen in the F814W radius data also. I use this cut in radius to remove the stars and quasars from the sample.

For comparison, in figure 8.2, I show the results of the radius selection on a BzK plot. The point sources selected in the radius plot (top) appear as the red squares in the BzK diagram (bottom). Most of the red squares are on the stellar locus, and those in the galaxy cloud have experienced some reddening or have complex SEDs, and are therefore quasars. This confirms the results of the radius separation method.

Another method to separate stars, galaxies, and quasars, based on template fitting and bayesian statistics, is outlined in Appendix A.

8.2.2 Radio AGN Host Identification

The radio catalog and photometry catalog were not matched initially, so I assigned radio emission to host galaxies. In this subsection, I will discuss the algorithm I used to automatically assign radio emission to galaxies. Then I will show a few instances where the galaxy matching failed, and show how I resolved the assignment in those cases.

Likelihood ratios

Due to the vast extent and asymmetry of radio emission, the true K-band counterpart to a blob of radio flux may not be identified by conducting a minimum distance coordinate match. Rather than matching simply on coordinates, I calculate likelihood ratios for each proposed match in the Ks band within 5 arcseconds of the radio coordinates. The likelihood ratio, which was developed by Sutherland & Saunders (1992) and Wolstencroft et al. (1986), and used in Simpson et al. (2006), is calculated by the following equation:

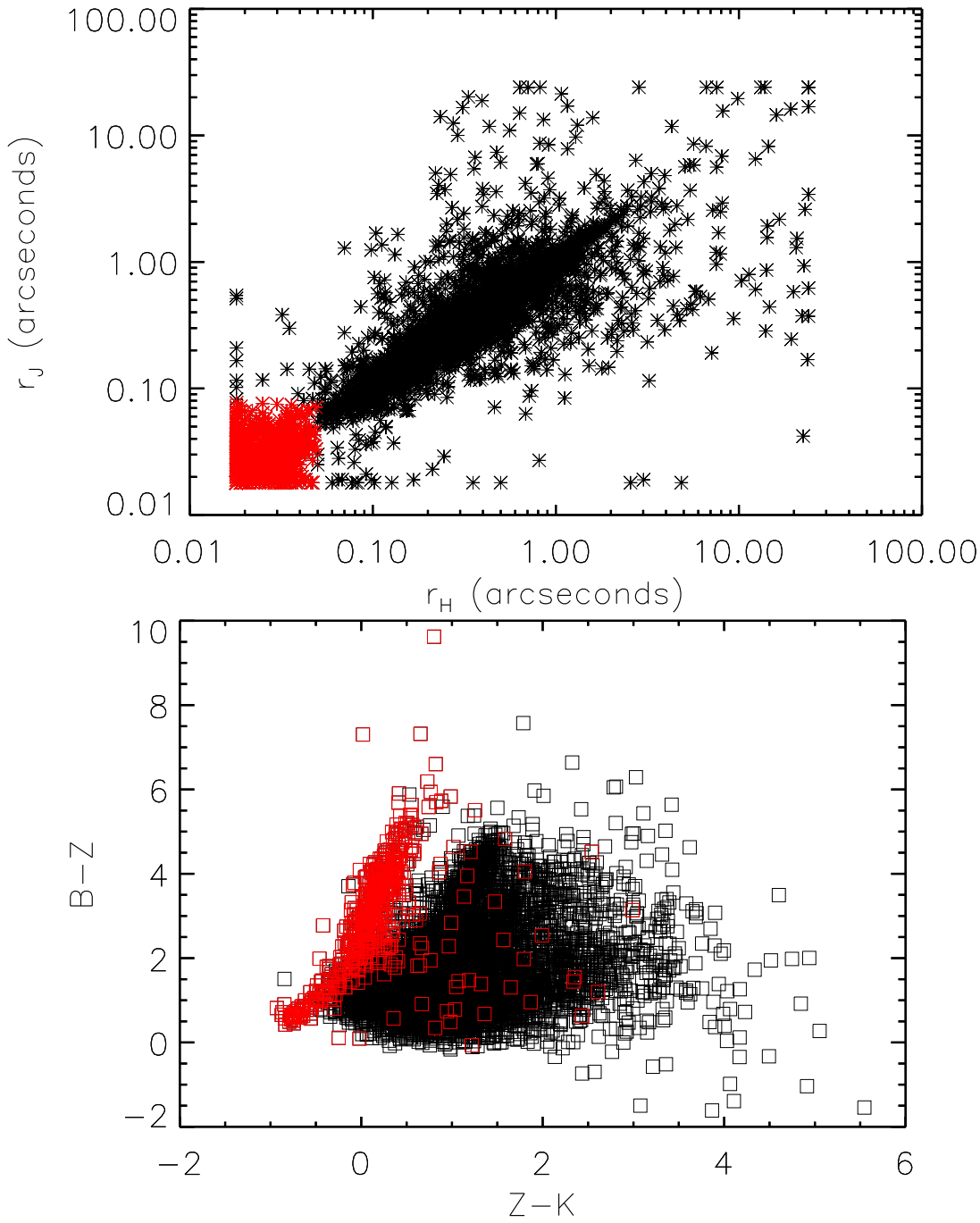

Figure 8.2: The top panel shows GALFIT effective radius measured in the J and H bands in the ULTRAVista field. The distinct division at radius = 0.05 arc seconds shows the boundary between resolved galaxies, and unresolved stars and quasars. For comparison, the lower panel shows most of the objects with r<0.05 arc seconds (red) fall on the stellar sequence BzK diagram, and those in the galaxy cloud are classified as quasars.

$$L_{kr} = \frac{Q(< m_k)\exp(-r_{kr}^2/2)}{2\pi\sigma_x\sigma_y N(< m_k)} \tag{8.1}$$

where Q($< m_k$) is the fraction of radio sources whose K band counterpart is brighter than the proposed match, r is the normalized separation on the sky between the radio coordinates and the K band source. It is described by the equation

$$r_{kr} = \sqrt{(\Delta_x/\sigma_x)^2 + (\Delta_y/\sigma_y)^2}. \tag{8.2}$$

σ_x and σ_y are the positional uncertainty taken from the radio catalogue. Δ_x and Δ_y are the positional offsets of the IR and radio coordinates on the sky. N($< m_k$) is the surface density of K band sources brighter than the proposed match. The K band source information was provided by Chris Simpson. The probability that a given K band source is the correct counterpart is given by:

$$P_{kr} = \frac{L_{kr}}{\sum_k L_{kr} + (1-q)}, \tag{8.3}$$

where q is the fraction of radio sources with K band counterparts in the catalogue. I initially assume q=0.9 and seed Q($< m_k$)=0.5. These parameters are updated automatically after each run. The process is repeated until the number of matches ceases to be increased.

Treatment of multicomponent sources

A multicomponent source is a radio source with multiple blobs attributed to one host galaxy. The majority of the multicomponent radio sources are properly assigned with the likelihood ratio method. However, due to the complexity of these objects, all multicomponent source matches were confirmed by eye, and there were 8 objects out of a total of 109 multicomponent sources which required reassignment. There were also 4 multicomponent radio sources for which there was no match. They were also included in the subset that received detailed visual inspection.

In four of the objects that required reassignment, the original mis-assignment was due to the radio coordinates not being representative of the AGN position. There were two instances where it was determined that two individual entries in the radio catalogue should be attributed to one source.

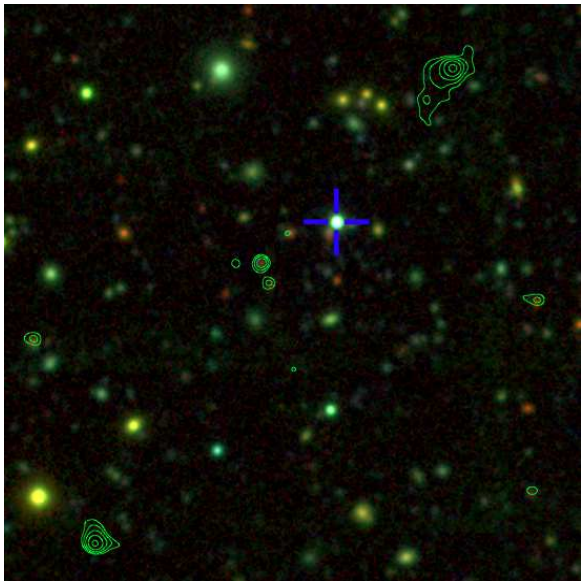

Figure 8.3: Radio Emission of a quasar at RA=150.3096, Dec=2.3991, with 1.4GHz radio contours and BzK photometry.

The radio source COSMOSVLADP−J100112.94+022423.3 was considered a complete object in the VLA catalogue, however it appears to be a hotspot of the quasar at 150.3096, 2.3991 in the UltraVISTA catalogue[1] with an ID number in the Muzzin et al. catalogue of 136421. The other hotspot component of the quasar is the radio source COSMOSVLADP−J100117.15+022301.1. The quasar is the most suitable choice for the source because there are no K band components at the hotspot positions, and the hotspots seem to be well aligned with the quasar, which is typical of double radio sources. The fluxes of the two hotspots have been combined (there was no noticeable core component), and assigned to the coordinates of the quasar.

The flux of radio source COSMOSVLADP J100129.35+014027.1 was combined with the flux of COSMOSVLADP J100131.09+014016.9 because it appeared in the radio image to be a single multicomponent source. The flux was assigned to the host galaxy

[1]The RA and DEC are in J2000 coordinates.

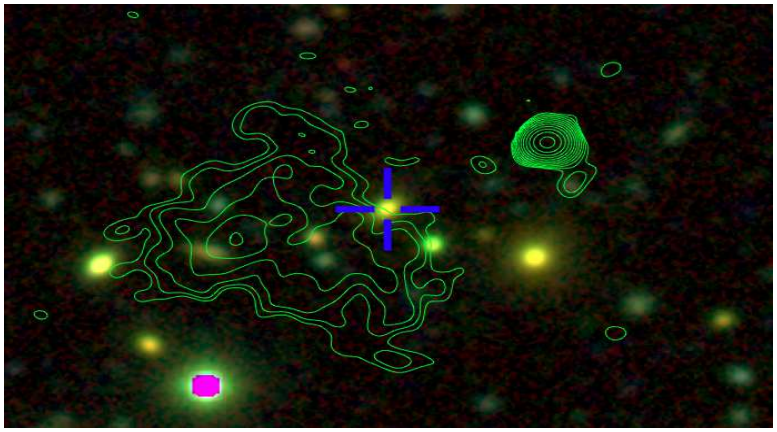

Figure 8.4: Host Galaxy 150.3760;1.6723 and associated radio emission, with 1.4GHz radio contours and BzK photometry.

at RA=150.3760, DEC=1.6723 in the UltraVISTA catalogue with an ID of 1005.

8.2.3 Radio-Loud Classification

Since I am operating under the assumption of the DCH, it is important to select the correct type of radio galaxy for this comparison. The best way to perform this selection is to compare line ratios to detect the presence of an accretion disk (Best & Heckman, 2012). A lack of emission lines produced by an accretion disk is indicative of inefficient accretion and the presence of a Low Energy Radio Galaxy (LERG). While High Energy Radio Galaxies (HERGs) efficiently drive gas away from the galaxy and strangle star formation, only LERGs can produce the right amount of feedback to balance the cooling of the hot halo and prevent new star formation. In lieu of spectral identification, a suitable alternative is to use the IR/Radio correlation which detects an excess of radio emission from the AGN. The q_{24} ratio (Appleton et al., 2004) is given by

$$q_{24} = \log(\frac{S_{24\mu m}}{S_{1.4GHz}}). \tag{8.4}$$

It is the ratio of ionizing photons from star formation in the 24 micron band, reprocessed in the dust, compared to the radio flux. A q_{24} value less than 0.03 indicates that the galaxy has an excess of radio emission, probably from an AGN. Objects below this

threshold in q24 are radio-loud (Ibar et al., 2008). Both the radio and 24 micron fluxes have been k-corrected. A k-correction is necessary to standardize the bandpasses and rest frame photometry (Hogg et al., 2002). Simpson used a M82 SED to k-correct the 24 micron fluxes for this research.

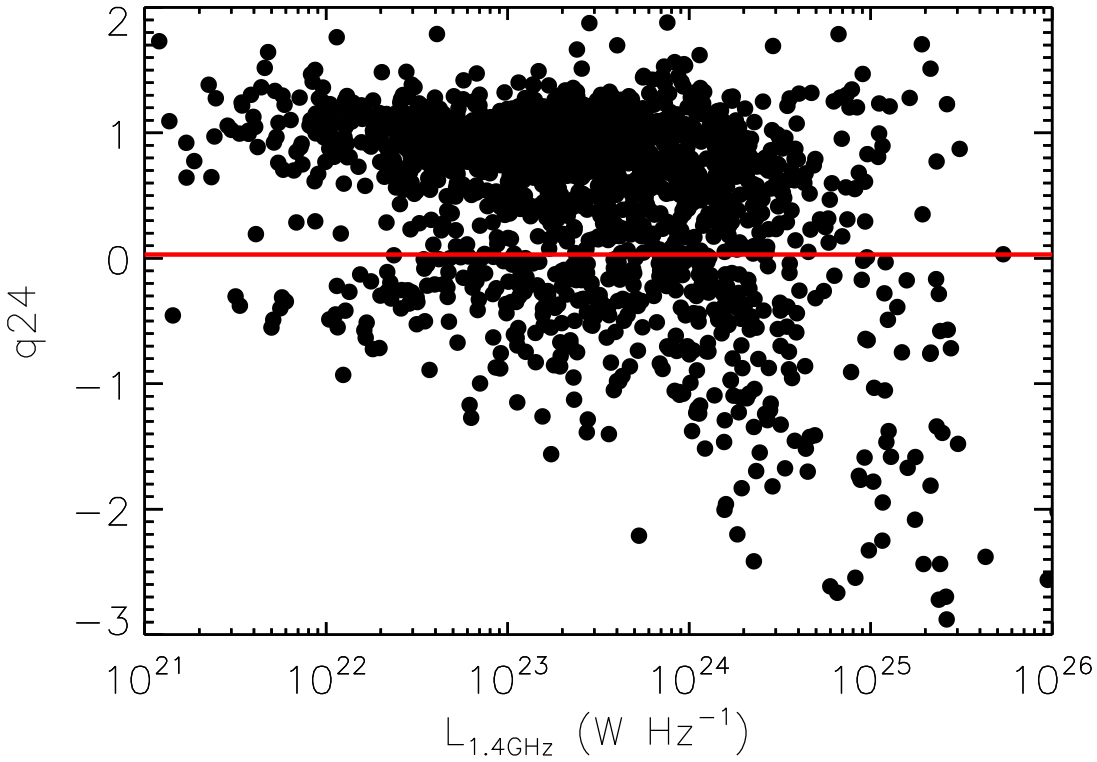

Figure 8.5: The q_{24} ratio shows the ratio of 24 micron flux to the 1.4GHz radio flux for all the radio emitting galaxies in the combined sample. Galaxies with an excess of radio emission have q_{24} values $<$0.03, and are classified as "Radio-Loud".

Without spectral confirmation of the accretion mode of the AGN, I cannot confirm if the sources are LERGs or HERGs, however, the Hine and Longair boundary for class A (low energy) and class B (high energy) AGN is $\approx 10^{25}$ W Hz^{-1} (Hine & Longair, 1979). Hine and Longair classes divide low energy AGN from high energy. Combining the q24 selection and the Hine and Longair classification, I can identify radio-loud, low energy sources, that will comprise the LERGs for this analysis. Figure 8.5 shows that most of the AGN lie below the q24 boundary, and therefore are radio-loud galaxies. Radio-loud galaxies below 10^{25} WHz^{-1} are the LERGs.

8.3 Testing the effect of AGN mass loss on host galaxies

With the sample of LERGs selected in the previous section, I can now test the radius evolution scenario proposed in Fan et al. (2008). I compare the radius of LERGs and massive elliptical galaxies, and their star formation activity. This will demonstrate the effects of rapid mass loss due to powerful AGN feedback, assuming the duty cycle hypothesis correctly leads me to select LERGs and the predecessors of HERGs.

8.3.1 Radius Comparison

AGN activity has been theorized to expand the radius of a galaxy (Fan et al., 2008). If the radii of the radio mode and inactive elliptical galaxies are similar, this is evidence that the effects of radio heating is common to all ellipticals, not just active radio galaxies, and suggests that a radio AGN duty cycle must play a primary role in the formation of all elliptical galaxies. The radio galaxies have been matched to three elliptical galaxies ($n_{Sersic} > 2.5$) with the closest stellar mass and redshift minimizing the equation:

$$s^2 = (\mathrm{M_{radio}} - \mathrm{M_{gal}})^2 + (\mathrm{z_{radio}} - \mathrm{z_{gal}})^2 \tag{8.5}$$

where s, is the difference between the mass of the radio and elliptical galaxy and the difference in redshift added in quadrature. Finally, the likelihood that the distribution of the radii of the radio and elliptical galaxies are drawn from the same population is calculated using a Kolmogorov-Smirnov test.

Kolmogorov-Smirnov test can be used to test if two samples are drawn from the same population. It calculates the cumulative histograms for both samples and produces a D value for the largest difference between two histogram bin heights. The p value is calculated from D, the KS statistic.

Figure 8.6 shows the results of the KS test on the radius, the probability and D value, binned by redshift. Initially the bin width is 0.1 wide in redshift, however, the KS test requires a minimum of 4 objects to perform the test, so when necessary, the redshift

bin size was expanded to accommodate at least 4 radio galaxies.

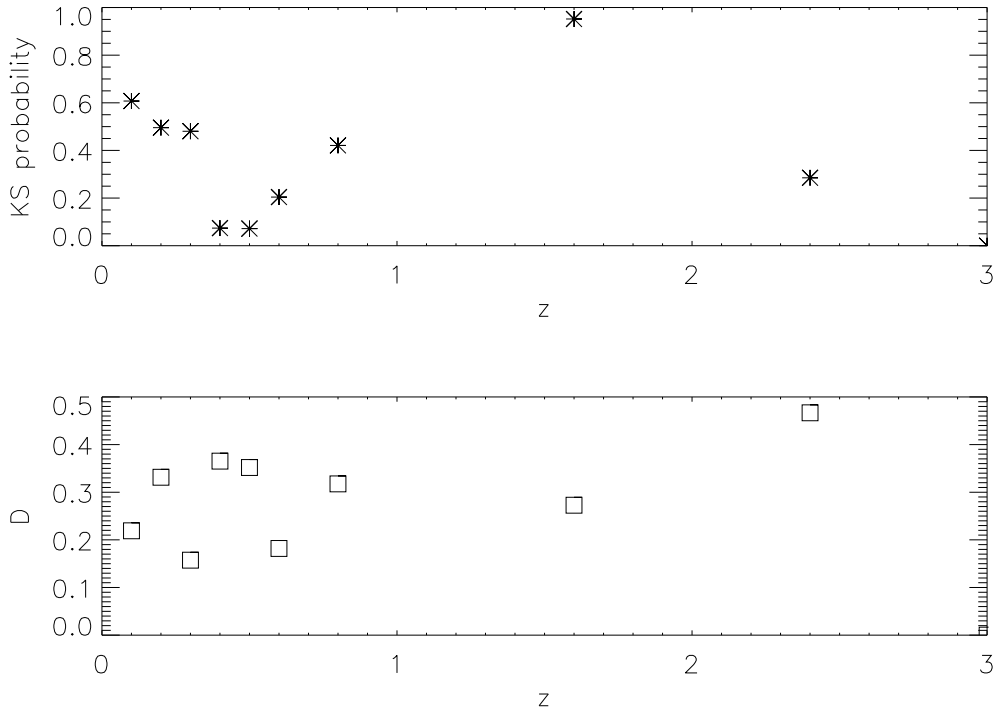

Figure 8.6: Results of KS test on radius of radio galaxies and the radius of ellipticals. When possible the test was run on subsets in redshift bins 0.1 wide, however the bin size was increased as much as necessary to include at least 4 radio galaxies.

Figure 8.6 identifies several redshift areas of interest that can be looked at in more detail. I have divided the sample into three redshift bins: $0.1< z <0.8$, $0.8< z <1.6$, and $1.6< z <3$, and the bins have 133, 9, and 9 radio galaxies, respectively. The bins have been selected to highlight the change in radius distribution after z$\approx$0.8, whilst keeping in mind the strong evolution of the radio luminosity function at redshifts of 2. Table 8.2 shows the result of the KS test after adopting the new, broader set of redshift bins.

Figure 8.7 shows the change in the mass-radius distributions with redshift. In the lowest redshift bin, the top plot of the figure, the radio and elliptical galaxies occupy the same space of the mass-radius plane. The KS test confirms with a low D value there is only a small separation of the distribution, but the probability that the objects are drawn from the same population is only 5 percent. Perhaps the apparent agreement

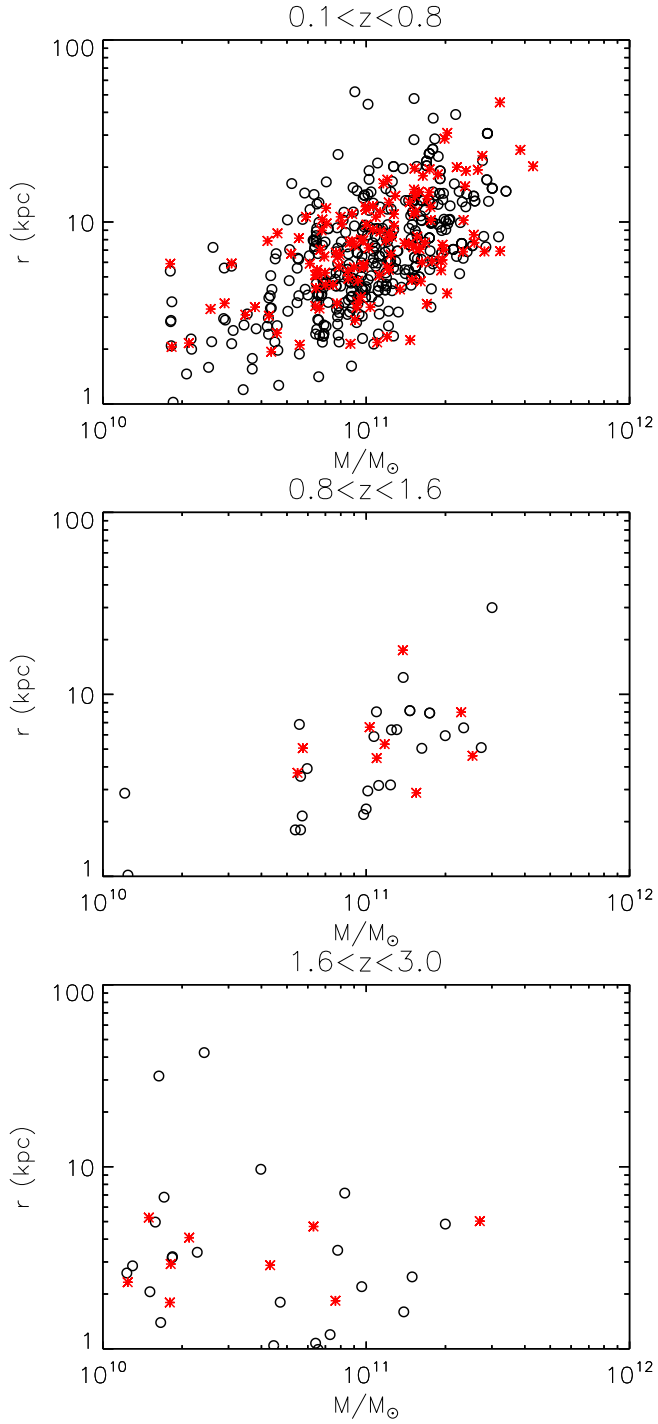

Figure 8.7: Log stellar mass vs. Radius in kpc. Elliptical galaxies with Sersic indices of greater than 2.5 are represented by black circles, and LERGs are represented by red asterisks. The three redshift bins are 0.1-0.8 (top), 0.8-1.6 (middle), and 1.6-3 (bottom). Average errors on the radii in each bin are: 3.6 kpc, 5.8 kpc, and 5.9 kpc, respectively. There is excellent agreement between the radius distribution of the two groups in the lowest redshift bin where completeness is highest, and the association holds, but becomes less clear at higher redshift.

Table 8.2: KS test results of the radius distribution. The cumulative distribution functions for each bin are presented in Appendix B.

Redshift	D	Probability
0.1-0.8	0.151	0.055
0.8-1.6	0.333	0.603
1.6-3	0.444	0.250

in size between the two populations would be better represented in the KS test results if the sample was subdivided by mass into bins larger and smaller than 10^{11} solar masses. This statistic appears to be at odds with the trend in the top plot of 8.7, and additional analysis will be completed to interpret this result.

The central plot of Figure 8.7 shows an intermediate redshift bin between 0.8 and 1.6. All of the radio galaxies are greater than 10.5 log mass, and have radii between 2 and 20 kpc. The underlying elliptical population may appear slightly smaller in radius than the radio, but the KS probability is large enough to conclude that the radio AGN hosts are a subset of the main elliptical population.

The lowest plot of Figure 8.7 is of the redshift bin 1.6 to 3. The radio galaxies in this bin are less massive in general than those in previous bins. This is interesting because it hints that the data are sensitive enough to show some hierarchical formation over this large timescale. Also, the radio galaxies appear slightly smaller on average than the more massive, nearby, radio galaxies.

From visual inspection, the elliptical galaxies at high redshift are not as closely matched in mass, compared to the first bin; but this is, in part, because sampling becomes sparse at these redshifts. The results of the KS test show that there is a comparatively larger separation, D value, between the cumulative distributions of the radio and elliptical radii. This seems to be mostly due to some large elliptical radii. Nevertheless, the KS probability is sufficiently large to conclude that the radio and elliptical galaxies at this redshift are drawn from the same population.

8.3.2 Star Formation Activity

In addition to puffing up the elliptical galaxies, LERGs may quench star formation in all ellipticals by balancing the cooling haloes (Best et al., 2006). The rest frame (U-V) vs (V-J) plane is a diagnostic to determine the color, and therefore the star formation activity of a galaxy (Williams et al., 2009). It has the advantage of not being sensitive to reddening by dust, because the slope of the star formation and quiescent sequence is the same as the change in color due to increasing A_v (Williams et al., 2009). Therefore, compared to other color-bimodality diagnostics such as UBV, it is less likely that dusty star forming galaxies appear in the red sequence. I use data from Chris Simpson which has been k-corrected and had rest-frame U-V and V-J colors by determining the best-fitting spectral energy distribution from a library of 10^5 galaxy models constructed from two exponentially-declining bursts of star formation covering a range of strengths, e-folding and cut-off times, metallicities, delay intervals, and extinctions. The rest frame colors were calculated by Simpson using the MUSYC U, V, and J filters. I set the boundary for the red sequence as $(U-V) > 0.88(V-J)+0.89$, because there is a clear separation between the red sequence and the cloud in the lowest redshift bin at this threshold.

Figure 8.8 shows that, out to a redshift of 1.6, the majority of low power AGN are hosted in quenched, red galaxies. At redshifts greater than 1.6, the radio mode hosts are in the star forming part of the UVJ diagram. The broad distribution of the radio galaxies across the V-J axis indicates that some radio galaxies are not star forming galaxies, and others are dusty star forming galaxies. Additionally, the radio galaxies in the highest redshift have 1.4GHz luminosities near the Hine and Longair boundary, and this information in conjunction with the knowledge that the number density for LERGs/Radio Mode AGN sharply decreases at redshifts greater than two (Simpson et al., 2012), may lead to the conclusion that the radio galaxies in this bin are not LERGs, but quasar mode HERGs which are theorised to be responsible for initialising the duty-cycle of star formation quenching by driving the gas into the halo or out of the galaxy entirely (Best et al., 2014).

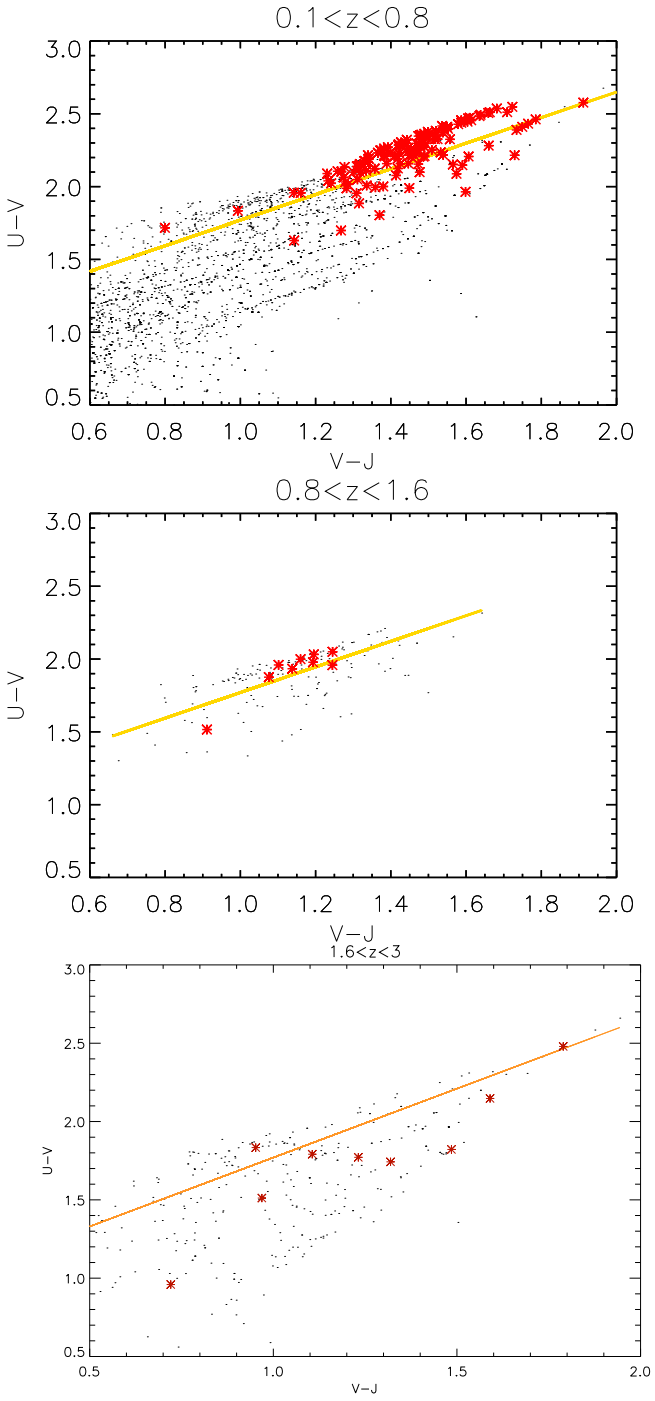

Figure 8.8: Star formation activity in 3 redshift bins ($0.1 < z < 0.8, 0.8 < z < 1.6, \mathrm{and} 1.6 <$ z < 3). The yellow line represents the boundary between the red sequence and blue cloud. Most radio galaxies (represented by red asterisks) are in the red sequence, except for the highest redshift bin. Background points show the location of all the galaxies in that redshift bin, and clearly show the locations of the blue cloud and red sequence.

8.4 Discussion

Are the LERGs the same host in different phases of the duty-cycle, or two inherently different objects with a few similar characteristics? The K-S tests suggest that LERGs and the control elliptical sample are from the same distribution. At this point, it is not possible to distinguish the two populations. A matched, statistically significant sample at high redshift is required. If the results here are a good representation of the actual population then the presence of a LERG does not indicate that a HERG rapidly expelled mass from the galaxy at earlier times, and caused the radius of these galaxies to expand.

In the Fan et al paper, it is suggested that the effective radius of ellipticals which once hosted a powerful quasar expands after suffering massive mass loss due to AGN winds. If the duty cycle hypothesis enables me to properly select the galaxies, the LERGs in figure 8.7 should increase in size up to twice original effective radius over a timescale of ≈ 2 gigayears. Assuming I have correctly selected LERGs as the progeny of HERGs, then the change in radius is much larger than what Fan et al predicts. The average radius of the high redshift galaxies is approximately 5 kpc and can increase up to several tens of kpc in the present epoch. This surpasses Fan et al's prediction.

Additionally, Fan et al make a distinction between the growth of large and small ellipticals. They say that if a galaxy is less than $2\times10\ M_{\odot}$, the AGN is too weak, and growth is driven instead by supernova and stellar winds. Have I actually selected these galaxies instead? Four of the nine LERGs in the highest redshift bin fall below this mass limit, however, I have looked at their radio luminosities and can confirm that they are active galaxies with powerful AGN, see figure 8.5. So, although there are some less massive galaxies present in the sample, they should display the behavior associated with powerful AGN activity.

Finally, there is additional evidence that 1.4 GHz radio galaxies are not a separate morphological class from general radio galaxies. Rees et al. (2016) found that nearly 50 per cent of radio-AGN possess a VLBI detected counter- part, and that those objects with a VLBI counterpart show no discernible bias towards specific stellar masses, red-

shifts or star formation. This is at odds to the DCH that, in its simplest form, relies on a strong dichotomy between HERGs and LERGs.

Further analysis of this dataset may yield better results. Additionally large, deep radio surveys will complete samples out to higher redshift, populating the highest redshift bin, and allowing better comparisons. For now, I have isolated radio-mode sources and ellipticals from K band selected catalogs and have observed their colors and location on the mass-radius plane at various redshifts. It is clear that the high mass $M_* > 10^{11}\mathrm{M}_\odot$ region becomes more populated by LERGs and quiescent ellipticals in the present day than at redshifts around 3. Additionally, from the color information, I confirm that the host galaxies of the LERGs decrease in star formation over time, and become red.

8.5 Summary

Combining data from the COSMOS and UKIDSS fields, I tested the theory that intermittent injection of feedback from LERGs into the intergalactic medium forms quiescent elliptical galaxies by balancing the cooling from the galactic halos. I conduct KS tests on the distribution of the radii of LERGs and elliptical galaxies out to a redshift of 3 and find that the distributions are drawn from the same population. Plots of the mass-radius plane agree with the KS test results, and UVJ plots show that the star formation activity is quenched in LERG hosts out to a redshift of approximately 2. The similarity of the radii between active and passive elliptical galaxies agrees with the DCH which says they are the same galaxy but in different phases of the duty cycle. However, the LERG star formation activity seen in 2 of the 3 redshift bins is contrary to the DCH's proposal of AGN quenching star formation. Spectral classification of LERGs will clarify if this shows a flaw in the DCH, or shows a lack of precision in one's ability to classify AGN without spectra.

Chapter 9

Part Two Conclusions and Future Work

In this part, I test the theory that rapid mass loss can cause a dramatic size increase in AGN hosts (Fan et al., 2008). I also test the duty cycle hypothesis (Best et al., 2014), which says the star formation in massive elliptical galaxies is quenched by AGN feedback.

In chapter 6, I describe the surveys I combine to obtain the maximum area coverage that is necessary to recover enough low luminosity radio-loud AGN hosts. All of the research in part 2 was conducted with publicly available survey data. I also used a publicly available catalog of morphological parameters derived from HST data.

In chapter 7, I guide the reader through the process of deriving essential physical quantities from the photometric survey data, and demonstrate the selection process of low luminosity radio loud AGN (LERGS). Finally, I present three tests of the galaxy evolution theories. First, I examine a plot of mass versus radius of LERGS compared to a control sample of non active elliptical galaxies in three different redshift bins. The LERGS do not appear to have a preferential mass range compared to the control sample, nor do they appear to have significantly larger radii. This test of the Fan theory proves negative, however it supports the duty cycle hypothesis, in which non active

ellipticals and LERGS are the same type of objects in different phases of the duty cycle. This is confirmed by a K-S test that does not produce a critical value high enough to conclude that the LERGS are drawn from a different population than the control sample. The third test, an analysis of the star formation activity of the LERGS shows that they are mostly found in the non star formation part of the UVJ diagram, indicating that although these galaxies host low luminosity radio loud AGN, they share the star formation and radial properties of non active elliptical galaxies. However, a few galaxies fall in the star formation part of the diagram and these have been flagged for follow up in future work.

More future work could be done improving mass estimation and radius estimations and increasing the sample size of objects with reliable radius estimations. More radii are needed in the higher redshift bins to begin to make a significant comparison. Additionally, the research would benefit from matching the control sample in magnitude as well as redshift and mass. I will also investigate the cause of the low probability from the KS test for the first bin in 8.7. The figure 8.6 suggests that within the $0.1 < z < 0.8$ bin, there is not good agreement between redshifts of 0.4-0.5. However, the statistics in all other bins are high enough to confirm the null hypothesis. I will check the matching of ellipticals and LERGs in this range, and experiment with different weightings of the redshift and mass matching. I plan to write up this research as a paper after improving the classification of the LERG sample with spectroscopy and/or investigating the LERGs that appear in the dusty star former part of the UVJ diagram.

Appendix A

Star/Galaxy/Quasar Separation

A.1 Literature Review

An unavoidable step in doing science with large surveys is classifying objects and isolating the population of interest in a timely and reliable fashion. Also photometric redshifts, which are calculated using template fitting, rely on correctly identifying the type of object. For the work in this thesis, a large sample size of objects is necessary to do meaningful statistical analysis. However, separating over 200,000 objects by eye is not time efficient and is prone to error. There are methods to separate stars from galaxies, but quasars are usually separated by eye or spectra.

The isolation of the quasar population is very important for statistics with the galaxy population. Since quasars are very luminous, the mass to light ratio could make them appear as very high mass galaxies, if they are left in the galaxy population. Therefore, it is necessary to exclude them from the galaxy population. I will build upon the currently available star/galaxy separation techniques to create a quasar identification method. The advantages and disadvantages of several of the most popular star/galaxy separations are discussed below.

Many surveys use color plots to distinguish stars from galaxies (Daddi et al., 2004; Caputi et al., 2011; Baldry et al., 2010; Muzzin et al., 2013). These plots can show

two distinct groups of objects. The objects that form a fairly coherent sequence are classified as stars, and those that appear in a large cloud are galaxies. These plots work because a star is characterized by a single blackbody curve, therefore stars are constrained to follow a tight locus of colors. Galaxies are composed of many stars and therefore their SED is composed of many blackbody curves. This results in the colors of galaxies not being as tightly constrained. The reddening effects of cosmological redshift also affect galaxies, and so in addition to having composite SEDs the galaxies also depart the color locus that stars follow due to being redshifted.

There are several disadvantages to this method. First, the classification is highly sensitive to the photometric quality of the bandpasses. Secondly, the dividing line for stars and galaxies must be decided upon visually, and there is usually not a completely clear division between the two populations. Third, and most importantly for this work, there is not an easy way to identify quasars.

Another star/galaxy separation tool is the Class Star output in SourceExtractor (Bertin & Arnouts, 1996). The Class Star output is a morphological discriminant that uses a neural networks code based on the size on the sky to determine if the object is a star or galaxy. This method is reliable to a certain magnitude, but results become less reliable when the signal-to-noise quality is poor.

The Bayesian algorithm developed by Simpson et al. (2013) delivers an a priori method of classifying stars and galaxies, and also outputs a reliability factor for the classification. SED classification is robust at higher redshifts where morphological information is less reliable. The program works by fitting SEDs of different object types to the object. The program uses prior knowledge about morphology, and expected number density to guide the classification. The best fit is determined by the formula:

$$\frac{P_g}{P_s} = \frac{1-S}{S}\frac{N_g(K)}{N_s(K)}\frac{\int_{z_{min}}^{z_{max}} P(z|K)\exp(-\chi_g^2/2)dz}{\exp(-\chi_s^2/2)} \tag{A.1}$$

which compares the probability that an object is a galaxy to the probability that an object is a star. Sometimes this is referenced as $Pgal_{star}$. S is the Class Star parameter from SourceExtractor which is useful for distinguishing between nearby galaxies and

stars. N is the expected number density of stars (Jarrett, 1992), and galaxies (Gardner et al., 1993), and z min/max are set by the user and are the limits of the photometric redshifts. $P(z|K)$ is the prior of the redshift distribution for galaxies, and χ^2 is the fit of the template to the SED, the product of these two quantities is from EAZY's (Brammer et al., 2008) output.

When run on a spectroscopic sample it had 4/305 stellar mis-classifications, and 20/3116 galaxy mis-classifications (Simpson et al., 2013). In addition to being a reliable star/galaxy separation technique that outputs probability of each classification, the Bayesian method should be easily expandable to include the probability that the object is a quasar.

A.2 Bayesian Star/Galaxy/Quasar Separation

The two main steps necessary to extend Simpson et al's (2013) method to include quasars are: (1) derive the quasar analogue to equation A.1, and (2) make quasar templates that unambiguously fit quasars better than stars and galaxies.

The first step is relatively straightforward. First I constrain all the probabilities add up to 1. That is, $P_g + P_s + P_q = 1$. Then I compare the probability that the object is a quasar to its probability of being a star or galaxy. It follows from equation A.1 that:

$$\frac{P_q}{P_s} = \frac{N_q(K)}{N_s(K)} \frac{\int_{z_{min}}^{z_{max}} P(z|K) \exp(-\chi_q^2/2) dz}{\exp(-\chi_s^2/2)} \tag{A.2}$$

$$\frac{P_g}{P_q} = \frac{P_g}{P_s} / \frac{P_q}{P_s} \tag{A.3}$$

describe the relationship of the probabilities that a quasar is a star or galaxy. The probabilities are normalized to attain the absolute probabilities.

Note that there is no source extractor Class Star value for the $Pqso_{star}$. This is because SourceExtractor only assigns a value between 0 and 1 of an object being a point source or not. Also, the quantity $P(z|K)$, the redshift distribution of quasars in different magnitude bins in equation A.2, is created by taking a slice in K band magnitude and

redshift space and calculating the absolute magnitude of a quasar in that slice. Then the quasar luminosity function (Croom et al. 2004, Richards et al. 2006) is used to get the space density at that luminosity. Then the space density is multiplied by an area of 1 degree^2 on the sky to get the number of quasars per square degree in a 1-magnitude wide bin with that K band magnitude in that redshift slice. This quantity is proportional to $P(z|K)$, and the normalization is done by EAZY.

The second step, creating a good set of templates that yield low χ^2 values, is essential for the Bayesian technique to work. The templates used for the photometric redshift calculations have been demonstrated by this work to be a good set of templates for the data. A variety of templates were used to achieve the best fit for various objects. A set of stellar spectral templates of Allard et al. (2011) were used. These templates cover a wide range of effective temperatures and surface gravities. From these templates, additional templates for main-sequence binaries have been constructed (Simpson et al., 2013). The galactic photometric redshifts use a template set by Charlot and Bruzal (2007). This template set is based on Bruzual & Charlot (2003), and includes models of galaxies with pulsating AGB stars. Such objects are very red, and very bright, and can produce excess near-infrared flux. If left unaccounted for they could cause an incorrect template fit during the redshift determination process. These are the same templates that were used in Simpson et al. (2013) and should work equally well for this data set.

Simpson made the quasar templates from a combination of templates from SDSS QSO spectrum of Vanden Berk et al. (2001) and the composite QSO SED of Richards et al. (2006). Mildly reddened spectra were created using the Pei (1992) parametrisation of the SMC reddening law. Then the spectral indices of the blue and red elements (i.e. above and below λ=14150 Å) were calculated by the following formula:

$$S_{new} = S_{old} \times \left(\frac{\lambda}{\lambda_{dustbump}} \right)^{\Delta\alpha} \tag{A.4}$$

to diversify the template set by accounting for variations in the AGN and dust component of the quasar. $\Delta\alpha$ is the amount by which the spectral index was varied, and in

this instance it was incremented in steps of 0.1 over the range -0.3 to 0.3.

EAZY also requires a template error function to be created. The template error function is a comparison between the fit of the template SED to the observed SED. The stellar templates do not require a template error function because it is believed that the stellar templates accurately cover the range of SEDs, and galaxy templates already have a template error function, but the new quasar template set does not. So, after creating many permutations of the quasar spectra, the template error function was created in a method similar to Brammer et al. (2008). First, I use EAZY to find the best fitting

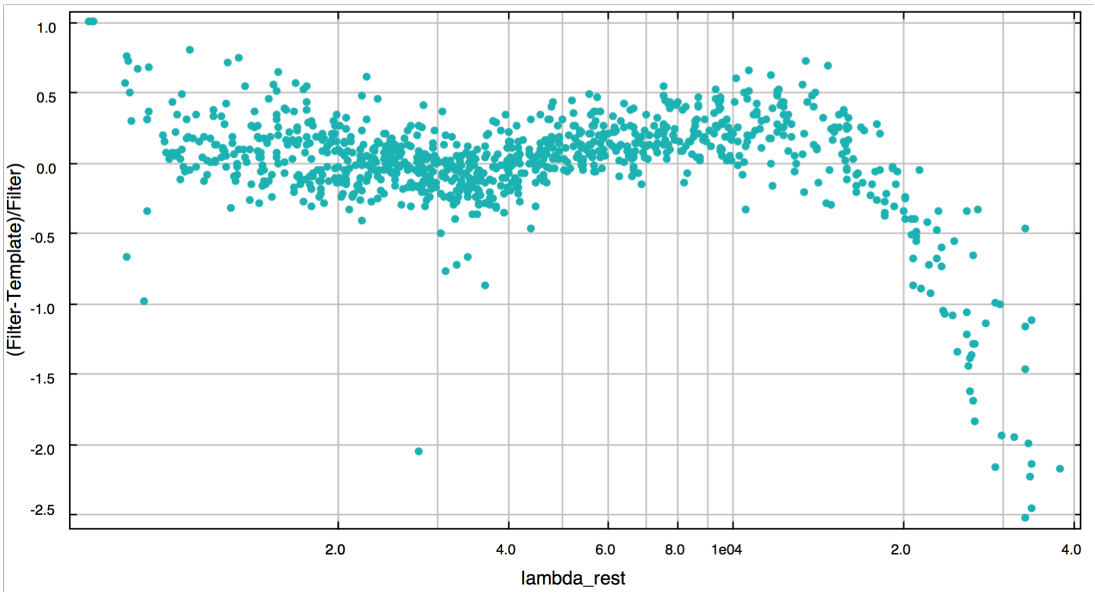

Figure A.1: This figure shows the quasar template error function before the absolute value of the median was taken. It indicates that the Spitzer data are not well fit by the current set of templates. The decline in the IR and scatter in the rest frame UV needs to be investigated in more detail to determine all the contributing factors.

quasar spectral template for each spectrally confirmed quasar in our sample. Then, I calculate the separation of the observed and the template flux at each rest-frame wavelength, see figure A.1. Then the absolute value of the residuals are binned by wavelength and extrapolated to the ends of the wavelength range of the template grid.

A.3 Preliminary Results

The program was tested on a spectroscopic subset comprised of the zCOSMOS data with the spectroscopic confidence class of 3 or 4 for stars and galaxies, and 13 or 14 for quasars (which claims to have 99.5% confidence in quality of the redshift) and a sample of 107 broad line AGN from the COSMOS/XMM survey (Trump et al., 2007). Only 39 out of 445 stars were misclassified. 64/5538 galaxies, and 62 out of 191 quasars were mis-classified. The distribution of sources can be seen in Figure A.2 and Table A.1. Figure A.2 shows the probability plane of $\mathrm{Log}_{10}(\frac{P_g}{P_q})$ vs. $\mathrm{Log}_{10}(\frac{P_g}{P_s})$. The position of the points show the classification of the object based on the Bayesian algorithm, and the colors represent the spectral classification. Objects in Quadrant I are assigned as galaxies. Objects in Quadrant II and III are classified as stars, and objects in Quadrant IV are quasars. Green represents galaxies, red represents stars, and yellow represents quasars, as defined by zCOSMOS spectra.

Table A.1: The spectroscopic "real" classification is read along the row, and the Bayesian assigned type is read down the column, e.g. there were 62 quasars classified as galaxies.

	Assigned Type		
Real Type	G	S	Q
Galaxy	5474	36	28
Star	35	406	4
Quasar	62	0	129

Another significant result is that when the entire catalogue is run through the classification program, the quasars are grossly over represented. The quasar luminosity function (Croom et al., 2004; Richards et al., 2006) predicts approximately 300 quasars per square degree of sky, and I calculate about 10 times as many. However, despite altering the quasar sky density, templates, and template error function, it was not possible to prevent the mis-classification of quasars and galaxies.

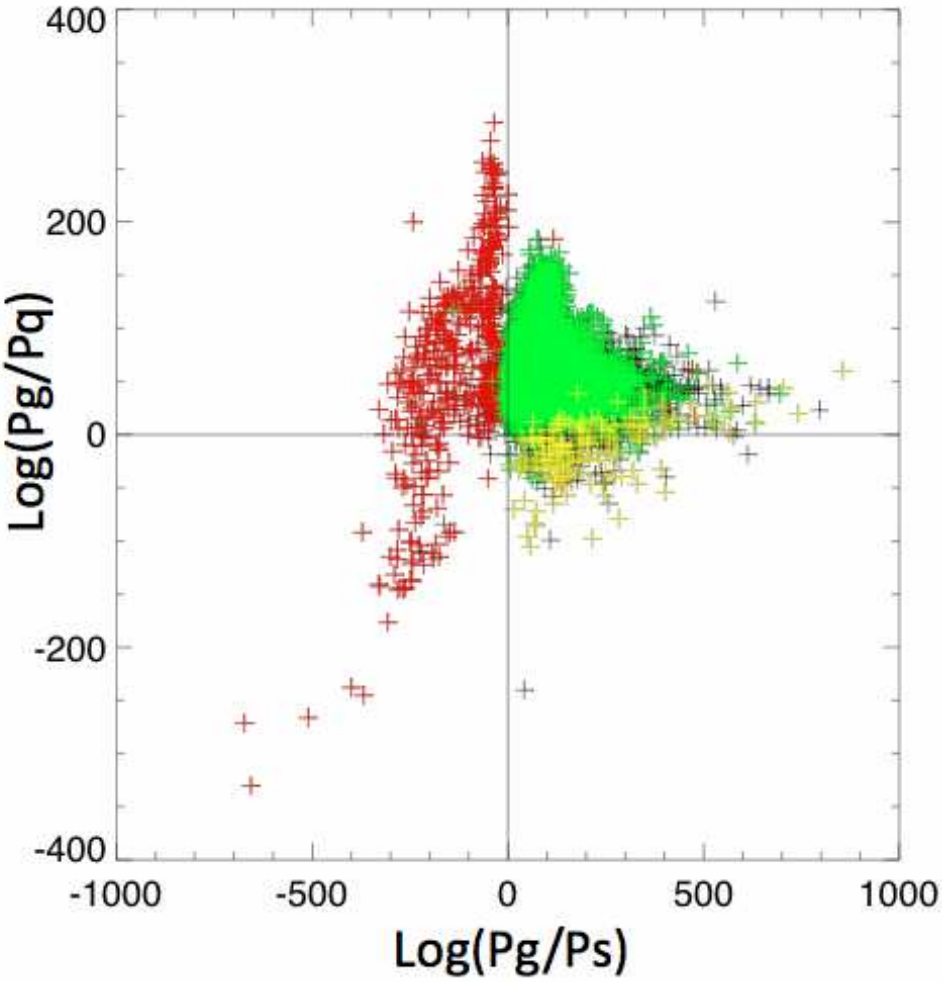

Figure A.2: Results of the Star/Galaxy/Quasar separation. The color of the points represents the spectroscopic classification: red=star, green=galaxy, and yellow=quasar. The position on the plot represents the Bayesian classification: Quadrant I=galaxy, Quadrant II & III = star, and Quadrant IV = quasar. Although the stars and galaxies are well separated, the quasars tend to spread into the galaxy quadrant.

Appendix B

Cumulative histograms for KS tests

Here I present the cumulative histograms that accompany the KS test results presented in table 8.2. I have plotted cumulative histograms of two populations to determine if the populations are identical, or not. The histograms are for the redshift bins: $0.1 < z < 0.8, 0.8 < z < 1.6, \text{and}, 1.6 < \text{z} < 3.0$. The control galaxies, plotted in black, are identified as elliptical galaxies without radio AGN activity. The red histogram is comprised of the the low energy radio galaxies (LERGs). In the lowest redshift bin, the histograms show that the populations are almost identical, except for a slight difference below 6 kpc. The higher redshift bins are limited by a small amount of data. There are only 9 LERGs in each of the higher redshift bins. There may be some agreement between the populations in the middle redshift bin, but in the $1.6 < z < 3.0$ bin, the cumulative distribution functions are very different.

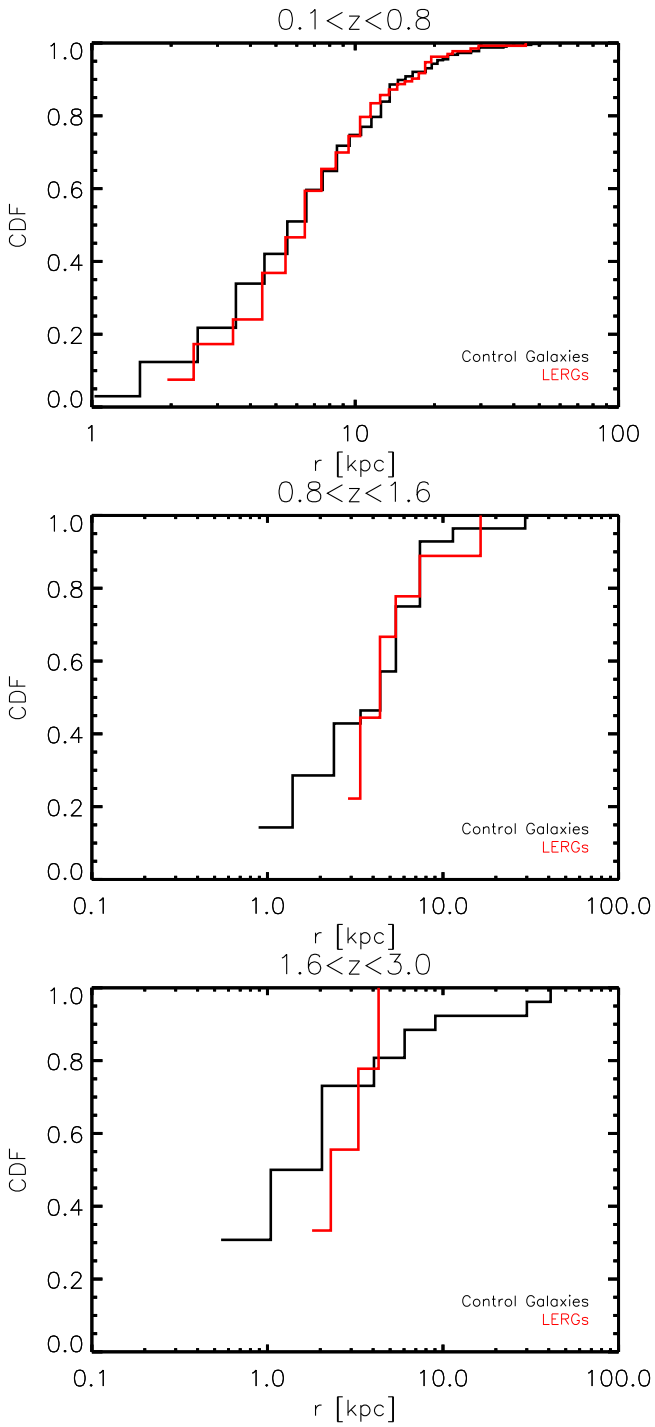

Figure B.1: The cumulative histograms of the control galaxies (non-active ellipticals), black, and the LERGs, red. The plots are in order of increasing redshift from top to bottom, they are $0.1 < z < 0.8, 0.8 < z < 1.6, \text{and}, 1.6 < \text{z} < 3.0$. There is good agreement between the populations in the $0.1 < z < 0.8$ bin. The other redshift bins show large discrepancies between the control population and the LERGs.

Bibliography

Aartsen, M. G., et al. 2014, arXiv:1401.2046

Abe, K., Abgrall, N., Aihara, H., et al. 2011, Nuclear Instruments and Methods in Physics Research A, 659, 106

Abell, G. O. 1958, ApJS, 3, 211

Addison, G. E., Huang, Y., Watts, D. J., et al. 2015, ArXiv e-prints, arXiv:1511.00055

Ali-Haïmoud, Y., & Bird, S. 2013, MNRAS, 428, 3375

Allard, F., Homeier, D., & Freytag, B. 2011, in Astronomical Society of the Pacific Conference Series, Vol. 448, 16th Cambridge Workshop on Cool Stars, Stellar Systems, and the Sun, ed. C. Johns-Krull, M. K. Browning, & A. A. West, 91

Allen, S. W., Evrard, A. E., & Mantz, A. B. 2011, ARA&A, 49, 409

Allen, S. W., Schmidt, R. W., & Fabian, A. C. 2001, MNRAS, 328, L37

Appleton, P. N., Fadda, D. T., Marleau, F. R., et al. 2004, ApJS, 154, 147

Bahé, Y. M., McCarthy, I. G., & King, L. J. 2012, MNRAS, 421, 1073

Baldry, I. K., Balogh, M. L., Bower, R. G., et al. 2006, MNRAS, 373, 469

Baldry, I. K., Glazebrook, K., Brinkmann, J., et al. 2004, ApJ, 600, 681

Baldry, I. K., Robotham, A. S. G., Hill, D. T., et al. 2010, MNRAS, 404, 86

Baldry, I. K., Alpaslan, M., Bauer, A. E., et al. 2014, MNRAS, 441, 2440

Balogh, M. L., McGee, S. L., Mok, A., et al. 2014, MNRAS, 443, 2679

Battye, R. A., & Moss, A. 2014, Physical Review Letters, 112, 051303

Becker, M. R., & Kravtsov, A. V. 2011, ApJ, 740, 25

Becker, M. R., McKay, T. A., Koester, B., et al. 2007, ApJ, 669, 905

Beers, T. C., Flynn, K., & Gebhardt, K. 1990, AJ, 100, 32

Benson, B. A., de Haan, T., Dudley, J. P., et al. 2013, ApJ, 763, 147

Bertin, E., & Arnouts, S. 1996, A&A Supp, 117, 393

Best, P. N., & Heckman, T. M. 2012, MNRAS, 421, 1569

Best, P. N., Kaiser, C. R., Heckman, T. M., & Kauffmann, G. 2006, MNRAS, 368, L67

Best, P. N., Kauffmann, G., Heckman, T. M., et al. 2005, MNRAS, 362, 25

Best, P. N., Ker, L. M., Simpson, C., Rigby, E. E., & Sabater, J. 2014, MNRAS, 445, 955

Beutler, F., Saito, S., Brownstein, J. R., et al. 2014, MNRAS, 444, 3501

Bird, S., Viel, M., & Haehnelt, M. G. 2012, MNRAS, 420, 2551

Bîrzan, L., Rafferty, D. A., McNamara, B. R., Wise, M. W., & Nulsen, P. E. J. 2004, ApJ, 607, 800

Biviano, A., Murante, G., Borgani, S., et al. 2006, A&A, 456, 23

Bohringer, H., Chon, G., & Collins, C. A. 2014, A&A, 570, A31

Bondi, M. Hoyle, F. 1944, MNRAS, 104, 273

Booth, C. M., & Schaye, J. 2009, MNRAS, 398, 53

Bower, R. G., Benson, A. J., & Crain, R. A. 2012, MNRAS, 422, 2816

Bower, R. G., Benson, A. J., Malbon, R., et al. 2006, MNRAS, 370, 645

Brammer, G. B., van Dokkum, P. G., & Coppi, P. 2008, ApJ, 686, 1503

Brammer, G. B., Whitaker, K. E., van Dokkum, P. G., et al. 2009, ApJ, 706, L173

Bruzual, G., & Charlot, S. 2003, MNRAS, 344, 1000

Budzynski, J. M., Koposov, S. E., McCarthy, I. G., McGee, S. L., & Belokurov, V. 2012, MNRAS, 423, 104

Caputi, K. I., Cirasuolo, M., Dunlop, J. S., et al. 2011, MNRAS, 413, 162

Cardelli, J. A., Clayton, G. C., & Mathis, J. S. 1989, ApJ, 345, 245

Carilli, C. L., Perley, R. A., & Harris, D. E. 1994, MNRAS, 270, 173

Carilli, C. L., & Rawlings, S. 2004, New Astronomy Reviews, 48, 979

Carlberg, R. G., Yee, H. K. C., & Ellingson, E. 1997a, ApJ, 478, 462

Carlberg, R. G., Yee, H. K. C., Ellingson, E., et al. 1997b, ApJ, 476, L7

Cattaneo, A., Dekel, A., Devriendt, J., Guiderdoni, B., & Blaizot, J. 2006, MNRAS, 370, 1651

Cimatti, A., Cassata, P., Pozzetti, L., et al. 2008, A&A, 482, 21

Cirasuolo, M., McLure, R. J., Dunlop, J. S., et al. 2007, MNRAS, 380, 585

Cole, S., Lacey, C. G., Baugh, C. M., & Frenk, C. S. 2000, MNRAS, 319, 168

Cowie, L. L., Songaila, A., Hu, E. M., & Cohen, J. G. 1996, AJ, 112, 839

Croom, S. M., Smith, R. J., Boyle, B. J., et al. 2004, MNRAS, 349, 1397

Croton, D. J., Springel, V., White, S. D. M., et al. 2006, MNRAS, 365, 11

Cui, W., Borgani, S., & Murante, G. 2014, MNRAS, 441, 1769

Daddi, E., Cimatti, A., Renzini, A., et al. 2004, ApJ, 617, 746

Dalla Vecchia, C., & Schaye, J. 2008, MNRAS, 387, 1431

Danese, L., de Zotti, G., & di Tullio, G. 1980, A&A, 82, 322

Dolag, K., Borgani, S., Murante, G., & Springel, V. 2009, MNRAS, 399, 497

Driver, S. P., Davies, L. J., Meyer, M., et al. 2015, ArXiv e-prints, arXiv:1507.00676

Driver, S. P., Hill, D. T., Kelvin, L. S., et al. 2011, MNRAS, 413, 971

Driver, S. P., Wright, A. H., Andrews, S. K., et al. 2016, MNRAS, 455, 3911

Dunlop, J. S., & McLure, R. J. 2003, in The Mass of Galaxies at Low and High Redshift, ed. R. Bender & A. Renzini, 268

Dunlop, J. S., McLure, R. J., Kukula, M. J., et al. 2003, MNRAS, 340, 1095

Dyson, F. W., Eddington, A. S., & Davidson, C. 1920, Philosophical Transactions of the Royal Society of London Series A, 220, 291

Eke, V. R., Baugh, C. M., Cole, S., et al. 2004, MNRAS, 348, 866

Evrard, A. E., Bialek, J., Busha, M., et al. 2008, ApJ, 672, 122

Fan, L., Lapi, A., De Zotti, G., & Danese, L. 2008, ApJ, 689, L101

Fanaroff, B. L., & Riley, J. M. 1974, MNRAS, 167, 31P

Ferrarese, L., & Merritt, D. 2000, ApJ, 539, L9

Finoguenov, A., Reiprich, T. H., & Böhringer, H. 2001, A&A, 368, 749

Friedmann, A. 1922, Zeitschrift fur Physik, 10, 377

Furusawa, H., Kosugi, G., Akiyama, M., et al. 2008, ApJS, 176, 1

Gardner, J. P., Cowie, L. L., & Wainscoat, R. J. 1993, ApJ, 415, L9

Gebhardt, K., Bender, R., Bower, G., et al. 2000, ApJ, 539, L13

Gendre, M. A., Best, P. N., Wall, J. V., & Ker, L. M. 2013, MNRAS, 430, 3086

Girardi, M., Giuricin, G., Mardirossian, F., Mezzetti, M., & Boschin, W. 1998, ApJ, 505, 74

Goodwin, S. P., & Bastian, N. 2006, MNRAS, 373, 752

Griffith, R. L., Cooper, M. C., Newman, J. A., et al. 2012, ApJS, 200, 9

Grogin, N. A., Kocevski, D. D., Faber, S. M., et al. 2011, ApJS, 197, 35

Gültekin, K., Richstone, D. O., Gebhardt, K., et al. 2009, ApJ, 698, 198

Gürkan, G., Hardcastle, M. J., & Jarvis, M. J. 2014, MNRAS, 438, 1149

Hannestad, S. 2016, ArXiv e-prints, arXiv:1605.03829

Hasinger, G., Cappelluti, N., Brunner, H., et al. 2007, ApJS, 172, 29

Hine, R. G., & Longair, M. S. 1979, MNRAS, 188, 111

Hinshaw, G., Spergel, D. N., Verde, L., et al. 2003, ApJS, 148, 135

Hinshaw, G., Larson, D., Komatsu, E., et al. 2013, ApJS, 208, 19

Hogg, D. W. 1999, ArXiv Astrophysics e-prints, astro-ph/9905116

Hogg, D. W., Baldry, I. K., Blanton, M. R., & Eisenstein, D. J. 2002, ArXiv Astrophysics e-prints, astro-ph/0210394

Hu, W., Fukugita, M., Zaldarriaga, M., & Tegmark, M. 2001, ApJS

Hubble, E. 1929, Proceedings of the National Academy of Sciences, 15, 168

Ibar, E., Cirasuolo, M., Ivison, R., et al. 2008, MNRAS, 386, 953

Jarrett, T. H. 1992, PhD thesis, Massachusetts Univ., Amherst.

Kajita, T. 1999, Nuclear Physics B Proceedings Supplements, 77, 123

Kauffmann, G., Colberg, J. M., Diaferio, A., & White, S. D. M. 1999, MNRAS, 303, 188

Koekemoer, A. M., Faber, S. M., Ferguson, H. C., et al. 2011, ApJS, 197, 36

Koester, B. P., McKay, T. A., Annis, J., et al. 2007, ApJ, 660, 239

Komatsu, E., Smith, K. M., Dunkley, J., et al. 2011, ApJS, 192, 18

Lahav, O., & Liddle, A. R. 2006, Journal of Physics, G, 224

Lange, R., Driver, S. P., Robotham, A. S. G., et al. 2015, MNRAS, 447, 2603

Lani, C., Almaini, O., Hartley, W. G., et al. 2013, MNRAS, 435, 207

Larson, D., Weiland, J. L., Hinshaw, G., & Bennett, C. L. 2015, ApJ, 801, 9

Lawrence, A., Warren, S. J., Almaini, O., et al. 2007, MNRAS, 379, 1599

Le Brun, A. M. C., McCarthy, I. G., Schaye, J., & Ponman, T. J. 2014, MNRAS, 441, 1270

—. 2016, ArXiv e-prints, arXiv:1606.04545

Leauthaud, A., Tinker, J., Bundy, K., et al. 2012, ApJ, 744, 159

Lemaitre, G. 1931, Publications du Laboratoire d'Astronomie et de Geodesie de l'Universite de Louvain, vol. 8, pp.101-120, 8, 101

Lesgourgues, J., & Pastor, S. 2006, Physics Reports, 429, 307

Levi, M., Bebek, C., Beers, T., et al. 2013, ArXiv e-prints, arXiv:1308.0847

Lewis, A., Challinor, A., & Lasenby, A. 2000, ApJ, 538, 473

Lilly, S. J., Le Brun, V., Maier, C., et al. 2009, ApJS, 184, 218

Lin, Y.-T., Mohr, J. J., & Stanford, S. A. 2004, ApJ, 610, 745

Lindsay, S. N., Jarvis, M. J., Santos, M. G., et al. 2014, MNRAS, 440, 1527

Liske, J., Baldry, I. K., Driver, S. P., et al. 2015, MNRAS, 452, 2087

Mantz, A. B., Allen, S. W., Morris, R. G., et al. 2014, MNRAS, 440, 2077

Mantz, A. B., von der Linden, A., Allen, S. W., et al. 2015, MNRAS, 446, 2205

Maughan, B. J., Giles, P. A., Randall, S. W., Jones, C., & Forman, W. R. 2012, MNRAS, 421, 1583

McCarthy, I. G., Le Brun, A. M. C., Schaye, J., & Holder, G. P. 2014, MNRAS, 440, 3645

McCarthy, I. G., Schaye, J., Bird, S., & Le Brun, A. M. C. 2016, ArXiv e-prints, arXiv:1603.02702

McCracken, H. J., Milvang-Jensen, B., Dunlop, J., et al. 2012, A&A, 544, A156

McDonald, A. B., Ahmad, Q. R., Allen, R. C., et al. 2002, in American Institute of Physics Conference Series, Vol. 646, Theoretical Physics: MRST 2002, ed. V. Elias, R. Epp, & R. C. Myers, 43–58

McNamara, B. R., Wise, M., Nulsen, P. E. J., et al. 2000, ApJ, 534, L135

More, S., van den Bosch, F. C., Cacciato, M., et al. 2011, MNRAS, 410, 210

Moster, B. P., Naab, T., & White, S. D. M. 2013, MNRAS, 428, 3121

Mulchaey, J. S. 2000, ARA&A, 38, 289

Muldrew, S. I., Pearce, F. R., & Power, C. 2011, MNRAS, 410, 2617

Munari, E., Biviano, A., Borgani, S., Murante, G., & Fabjan, D. 2013, MNRAS, 430, 2638

Muzzin, A., Marchesini, D., Stefanon, M., et al. 2013, ApJS, 206, 8

Newman, A. B., Ellis, R. S., Bundy, K., & Treu, T. 2012, ApJ, 746, 162

Newman, J. A., Marinoni, C., Coil, A. L., & Davis, M. 2002, PASP, 114, 29

Norris, R. P., Afonso, J., Bacon, D., et al. 2013, PASA, 30, 20

Ntampaka, M., Trac, H., Cisewski, J., & Price, L. C. 2016, ArXiv e-prints, arXiv:1602.01837

Patterson, R. B. 2015, Annual Review of Nuclear and Particle Science, 65, 177

Peebles, P. J. E. 1968, ApJ, 153, 1

Pei, Y. C. 1992, ApJ, 395, 130

Pimbblet, K. A., Smail, I., Edge, A. C., et al. 2006, MNRAS, 366, 645

Planck Collaboration, Ade, P. A. R., Aghanim, N., et al. 2011, A&A, 536, A1

—. 2014, A&A, 571, A20

—. 2016, A&A, 594, A13

Planck Collaboration XVI, Ade, P. A. R., Aghanim, N., et al. 2014, A&A, 571, A16

Planck Collaboration XX, Ade, P. A. R., Aghanim, N., et al. 2014, A&A, 571, A20

Planck Collaboration XXIV, Ade, P. A. R., Aghanim, N., et al. 2015, ArXiv e-prints, arXiv:1502.01597

Proctor, R. N., Mendes de Oliveira, C., Azanha, L., Dupke, R., & Overzier, R. 2015, MNRAS, 449, 2345

Rees, G. A., Norris, R. P., Spitler, L. R., Herrera-Ruiz, N., & Middelberg, E. 2016, MNRAS, 458, L49

Refregier, A., Amara, A., Kitching, T. D., et al. 2010, ArXiv e-prints, arXiv:1001.0061

Reichardt, C., Jimenez, R., & Heavens, A. F. 2001, MNRAS, 327, 849

Richards, G. T., Lacy, M., Storrie-Lombardi, L. J., et al. 2006, ApJS, 166, 470

Rines, K., & Diaferio, A. 2006, AJ, 132, 1275

Robotham, A. S. G., Norberg, P., Driver, S. P., et al. 2011, MNRAS, 416, 2640

Rozo, E., Bartlett, J. G., Evrard, A. E., & Rykoff, E. S. 2014, MNRAS, 438, 78

Rozo, E., Rykoff, E. S., Evrard, A., et al. 2009, ApJ, 699, 768

Rozo, E., Wechsler, R. H., Rykoff, E. S., et al. 2010, ApJ, 708, 645

Ruel, J., Bazin, G., Bayliss, M., et al. 2014, ApJ, 792, 45

Saro, A., Mohr, J. J., Bazin, G., & Dolag, K. 2013, ApJ, 772, 47

Schaye, J., & Dalla Vecchia, C. 2008, MNRAS, 383, 1210

Schaye, J., Dalla Vecchia, C., Booth, C. M., et al. 2010, MNRAS, 402, 1536

Schinnerer, E., Smolčić, V., Carilli, C. L., et al. 2007, ApJS, 172, 46

Schinnerer, E., Sargent, M. T., Bondi, M., et al. 2010, ApJS, 188, 384

Schlegel, D. J., Finkbeiner, D. P., & Davis, M. 1998, ApJ, 500, 525

Sheth, R. K., Mo, H. J., & Tormen, G. 2001, MNRAS, 323, 1

Shimizu, M., Kitayama, T., Sasaki, S., & Suto, Y. 2003, ApJ, 590, 197

Silk, J., & Rees, M. J. 1998, A&A, 331, L1

Simpson, C., & Eisenhardt, P. 1999, PASP, 111, 691

Simpson, C., Westoby, P., Arumugam, V., et al. 2013, MNRAS, 433, 2647

Simpson, C., Almaini, O., Cirasuolo, M., et al. 2006, MNRAS, 373, L21

Simpson, C., Rawlings, S., Ivison, R., et al. 2012, MNRAS, 421, 3060

Smoot, G. F., Bennett, C. L., Kogut, A., et al. 1992, ApJ, 396, L1

Somerville, R. S., & Primack, J. R. 1999, MNRAS, 310, 1087

Spergel, D. N., Flauger, R., & Hložek, R. 2015, Physical Review D, 91, 023518

Springel, V. 2005, MNRAS, 364, 1105

Springel, V., White, S. D. M., Tormen, G., & Kauffmann, G. 2001, MNRAS, 328, 726

Strateva, I. V., Brandt, W. N., Schneider, D. P., Vanden Berk, D. G., & Vignali, C. 2005, AJ, 130, 387

Sutherland, W., & Saunders, W. 1992, MNRAS, 259, 413

Taylor, E. N., Hopkins, A. M., Baldry, I. K., et al. 2011, MNRAS, 418, 1587

Tinker, J., Kravtsov, A. V., Klypin, A., et al. 2008, ApJ, 688, 709

Tinker, J. L., Robertson, B. E., Kravtsov, A. V., et al. 2010, ApJ, 724, 878

Trager, S. C., & the Science Teams. 2012, (unpublished)

Tremaine, S., Gebhardt, K., Bender, R., et al. 2002, ApJ, 574, 740

Trump, J. R., Impey, C. D., McCarthy, P. J., et al. 2007, ApJS, 172, 383

van der Burg, R. F. J., Hoekstra, H., Muzzin, A., et al. 2015, A&A, 577, A19

van der Wel, A., Bell, E. F., Häussler, B., et al. 2012, ApJS, 203, 24

Vanden Berk, D. E., Richards, G. T., Bauer, A., et al. 2001, AJ, 122, 549

Velliscig, M., van Daalen, M. P., Schaye, J., et al. 2014, MNRAS, 442, 2641

Vikhlinin, A., Kravtsov, A. V., Burenin, R. A., et al. 2009, ApJ, 692, 1060

Viola, M., Cacciato, M., Brouwer, M., et al. 2015, ArXiv e-prints, arXiv:1507.00735

Vogel, P., Wen, L. J., & Zhang, C. 2015, Nat Commun, 6

Voit, G. M. 2005, Reviews of Modern Physics, 77, 207

von der Linden, A., Mantz, A., Allen, S. W., et al. 2014, MNRAS, 443, 1973

Wainer, H., & Thissen, D. 1976, Psychometrika, 41, 9

Weinberg, S. 1967, Physical Review Letters, 19, 1264

White, S. D. M., & Frenk, C. S. 1991, ApJ, 379, 52

Wiersma, R. P. C., Schaye, J., & Smith, B. D. 2009a, MNRAS, 393, 99

Wiersma, R. P. C., Schaye, J., Theuns, T., Dalla Vecchia, C., & Tornatore, L. 2009b, MNRAS, 399, 574

Williams, M. J., Bureau, M., & Cappellari, M. 2010, MNRAS, 409, 1330

Williams, R. J., Quadri, R. F., Franx, M., van Dokkum, P., & Labbé, I. 2009, ApJ, 691, 1879

Wilman, R. J., Miller, L., Jarvis, M. J., et al. 2008, MNRAS, 388, 1335

Wilson, S., Hilton, M., Rooney, P. J., et al. 2016, MNRAS, 463, 413

Wolstencroft, R. D., Savage, A., Clowes, R. G., et al. 1986, MNRAS, 223, 279

Wyman, M., Rudd, D. H., Vanderveld, R. A., & Hu, W. 2014, Physical Review Letters, 112, 051302

Xing, Z.-Z., & Zhao, Z.-H. 2016, Reports on Progress in Physics, 79, 076201

Zwicky, F., Herzog, E., Wild, P., Karpowicz, M., & Kowal, C. T. 1961, Catalogue of galaxies and of clusters of galaxies, Vol. I